Light-Induced Torque at Multipolar Plasmon Resonance

by

Yoon Kyung (Eunnie) Lee

Submitted to the Department of Mechanical Engineering in partial fulfillment of the requirements for the degree of

Master of Science in Mechanical Engineering

at the

MASSACHUSETTS INSTITUTE OF TECHNOLOGY

September 2013

Author.....

Department of Mechanical Engineering

August 23, 2013

Certified by.....

Nicholas X. Fang

D'Arbeloff Career Development Associate Professor

Thesis Supervisor

Accepted by.....

David E. Hardt

Chairman, Department Committee on Graduate Students

To the beloved.

Light-Induced Torque at Multipolar Plasmon Resonance

by

Yoon Kyung (Eunnie) Lee

Submitted to the Department of Mechanical Engineering
on Aug. 23, 2013, in partial fulfillment of the
requirements for the degree of
Master of Science in Mechanical Engineering

Abstract

Light-matter interaction provides a powerful means to control mechanical excitation in the nanoscale. The efficiency of this interaction reaches maximum at optical resonance. By understanding and designing the electromagnetic resonance of nanostructures, we can manipulate the electromagnetic field distribution as desired, with the benefits of enhancing the field strength and squeezing the field spot to be tighter than the diffraction limit. This thesis focuses on the enhanced mechanical effects arising at multipolar plasmon resonance of a subwavelength plasmonic resonator. We perform Finite Difference Time Domain (FDTD) simulation and show that the discrete rotational symmetry of the resonator determines the possible output modes in angular momentum conversion at non-dipolar plasmon resonance. Next, we analyze the efficiency of this conversion for a single, subwavelength nanoparticle in free space. Finally, we calculate the mechanical effects and report that scattering-induced transfer of torque can be unusually enhanced at non-dipolar resonance due to the effects of angular momentum conversion.

Thesis Supervisor: Nicholas X. Fang
Title: D'Arbeloff Career Development Associate Professor

Acknowledgement

I would like to thank the individuals who supported me through the ups and downs of my first two years at MIT. First and foremost, I sincerely thank Prof. Nicholas Xuanlai Fang, for the opportunity to work with him. His inspiration, patience, and guidance were invaluable to me. I'd also like to thank Prof. Kin Hung Fung for passing on a great deal of knowledge on the project, and helping me to get started with the fundamentals. Speaking of which, I must also thank Dr. Jun Xu, for his help and guidance in the lab, Dr. Dafei Jin, who taught me physics and the laws of nature in the office, Dr. Qing Hu, who taught me fabrication and introduced me to Chinese culture, Ansuman Kumar, who inspired me and spread a love towards physics & philosophy, Matt Klug, who shared his positivity and endurance towards research, and Fan Wang, who helped with the workstation and physical concepts - for all the help and discussions regarding the project. Special thanks to Matt, Anshuman, and Erinc, for the help during Quals. I'd like to thank Prof. Howon Lee, who helped me and gave sincere advice as I settled down in the Fang lab. I thank Prof. Nick Boechler and Prof. ShengQiang Cai for the advices on being an engineer and being in graduate school. I thank my lab-buddies Tian Gan, Mo Chen, and Jinhong Choi for sharing the moments of hardship and growth, and for sharing with me their dreams. For all of the names mentioned above, including Dr. Sang Hoon Nam and Narges Kaynia who recently joined, I thank them as a whole for being a part of the best group I could ever hope for.

I would like to thank KGSAME (Korean Graduate Student Association of Mechanical Engineering) for the precious friendship and support during the whole time I have been here at MIT. I thank 'Walking down the Endless Road in Boston' folks, and I thank all of my friends for sharing the happy and stupid times together. Special thanks to Sohae Kim and Ahhyun Nam. I thank GAME (Graduate Association of Mechanical Engineering) for liberating my heart from time to time, and the GWAMIT mentoring committee and my mentors Dr. Wendy Lin and Prof. Noelle Selin, for their advice and consolations. I thank Prof. Terry Orlando and Poorya Hosseini for giving me opportunities to strengthen my academic integrity. I thank Prof. Jung Hoon Chun and Prof. Sang Gook Kim for the advice and guidance about being an engineer in a new field. I thank Prof. Andy Yun, Prof. Wang-Yuhl Oh, and Prof. Dai Gil Lee for sowing in me a dream of becoming a researcher, from my undergraduate days in KAIST. I am sincerely grateful for NSF and Samsumg Scholarship which provided financial support for this study.

Finally, I'd like to thank my parents, my sister, and my boyfriend Kyungheon for their enduring love and support. This thesis is dedicated to them.

Table of Contents

Table of Contents 7

List of Figures 11

1. Introduction 15

1.1. Motivation: Torque transfer by Light 15

1.2. Momentum of Light and Advances in Optical Micro-manipulation 16

1.2.1. The Mechanical Properties of Light 16

1.2.2. Light Induced Motion: Optical Tweezers 17

1.2.3. Light Induced Torque in the Optical Tweezer Settings 18

1.2.4. Other Approaches in Particle Manipulation 19

1.3. Light Induced Momentum Transfer with Metallic Elements 20

1.3.1. Considerations for including Metallic Elements 20

1.3.2. Studies on the Optical Response of Metallic Nanoparticles 21

1.3.3. Trapping of Metallic Particles in the Optical Tweezer Environment 23

1.3.4. Metallic Nanostructures as a Platform for Nanotweezers 23

1.3.5. Torque on Metallic Particles 24

1.4. Problem Definition 25

1.5. Organization of Thesis 26

2. Theoretical Foundations 27

2.1. Basic Electromagnetic Theory and the Material Response to Light 27

2.1.1. Maxwell Equations 28

2.1.2. Energy, Momentum, Force, and Torque 29

2.1.3. Material Response to Light 32

2.1.4. Optical Resonance at an Interface and the Surface Plasmon Polariton 34

2.1.5. Polarization and Angular Momentum 39

2.2. Angular Grating Analogy 41

2.2.1. The Grating Equation 41

2.2.2. Angular Grating Analogy 42
2.3. Characterization and Calculation of the Optical Response 44
2.3.1. Definition of Optical Cross Sections 44
2.3.2. The Mie Theory 45
2.3.3. Computational methods for the calculation of optical response 45
2.3.4. Quantifying the Mechanical Effects of Absorption and Scattering 46
3. Finite Difference Time Domain (FDTD) Numerical Analysis 48
3.1. Simulation Setup 48
3.1.1. Yee Cell 48
3.1.2. Absorbing Boundary Condition 49
3.1.3. Material Response Fit 49
3.1.4. Light Source 50
3.2. Geometrical specifications 52
4. Results and Discussion 53
4.1. Verification of the Angular Grating Analogy 53
4.2. Angular Momentum Conversion of a Single Plasmonic Resonator 59
4.2.1. Possible Output Modes of a Plasmonic Converter 59
4.2.2. Dipole to Quadrupole Converter with 3-fold Symmetry 60
4.2.3. Results from a Plane Wave Source 62
4.2.4. Results from a Near Field Source 64
4.2.5. Highlighs on the Importance of Broken Symmetry 65
4.2.6. The Effect of Particle Size 66
4.3. Mechanical Effects at Multipolar Plasmon Resonance 67
4.3.1. Calculation of the Mechanical Effects 68
4.3.2. Particles with Perfect Rotational Symmetry 69
4.3.3. Particles with Discrete Rotational Symmetry 76
4.3.4. Material Variation: Effect of the Reduction in Loss 79

5. Summary and Outlook 84
5.1. Summary 84
5.2. Considerations and Future Outlook 85
5.2.1. Handling a Substrate or a Surrounding Medium 85
5.2.2. Mode Theory 86
5.2.3. Analysis of Thermal Effects 86
5.2.4. Experimental Characterization of the Scattered Field 87
References 89

List of Figures

Figure 1. Illustration of torque generation and angular momentum conversion at plasmon resonance. (a) The generation of mechanical torque. (b) The conversion of angular momentum state by the resonant excitation of the nanoparticle plasmon modes..... 25

Figure 2. An illustration of a metal-dielectric interface which can support surface plasmon polaritons. 35

Figure 3. Surface plasmon polariton dispersion. At low k_x, ω of the surface plasmon curve (solid) approaches that of the light line (dashed). At high k_x, ω approaches the constant value of ω_{sp}..... 36

Figure 4. Momentum-matching methods to couple photons and surface plasmon polaritons. (a) By a dielectric medium, i.e. prism coupling. (b) By a grating structure on the surface. The coupling is represented by the intersection of the light line and the surface plasmon curve..... 37

Figure 5. An illustration of Localized Surface Plasmon Resonance (LSPR). The dipolar SPP's are excited by the electric field of an incident light wave of frequency $\nu=1/T$. The electron cloud oscillates to form an electronic (-) region on one side and an ionic (+) region on the opposite side..... 37

Figure 6. A schematic of a linear grating. The incoming wavevector k can be converted to discrete output values k', due to the momentum matched by the linear grating. The grating period is *a*, and the integer j denotes the diffraction order. 41

Figure 7. A schematic of an angular grating with N-fold rotational symmetry. The incoming angular momentum number *m* can be converted to discrete output values *m*', due to the angular momentum matched by the angular grating. The left shows an example of a N=3 fold angular grating. The right shows the possible output angular momentum states, dictated by the discrete rotational symmetry of the grating. The three lowest order responses are listed. The arrows represent the direction of field rotation of each mode, and the multipole functions inside the round arrows indicate how much phase change occurs in 2π azimuthal angle. The red and blue colors are the positive and negative phase of the electric field, respectively. *m*'=1 is the dipole mode, *m*'=-2 is a negative quadrupole mode, and *m*'=4 is the octupole mode. 43

Figure 8. Dielectric function of gold, used in the FDTD simulations. (a) Real part of the dielctric function. (b) Imaginary part of the dielectric function. The dotted line is a smoothed experimental data from Palik, and the solid like is the FDTD function Fit. The solid dash line and solid dot line represents two artificial materials with reduced $\mathrm{Im}(\varepsilon)$, by a factor of 1/2 and 1/10, respectively. 51

Figure 9. Simulation scheme for Lumerical FDTD Software. The example particle illustrated is a flat gold triangle with edge size 400nm. (a) *y-z* cross section of the simulation region. The linearly

polarized plane wave source is located between the total field and scattered field monitor boxes (yellow), propagating towards the positive z direction. (b) *x-y* cross section. The orange box indicates the size of the meshing region. The size of the particle and the monitors (yellow) are shown. (c) The 3D view of the entire simulation space. The small orange box is the meshing region and the large orange box is the total FDTD simulation boundary, where PML boundary condition is applied..... 52

Figure 10. Representative polygon geometries for different N-fold discrete rotational symmetries. N=2 corresponds to mirror symmetry about one linear axis. For higher orders, the representative polygons are triangles for N=3, square for N=4, pentagon for N=5, and hexagon for N=6..... 54

Figure 11. Optical resonance of a 3-fold symmetric plasmonic particle. The extinction (solid), scattering (dotted), and absorption (dashed) are plotted with respect to wavelength. The triangle size is 300nm with 30nm-diameter rounded corners and 40nm thickness, and the surrounding dielectric medium has n=2.35. The absorption and scattering peaks for the same mode occur at slightly different wavelengths, and the absorption peaks correspond to 1715.76nm (m=1), 1044.74nm (m=-2), 814.14nm (m=4), and 706.321nm (m=-5), respectively. The modes in the shorter wavelength region consist of out-of-plane hybrid modes involving variations in the depth direction z..... 55

Figure 12. Snapshot of $\mathbf{E}_z$ on the surface of a 3-fold symmetric plasmonic particle. (a) m=1 dipole resonance at 1715.76nm. (b) m=-2 negative quadrupole resonance at 1044.74nm. (c) m=4 octupole resonance at 814.14nm. (d) m=-5 resonance at 706.32nm. The color represents the real part of $\mathbf{E}_z$ in arbitrary units. The distribution is measured with a 2D monitor located 2 nm above the surface. The + and – marks the sign of the electric field..... 56

Figure 13. Optical resonance of a 4-fold symmetric plasmonic particle. The extinction (solid), scattering (dotted), and absorption (dashed) are plotted with respect to wavelength. The square size is 400nm with 30nm-diameter rounded corners and 40nm thickness, and the surrounding medium has n=1. The absorption and scattering peaks for the same mode occur at slightly different wavelengths, and the absorption peaks correspond to above 990nm (m=1) and 578nm (m=-3), respectively. The modes in the shorter wavelength region consist of out-of-plane hybrid modes involving variations in the depth direction z..... 57

Figure 14. Snapshot of $\mathbf{E}_z$ on the surface of a 4-fold symmetric plasmonic particle. Left shows m'=1 dipole resonance at 990nm, and right shows m'=-3 resonance at 578nm. The color represents the real part of $\mathbf{E}_z$ in arbitrary units. The distribution is measured with a 2D monitor located 2 nm above the particle surface. The particle is identical with the one in Figure 13. The + and – marks the sign of the electric field..... 58

Figure 15. A schematic of the conversion of angular momentum state from m to m', by using a converter which possesses N-fold discrete rotational symmetry. The angular grating effect allows the conversion of incident angular momentum state m to multiple output states m'. A conversion to a particular m' channel is enhanced when the multipolar plasmon resonance matches the azimuthal order m'..... 60

Figure 16. Optical response of a 400nm triangular gold nanoplate inside vacuum (n=1). The extinction (solid), scattering (dotted), and absorption (dashed) efficiencies are plotted with respect to wavelength, and the two resonant modes, dipole (right inset) and negative quadrupole (left inset), are indicated with a snapshot of $\mathbf{E}_z$. The triangle edge length is 400nm with 40nm thickness. The rotating arrows inside the insets indicate the rotation of the phase. CCW direction matches the incidence and CW direction has the opposite sign. 61

Figure 17. Angular momentum conversion efficiency from a plane wave (far field) source. Left inset shows a left-hand plane wave (m=1) that can be converted to a negative quadrupole (m'=-2) using the resonant properties. Bottom (top) colored plot shows normal electric field 4nm above the surface of the triangular nanoplate at 640 nm (900 nm), representing approximately the corresponding charge distribution. 63

Figure 18. Angular momentum conversion efficiency from a near-field dipole source. Top inset shows a dipole emitter can be converted to a quadrupole emission source using the resonant properties. The radial plot on the left (right) shows the radial component of the electric field 400 nm away from the center of dipole source when the nanostructure is present (absent). 65

Figure 19. Comparison of the conversion efficiency between 3-fold and 6-fold symmetric converters. A smooth change from 6-fold symmetric hexagon to 3-fold symmetric triangle is observed. The momentum conversion onto the negative quadruple mode is only possible by a 3-fold symmetric structure, and not by the 6-fold symmetric structure. 66

Figure 20. The size dependence of the conversion efficiency. An optimum size exists for a maximum conversion efficiency. The results for a varied edge length of 200nm (gray), 250nm (red), 300nm (green), 350nm (blue), 400nm (black), and 450nm (magenta) are plotted. 67

Figure 21. The optical response of a spherical gold nanoparticle. (a) r=50nm. (b) r=100nm. (c) r=150nm. (d) r=200nm. Extinction (solid), scattering (dotted), and absorption (dashed) are plotted together. 69

Figure 22. Light induced force on a spherical gold nanoparticle. The top (a) shows total force, and the bottom (b) shows the force from absorption. The difference between the two is the scattering-induced force. The lines indicate the size variation of 200nm (solid), 150nm (dotted), 100nm (dashed), and 50nm (short dashed). 72

Figure 23. Light induced torque on a spherical gold nanoparticle. 100% of the torque comes from absorption. The lines indicate the size variation of 200nm (solid black), 150nm (dotted black), 100nm (dashed dark gray), and 50nm (dotted gray). The torque from absorption is plotted with square markers for all four curves, and shows an exact match with the total torque. 73

Figure 24. Optical response of a circular gold nanoplate with r=200nm. (a) extinction (solid), scattering (dotted), and absorption (gray dashed) efficiencies. (b) Force applied to the particle. (c) Torque applied to the particle, where 100% of the total torque (solid) and the torque from absorption (square marker) overlap exactly. The torque from the scattered field is zero. 74

Figure 25. Snapshot of $\mathbf{E}_z$ on the surface of a circular gold nanoplate. (a) m=1 dipole mode at 900nm excitation, (b) another mode with a different radial distribution, while azimuthal order is still m=1 (at 457nm excitation.) The color represents the real part of $\mathbf{E}_z$ in arbitrary units. The distribution is measured with a 2D monitor located 2 nm above the surface. The + and – marks the signs of the electric field, and the rotating arrow indicates the direction of phase rotation. CCW matches with the incident illumination. 75

Figure 26. Force and torque due to scattering and absorption from a triangular gold nanoplate. (a) F orce applied to the particle, which resembles the extinction efficiency profiles and is largely scattering dependent. (b) Torque applied to the particle. Total value (solid), scattering-induced value (dotted), and absorption-induced value (dashed) are plotted together. 77

Figure 27. Torque from the scattered field due to angular momentum conversion. The total torque (solid), torque from scattering (dotted), and the torque from the output scattered field (dot-dashed) are plotted together. 78

Figure 28. Snapshot of $\mathbf{E}_z$ on the surface of a triangular gold nanoplate. (a) m=1 dipole mode at 900nm excitation, (b) m=-2 quadrupole mode at 634.4nm. The color represents the real part of $\mathbf{E}_z$ in arbitrary units. The distribution is measured with a 2D monitor located 2 nm above the surface. The + and – marks the signs of the electric field, and the rotating arrow indicates the direction of phase rotation. CCW matches with the incident illumination. 79

Figure 29. Optical response of a triangular nanoplate, made of gold with reduced loss of $0.5\times\mathrm{Im}(\varepsilon)$. (a) Extinction (solid), scattering (dotted), and absorption (dashed) efficiencies are plotted together. (b) Force applied to the particle. (c) Torque applied to the particle. 80

Figure 30. Optical response of a triangular nanoplate, made of gold with reduced loss of $0.1\times\mathrm{Im}(\varepsilon)$. (a) Extinction (solid), scattering (dotted), and absorption (dashed) efficiencies are plotted together. (b) Force applied to the particle. (c) Torque applied to the particle. 81

Figure 31. Light induced torque on a circular gold disk, for materials with reduced loss. Colors represent the different materials, black for gold with full loss, dark gray for gold modified to half loss, and light gray for gold modified to 1/10 loss. For all three cases, the torque contribution from scattering is zero. Contribution from absorption is plotted in square markers 82

1. Introduction

1.1. Motivation: Torque transfer by Light

One of the significant challenges of nanotechnology is to develop a means to control the transfer of energy and momentum to individual objects and molecules that are too small for direct reach. Possible target objects include biomolecules, functionalized nanoparticles, and components for microfluidics and other nanoscale devices.

In the size range from hundreds of microns down to a few nanometers, the transfer of energy and momentum is best mediated by the use of fields, which can create a spatial distribution of stress, temperature, or density. As one of the fundamental forces in nature, light and other electromagnetic waves are particularly suited for this purpose because we can control the wavelength, intensity, polarization state, and spatial distribution simultaneously. For small particles on the order of a few microns and below, the optical response is governed by three major factors; the particle size compared to wavelength, the material's optical response, and the shape factor. The effect of each factors have been elucidated by the contributions from a great variety of science and engineering disciplines, including planetary atmospheres, climatology, laser micro-manipulation, physical chemistry, and single particle spectroscopy, to name a few.

Recently, the optical resonance properties of metal nanoparticles have gained a wide interest in both pure and applied science due to their enhanced optical absorption and scattering at resonance. Unlike transparent and dielectric objects, metallic nanoparticles have free electrons that can oscillate coherently with the incoming electromagnetic wave. When conditions are satisfied so that the free electrons move coherently, a very efficient transfer of energy and momentum is made possible. This is commonly used in sensor, diagnostics, photo-thermal engineering, and imaging applications.

It has been observed for sub-wavelength metallic particles that the shape factor plays a critical role in determining the optical resonance [1], [2]. The geometrical symmetry is especially important for the transfer of angular momentum and torque. Various experiments have shown

that the spin and orbital angular momentum of light can be transferred to microscopic particles and anisotropic structures, ranging from symmetric dielectric particles to birefringent and structured objects, and also with varied material properties. The results are reviewed extensively in 1.2.3 and 1.3.5. Manipulation of the angular momentum state of light also enables dense information packing per photon in quantum communication [3].

While complex structures have been fabricated and experimented, fundamental studies on the effects of particle symmetry on plasmon resonance are still rare in literature. We numerically study the transfer of optical angular momentum to simple shapes of metal nanopolygons, such as triangles, stars, and hexagons. The results show that the transfer of angular momentum can be enhanced by controlling the broken rotational symmetry of the structure together with plasmon resonance.

1.2. Momentum of Light and Advances in Optical Micro-manipulation

1.2.1. The Mechanical Properties of Light

In the 17^{th} century, Kepler suggested that light possesses mechanical properties, based on his proposal that the tail of the comet is created by the radiation pressure of the sun. Maxwell's treatise on electricity and magnetism, published in 1881, became the basis for the quantitative discussion of electromagnetism [4]. In 1884, Poynting quantified the momentum and energy flux of an electromagnetic field [5] and later reasoned in 1909 that light with circular polarization should carry angular momentum [6], from an analogy between a uniformly revolving shaft and a beam of circularly polarized light. The optical torque from the circular polarization of light was considered too small for experimental observation until the careful experiment by Beth in 1936 [7], where he measured the rotation of a birefringent wave plate suspended from a quartz fiber.

Thanks to the early pioneers, we now know and appreciate that photons have both linear and angular momentum. In vacuum, the energy, momentum, and angular momentum of light per photon can be quantified as:

$$E_{photon} = \hbar\omega \tag{1.1}$$

$$\vec{p}_{photon} = \hbar\vec{k} \tag{1.2}$$

$$j_{photon} = \hbar m \tag{1.3}$$

respectively, where $\hbar$ is the Planck constant, ω is the angular frequency of the electromagnetic wave, $\vec{k}$ is the wave vector with the magnitude $2\pi / \lambda$, with λ being the wavelength, and m is the total angular momentum quantum number, with the sign indicating the rotational direction. Detailed discussion continues in Chapter 2.

1.2.2. Light Induced Motion: Optical Tweezers

The influence of the momentum and angular momentum of a photon becomes evident during scattering or absorption processes. For example, the transfer of linear momentum from photons to an object results in an optical force that can be used for optical trapping and cooling, as demonstrated by Ashkin et al. in 1978 [8]. In their first realization of an optical tweezer, Ashkin et al. report that a strongly focused laser light incident on a transparent particle produced a gradient force, acting on the particle towards the region of highest irradiance [9]. The experimental studies on optical force and torque were greatly accelerated by the development of optical tweezers, also called laser micro-manipulation and optical trapping.

Since then, the field of optical tweezers progressed rapidly to generate multiple-beam optical traps, [10] improve the stability and trap strength, and broaden the application. Optical tweezers were used to study mechanical effects that were previously too small for experimental investigation, such as biological forces on the order of pico Newton (10^{-12}N) and the mechanical properties of biological compounds under tension and torsion (e.g. DNA [11], motor of bacterial flagellum [12]). Transparent dielectric particles with the size of a couple of microns were used as good "handle" particles because of the small absorption and scattering compared to other optically participating materials. A comprehensive review on the advances in optical tweezers is given in [13].

1.2.3. Light Induced Torque in the Optical Tweezer Settings

The first demonstration of torque added to an optical trap was done by attaching a micropipette tip on one of the dielectric particles and rotating the pipette tip mechanically [14]. Magnetic rotation of paramagnetic beads was demonstrated next, without the unstable mechanical component in the tweezer environment [11-13]. In order to measure the torque on the paramagnetic bead, a visibly asymmetric bead was tracked optically [17]. Calibration of torque for each bead was performed by measuring the phase delay of the bead rotation with respect to the rotating magnetic field, inside a fluid of known viscosity [17]. The dynamic relaxation of supercoiled DNA was investigated using this method [18].

Another way to simply apply torque to systems with a fixed rotational axis was to move the optical trap in a circle around the axis of the sample. This scheme was used to study the motor of the bacterial flagellum [12]. For systems with no fixed axis, an addition of one more optical trap which works as a rotation point was implemented [19].

While instrumentally more challenging, a more powerful technique to introduce torque is to use the change in the angular momentum of light. A light beam can carry angular momentum by its elliptical polarization state and also by the modified phase front distribution, as explained further in section 2.1.5. Liquid crystal arrays and holograms were used to introduce a desired phase front modulation of the light beam. Torque was originated from the light beam and then transferred to the particle via absorption and scattering of the trapping light [17-19]. A comprehensive review on optical torque is given by [23].

An addition of angular momentum into the trapping light can also be made by the asymmetry of the trapping particle itself, from the shape change such as windmill-shaped motor structures [22-24] and from the intrinsic birefringent properties of materials such as calcite and quartz [25-27]. Torque is applied to the asymmetric object in this case in order to conserve the angular momentum of the entire system, composed of the incident and scattered light and the object. When uniform birefringent particles are used, the incident and scattered light differs only in the polarization states, as opposed to the spatial distribution of light. Consequently, the exact torque on the particle can be calculated from the changes in the polarization state of the scattered light [28], [30]. A feedback system was implemented to stabilize the torque applied to the particle, which is similar to the feedback methods used for the control of force and position[28].

For the difficulty in simultaneously aligning the extraordinary axis of the birefringent material with the asymmetries of the particle and the axis of the desired experiment [29], micron-sized quartz cylinders were fabricated with the extraordinary axis of the quartz aligned with the short axis of the cylinder [31].

1.2.4. Other Approaches in Particle Manipulation

Along with the development of optical tweezers, magnetic tweezers [32] and AC dielectrophoresis [33] methods have also been developed to trap and manipulate micron-scale dielectric particles. In each of these techniques, the force scales with the volume of the trapped object, which means that a 10 nm object requires a million times larger input power than a 1-micron object.

In order to trap smaller objects, researchers have sought ways to decrease the trapping volume by focusing light using sub-wavelength structures [34], which is explained further in 1.3.4, and by the use of electrokinetic traps with feedback, which effectively cancels the Brownian fluctuation of a single molecule smaller than 100nm in solution [35].

For direct manipulation using contact forces in the nanoscale, the scanning probe microscopes are used. (STM [36] and AFM [37]) Scanned probes require direct mechanical access to the object being manipulated, with the tip necessarily a few nm away from the object. Scanned probes have very high spatial resolution, but are restricted to moving objects on solid surfaces. The usage is also limited to stiffer materials because a large local force exerted by a sharp probe tip might damage soft biomaterials.

In conclusion, this section gives a brief overview of the advances in optical tweezers for dielectric material manipulation. The incorporation of rotational forces is discussed in detail, and several methods which can be substituted in place of optical tweezers are summarized.

1.3. Light Induced Momentum Transfer with Metallic Elements

1.3.1. Considerations for including Metallic Elements

Before jumping into how metallic particles differ in their optical response compared their dielectric counterparts, it is worth noting why metallic components are of interest for mechanical manipulation. The biggest advantage in using metallic particles and structures is the sub-wavelength local enhancement of the electromagnetic field at resonance, allowing efficient transfer of energy, momentum, and angular momentum. This happens when the free electrons inside the particle are in resonance, oscillating coherently with the incoming field. Because of the high local electromagnetic field intensity produced, the visibility and sensitivity of the optical signals can be increased. At the same time, scattering and absorption are greatly enhanced.

Because large scattering and absorption entail optical radiation forces of its own, it hinders tweezer manipulation which uses laser intensity gradients to keep the particle at a desired location. Also, absorption produces heating, and thermal effects pose additional challenges in accurate manipulation. From these reasons, the use of metallic nanoparticles as "handles" for micro-manipulation has not been realized.

On the other hand, engineering the scattering and absorption behaviors of nanoparticles could open up new possibilities of optical manipulation. An enhancement in the application of torque is particularly interesting with a metallic structure, since a simple plane wave can transfer its spin angular momentum onto a nanoparticle through absorption [38]. Absorption and scattering are very weak for dielectric materials with small optical constants. If only dielectric materials are to be used, micrometer- or even millimeter-scale particles and motors are required to generate a useful amount of torque, in the range of [pN μm/W μm^{-2}]. Due to this reason, most of these dielectric systems require a manipulation of the phase front of the illuminating beam or a complex anisotropy of the object such as birefringence or asymmetry in shape. This significantly limits the type of light sources and materials that can be used. On the contrary, tailoring the absorption and scattering of metallic particles could open up ways for a more efficient torque generation.

In order to do this, we first need to understand the optical response of metallic particles and the governing parameters. The following section presents a brief history in the study of the optical response of metallic particles and lists useful references.

1.3.2. Studies on the Optical Response of Metallic Nanoparticles

The strongly enhanced surface plasmon resonance of noble metal nanoparticles at optical frequencies makes them excellent scatterers and absorbers of visible light (see 2.1.4 for a detailed explanation). Studies about the resonance of metallic nanoparticles date back to Faraday's investigations of gold colloids in the middle of the 19th century. The Maxwell's equations for the optical response of metal nanoparticles were first solved analytically for a homogeneous isotropic sphere by Gustav Mie in 1908 [39]. Mie's solution remains of great value to this day, and many extensions of Mie theory have been made for covering different modifications including magnetic[40] and coated spheres [41].

Yet this analytical method is fundamentally limited that the exact solutions are restricted to highly symmetrical particles such as spheres, cylinders, and spheroids [37-38]. For other non-spherical particles, a number of numerical approximate methods based on more advanced scattering theories have been developed, which are discussed in detail in 2.3.3 and further in Chapter 3.

The absorption and scattering cross sections of gold and silver nanoparticles are 5 to 6 orders higher in magnitude than other molecular species such as organic chromophores. This enhancement happens when the free electrons on the surface of the conducting particle oscillate coherently with the incoming electromagnetic wave. This special condition of electromagnetic resonance is called (Localized) Surface Plasmon Polariton Resonance (LSPR, SPR, SPP). As a result, the absorption and scattering of a metallic nanostructure can be significantly enhanced, as explained in detail in 2.1.4. Different geometries that enable the excitation of LSPR are also summarized in 2.1.4. Discussion on the experimental techniques for characterizing the resonance modes will be discussed further in Chapter 5.

In general, light absorption dominates the extinction spectrum for particles of relatively small radius (<20 nm), and light-scattering becomes the dominant process for large particles. As the particle size increases, the surface plasmon peaks are usually shifted toward the longer, red

wavelengths. New peaks may also appear in the extinction spectra due to the excitation of quadrupole and higher order modes [44]. The enhanced absorption is commonly used in sensors, diagnostics, and photothermal engineering applications. The enhanced scattering, on the other hand, is mainly used for imaging.

A big advantage of the use of gold and silver in the biochemical environment is that their surfaces can be easily functionalized with various functional groups by taking advantage of the well-established monolayer chemistry based on alkanethiols ($HS(CH_2)_nX$) with different functional groups ($X = CO_2^-$, SO_3^-, PO_3^{2-}, OH, $N(CH_3)_3^+$, CH_3) [45], [46].

One can precisely control the wavelengths at which gold and silver nanoparticles absorb and scatter light by controlling their shapes, dimensions, and structures, and it is also possible to tailor the magnitude of absorption and scattering coefficients by engineering their geometric parameters.

In addition to extinction, gold or silver nanostructures can be used to substantially enhance local electromagnetic fields. Upon excitation of SPP's, charges will be concentrated at the metal–dielectric interface, resulting in very strong amplification of the electric field **E**. For colloidal particles 10-200 nm in size where LSPR modes are excited, the magnitude squared of the electric field $|\mathbf{E}|^2$ can be 100 to 10,000 times greater in magnitude than the incident field. The field distribution has a spatial range on the order of 10-50 nm and is strongly dependent on the size, shape, and local dielectric environment of the particle.

The ability of gold and silver nanostructures to enhance the local electric fields has led to the development of surface-enhanced spectroscopy, such as surface enhanced Raman scattering (SERS) [47] and surface enhanced fluorescence [48]. Electromagnetic enhancement occurs when the incident light is in resonance with the SPP modes of a metallic thin film or nanoparticle. Gold and silver nanostructures with controllable shapes enable fine-tuning of the spectral positions of the SPP peak wavelengths to achieve the desired resonance conditions, and therefore are excellent candidates for sensing applications [2], [46-47]. Trianglular nanoplates, which are often called "nanoprisms" in the field of physical chemistry, were extensively studied in the past decade[50–53], and the existence of the quadrupolar resonance mode was reported several times using a variety of excitation methods [54], [55].

1.3.3. Trapping of Metallic Particles in the Optical Tweezer Environment

First, we summarize the advances in incorporating metallic particles to the traditional optical tweezer environment. While the trapping of dielectric particles have been successfully realized by optical tweezers, the trapping of metal nanoparticles in a stable manner has been more difficult because metallic particles exhibit a high absorption and scattering behavior due to the interaction of the incident electromagnetic field with the free electrons in the particle.

The scattering and absorption create forces of their own, and to overcome such effects with a traditional optical tweezer, a stronger gradient force is necessary. In 1994, Svoboda and Block showed the trapping of gold beads of 36nm diameter, where the gold particles were trapped with a 7-fold higher trap stiffness compared to the similarly sized polystyrene beads [56]. This was possible because the particle was much smaller than the wavelength of light, thereby falling into the Rayleigh regime, where the scattering from metals and dielectric particles are similar. Larger metal particles have also been confined in two dimensions by annular rings [57] or scanning beams [58] which rely on light scattering to produce a repulsive force and trap the particle.

Hansen et al. showed experimentally that gold nanoparticles with diameters in the range of 18 to 254 nm could be trapped with a tightly focused single laser beam [59]. Bosanac et al. experimentally demonstrated the trapping of silver nanoparticles[60].

The possible improvements for the gradient force-based optical tweezers are the size and stiffness of the trap. The focus of a conventional optical tweezer is diffraction-limited to be approximately half the wavelength or larger. This focal spot size limits the achievable gradient force from a given input laser power, and also reduces the precision of the trap when the size of the trapped particle is much smaller than the trap itself. Because of the high laser power and the absorptive property of metallic particles, the heating issue was pointed out as the major backlash preventing the use of metallic nanoparticles for optical manipulation handles. [61].

1.3.4. Metallic Nanostructures as a Platform for Nanotweezers

The use of near-field optics was suggested in order to decrease the trapping volume and increase the trap stiffness more effectively without increasing the intensity of the laser beams. Methods

using waveguide modes that create evanescent fields above a dielectric surface were reported by Ng et al. and Sasaki & Hotta in 2000, Gaugiran et al. in 2005, and by Yang et al. in 2009 [54-57].

The use of surface plasmon polariton (SPP) excitation was also investigated for the creation of highly enhanced evanescent fields [32, 58-61]. Plasmon-based optical manipulation was first demonstrated for the control of dielectric particles. Garces-Chavez et al. excited surface plasmon polaritons (SPPs) on a gold film, and observed the self-organization of dielectric particles over a large area through the combined effect of optical and thermal convection forces [70]. Volpe et al. used a variation of an optical tweezer known as a photonic force microscope, and measured the enhancement of optical forces on dielectric particles 500 nm above the gold film [71]. The enhanced manipulation of gold particles separated by a small gap from a gold film was observed by measuring the velocity of gold particles pushed by optical radiation forces arising from SPP excitation [72].

1.3.5. Torque on Metallic Particles

In order to apply torque on metallic particles, two major approaches were taken that differ in the source of the rotational force, similar to the study of dielectric particles. The first approach used the angular momentum state of light as the source of the rotational force, as demonstrated by O'Neil and Padgett [73]. They used an inverted optical tweezer with both spin angular momentum from circular polarization and orbital angular momentum from Laguerre-Gaussian beam. The orbital angular momentum input created a bulk motion of the spherical particles around the beam axis, which was unaffected by the change in polarization, and thus they concluded that the major mechanism for the particle motion is scattering rather than absorption.

The second approach used the rotation-inducing geometry of the particle as the source of the rotational force, as demonstrated by Liu et al. [74] The authors fabricated a gold nanostructure in a shape of a gammadion, and excited the plasmonic resonance of the nanoparticle in order to enhance the rotational forces generated by the locally varied strength of the electric field inside the gammadion. The rotor particle with size of 1/10 of the wavelength was reported to be capable of rotating a silica microdisk, 4,000 times larger in volume. The rotation velocity and direction can be controlled by varying the wavelength of the incident light, thereby inducing different plasmonic modes that possess different torque directions [74].

Recently, experimental advances in nanotrapping and nanotweezing enabled the demonstration of extremely fast rotations of plasmonic nanoparticles in water, which results from the transfer of spin angular momentum of circularly polarized incident beam due to absorption, aided by heat-induced viscosity drop of the fluidic environment [75].

1.4. Problem Definition

Our goal is to numerically study the efficiency of angular momentum transfer at different resonant modes of a metallic nanoparticle of varied geometries. Flat gold nanoparticles with polygonal geometries are studied, such as triangles, stars, and hexagons. The particles used in our analysis do not possess any intrinsic anisotropy or chirality, as opposed to complex rotational shapes like windmills. The size of the particle is varied between 50-500nm, which is approximately of the same order of magnitude as the wavelength, or smaller. The incident angular momentum state is created by a circularly polarized plane wave at normal incidence, or by a rotating electric dipole in the center of the nanoparticle. FDTD numerical calculation method is used to study different geometries of flat metal nanopolygons, such as triangles, stars, and hexagons.

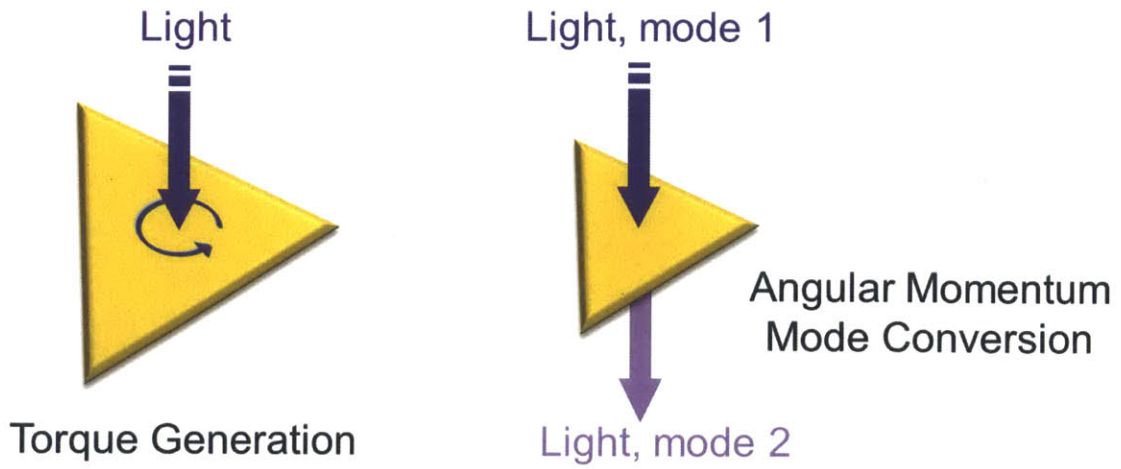

Figure 1. Illustration of torque generation and angular momentum conversion at plasmon resonance. (a) The generation of mechanical torque. (b) The conversion of angular momentum state by the resonant excitation of the nanoparticle plasmon modes.

Figure 1 visualizes the two major application perspectives from the high efficiency of angular momentum transfer. The first is the enhancement of mechanical torque generation. The second is the conversion efficiency of light's angular momentum state from one to another, when the nanostructure is excited at different resonance modes. This possibility is analyzed with a conversion efficiency defined for a single 'angular momentum converter'.

We find that the resonance is dictated by the discrete rotational symmetry of the structure dictates the possible resonant modes that can be excited at normal incidence. We give a theoretical interpretation for the symmetry-dependent resonant mode selection with an analogy of angular grating. Our results show that the transfer of angular momentum can be enhanced by operating at the 'negative quadrupole' resonance, which will be explained in detail throughout the thesis.

1.5. Organization of Thesis

This thesis presents a numerical analysis of how a circular polarization of light interacts with the optical resonance modes of a single, sub-micron nanoparticle suspended in free space. Chapter 2 provides a background on the scattering theory and plasmonic enhancement, then describes the angular grating theory. Chapter 3 describes the methods and conditions of the finite difference time domain (FDTD) numerical calculation. Chapter 4 discusses the results. Finally, chapter 5 summarizes the key findings and provides an outlook on future work.

2. Theoretical Foundations

Before delving into the particular problem of enhancing the transfer of angular momentum to a metallic nanoparticle, first we can start from a general picture of electromagnetic energy, momentum, and resonance. What is the definition of the energy and momentum of light? How can light exert force and torque onto a particle? What is an 'optical resonance' or 'plasmon resonance'? These are the basic questions that form the foundations of this study, of which the answers are well documented in literature and textbooks.

The first section of this chapter summarizes the theory of electromagnetic wave and the optical response, and the second section presents the theoretical backbone of this thesis: the angular grating analogy. This theory describes how the symmetry of the particle governs the excitable higher order resonance modes of a nanostructure. According to this angular grating analogy, we aim to answer the following question: what is role of the shape and symmetry of the particle for torque transfer? The angular grating analogy explains why the excitation of resonant modes depends on the discrete rotational symmetry of the nanostructures. Lastly, the third section summarizes the characterization and calculation of optical response at resonance. Starting with the Mie theory for highly symmetric particles, we move on to the computational methods for non-spherical objects.

2.1. Basic Electromagnetic Theory and the Material Response to Light

A brief review of the underlying electromagnetic theory is presented in this section. Special care is given to a modification in each term for the case of absorptive and dispersive (frequency-dependent) optical media, such as noble metals that are considered in this thesis. Next, the calculation of electromagnetic force and torque from the Maxwell Stress Tensor method is reviewed. The material dependence of the constitutive relation is explained with simple models of the dielectric functions, again with a few modifications for a proper treatment of the noble

metals at a wide range of frequencies. Finally, the surface plasmon polariton and size-dependent resonance of localized surface plasmon is explained.

2.1.1. Maxwell Equations

The macroscopic Maxwell equations can be written as the following [4].

$$\begin{aligned} \nabla \cdot \mathbf{D} &= \rho_{ext} \\ \nabla \cdot \mathbf{B} &= 0 \\ \nabla \times \mathbf{H} &= \mathbf{J}_{ext} + \frac{\partial \mathbf{D}}{\partial t} \\ \nabla \times \mathbf{E} &= -\frac{\partial \mathbf{B}}{\partial t} \end{aligned} \tag{2.1}$$

These equations link the four macroscopic fields **D** (the electric displacement), **E** (the electric field), **B** (the magnetic induction or magnetic flux density), and **H** (the magnetic field), with the external charge and current densities ρ_{ext} and $\mathbf{J}_{ext}$, respectively. The total charge and current densities are a summation of the internal $(\rho, \mathbf{J})$ and external $(\rho_{ext}, \mathbf{J}_{ext})$ contributions, so that in total, $\rho_{tot} = \rho + \rho_{ext}$ and $\mathbf{J}_{tot} = \mathbf{J} + \mathbf{J}_{ext}$ holds.

The constitutive relation between **D** and **E**, **B** and **H** are:

$$\mathbf{D} = \varepsilon_0 \mathbf{E} + \mathbf{P} \tag{2.2}$$

$$\mathbf{H} = \frac{1}{\mu_0}\mathbf{B} - \mathbf{M} \tag{2.3}$$

where the polarization **P** and magnetization **M** links the four macroscopic fields, and ε_0 and μ_0 are the constants of vacuum electric permittivity and vacuum magnetic permeability, respectively. The polarization describes the electric dipole moment per unit volume inside the material, caused by the alignment of microscopic dipoles with the electric field, and **P** is related to the internal charge density by $\nabla \cdot \mathbf{P} = -\rho$. The definition and derivation for **P** will be discussed in detail in 2.1.4. Further, charge conservation relates the internal current density with polarization by:

$$\nabla \cdot \mathbf{J} = -\frac{\partial \rho}{\partial t} = \frac{\partial \mathbf{P}}{\partial t}. \tag{2.4}$$

Then the divergence of the electric field can be expressed as the *total* charge density divided by vacuum permittivity:

$$\nabla \cdot \mathbf{E} = \frac{\rho_{tot}}{\varepsilon_0} \tag{2.5}$$

and for linear, isotropic and nonmagnetic media, (2.2) and (2.3) are simplified as:

$$\mathbf{D} = \varepsilon_0 \varepsilon \mathbf{E} \tag{2.6}$$

$$\mathbf{B} = \mu_0 \mu \mathbf{H} \tag{2.7}$$

where ε is the dielectric function or the relative permittivity, and μ = 1 is the relative permeability. One more constitutive relation between the electric field and the internal current density can be written as:

$$\mathbf{J} = \sigma \mathbf{E} \tag{2.8}$$

where σ is the conductivity.

The Boundary Conditions at the interface between two media are:

$$(\mathbf{E}_2 - \mathbf{E}_1) \times \mathbf{n} = 0 \tag{2.9}$$

$$(\mathbf{H}_2 - \mathbf{H}_1) \times \mathbf{n} = 0 \tag{2.10}$$

where **n** is the outward normal of the interface. Different computational methods use slightly different forms of the above governing equations. The computation in this thesis uses the original time domain equations presented in this section.

2.1.2. Energy, Momentum, Force, and Torque

The Lorentz force law gives the force applied to a single charge q inside an electromagnetic field.

$$\mathbf{F} = q(\mathbf{E} + v \times \mathbf{B}) \tag{2.11}$$

In case when the force is applied to a collection of charges, using the Lorentz force law for each charge becomes difficult. A surface integral method can be used, called the Maxwell Stress Tensor (MST) method. In order to formulate a stress tensor representing the change in momentum due to electromagnetic forces, let us first define the energy and momentum of an electromagnetic field.

For a linear medium with no dispersion or loss, the total energy density of the electromagnetic field can be written [76] as:

$$u = \frac{1}{2}(\mathbf{E}\cdot\mathbf{D} + \mathbf{B}\cdot\mathbf{H}) = \frac{1}{2}(\varepsilon_0\varepsilon\mathbf{E}^2 + \mu_0^{-1}\mu^{-1}\mathbf{B}^2) \tag{2.12}$$

This expression enters together with the Poynting vector of energy flow $\mathbf{S} = \mathbf{E}\times\mathbf{H}$ into the energy conservation law,

$$\frac{\partial u}{\partial t} + \nabla\cdot\mathbf{S} = -\mathbf{J}\cdot\mathbf{E} \tag{2.13}$$

relating changes in electromagnetic energy density u to energy flow $\mathbf{S}$ and absorption inside the material. The Poynting vector in each direction can be calculated in the same way as

$$\mathbf{S}_z = \mathbf{E}_x\mathbf{H}_y^* - \mathbf{E}_y\mathbf{H}_x^* \ . \tag{2.14}$$

In a lossy, dispersive media, however, (2.12) does not hold because the energy of the total electromagnetic field should not be complex or frequency dependent. According to Landau and Lifshitz, the effective energy density is defined as

$$u_{eff}(\omega_0) = \frac{1}{2}Re\left[\frac{\mathrm{d}(\omega\varepsilon)}{\mathrm{d}\omega}\right]_{\omega_0}\left\langle\mathbf{E}(\vec{r},t)\cdot\mathbf{E}(\vec{r},t)\right\rangle + \frac{1}{2}\mu_0^{-1}\mu^{-1}\left\langle\mathbf{B}(\vec{r},t)\cdot\mathbf{B}(\vec{r},t)\right\rangle \tag{2.15}$$

where taking the real part of ε requires the assumption of low absorption. The energy conservation (2.13) is consequently modified to be (2.16) below.

$$\frac{\partial u_{eff}(\omega_0)}{\partial t} + \nabla\cdot\mathbf{S} = -\omega_0\,\mathrm{Im}\left[\varepsilon(\omega_0)\right]\left\langle\mathbf{E}(\vec{r},t)\cdot\mathbf{E}(\vec{r},t)\right\rangle \tag{2.16}$$

For the case of highly absorbing media, the electric part of the effective energy density is modified as the following.

$$u_{eff,E} = \frac{\varepsilon_0}{4}\left(\varepsilon_1 + \frac{2\omega\varepsilon_2}{\Gamma}\right)|\mathbf{E}|^2 \tag{2.17}$$

The additional factor of 1/2 is due to the implicit assumption of harmonic time dependence. For energy localization in fields at metallic surfaces, (2.17) is used. The Poynting vector using the complex electromagnetic fields can be written as:

$$\begin{aligned}\mathbf{S} &= \mathbf{E}(\vec{r},t)\times\mathbf{H}(\vec{r},t) = \mathrm{Re}(\mathbf{E}(\vec{r})\mathrm{e}^{i\omega t})\times\mathrm{Re}(\mathbf{H}(\vec{r})\mathrm{e}^{i\omega t}) \\ &= \frac{1}{2}\mathrm{Re}(\mathbf{E}\times\mathbf{H}^*) + \frac{1}{2}\mathrm{Re}(\mathbf{E}\times\mathbf{H}e^{2i\omega t})\end{aligned} \tag{2.18}$$

and the time averaged form is:

$$\langle \mathbf{S} \rangle = \frac{1}{T}\int_0^T \mathbf{S}(t)dt = \frac{1}{T}\int_0^T \mathbf{S}(t)dt$$
$$= \frac{1}{T}\int_0^T \left[\frac{1}{2}\mathrm{Re}(\mathbf{E}\times\mathbf{H}^*) + \frac{1}{2}\mathrm{Re}(\mathbf{E}\times\mathbf{H}e^{2i\omega t})\right]dt = \frac{1}{2}\mathrm{Re}(\mathbf{E}\times\mathbf{H}^*) \quad . \tag{2.19}$$

A conservation law for the momentum of an electromagnetic wave can be written as:

$$\frac{\partial \mathbf{S}}{\partial t} + \nabla\cdot\overline{\overline{\mathbf{T}}} = 0 \quad . \tag{2.20}$$

For the calculation of the total force and torque applied to an object, a volume is chosen to enclose the object to form a closed surface. The time-averaged form of the momentum conservation law can be written as:

$$\frac{\partial \langle \mathbf{S} \rangle}{\partial t} + \nabla\cdot\left\langle \overline{\overline{\mathbf{T}}} \right\rangle = 0 \quad . \tag{2.21}$$

The Maxwell Stress Tensor is a second rank tensor, formulated to greatly simplify the calculations of the Lorentz force through tensor arithmetic. The definition of the Maxwell stress tensor is given in (2.22).

$$T_{\alpha\beta} = \mathbf{E}_\alpha\mathbf{D}_\beta + \mathbf{B}_\alpha\mathbf{H}_\beta - \frac{1}{2}\delta_{\alpha\beta}(\mathbf{E}\cdot\mathbf{D} + \mathbf{B}\cdot\mathbf{H})$$
$$= \varepsilon_0\varepsilon\mathbf{E}_\alpha\mathbf{E}_\beta + \mu_0^{-1}\mu^{-1}\mathbf{B}_\alpha\mathbf{B}_\beta - \frac{1}{2}\delta_{\alpha\beta}(\varepsilon_0\varepsilon\mathbf{E}^2 + \mu_0^{-1}\mu^{-1}\mathbf{B}^2) \tag{2.22}$$

The time averaged form can be written as:

$$\langle T_{\alpha\beta} \rangle = \frac{1}{2}\mathrm{Re}\left(E^*{}_\alpha D_\beta\right) + \frac{1}{2}\mathrm{Re}\left(B^*{}_\alpha H_\beta\right) - \frac{1}{4}\mathrm{Re}\left(\mathbf{E}^*\cdot\mathbf{D}\right) - \frac{1}{4}\mathrm{Re}\left(\mathbf{B}^*\cdot\mathbf{H}\right)$$
$$= \left[\frac{1}{2}\mathrm{Re}\left(\varepsilon_0\varepsilon E^*{}_\alpha E_\beta\right) + \frac{1}{2}\mathrm{Re}\left(\mu_0^{-1}\mu^{-1}B^*{}_\alpha B_\beta\right)\right. \tag{2.23}$$
$$\left. - \frac{1}{4}\mathrm{Re}\left(\varepsilon_0\varepsilon\mathbf{E}^*\cdot\mathbf{E}\right) - \frac{1}{4}\mathrm{Re}\left(\mu_0^{-1}\mu^{-1}\mathbf{B}^*\cdot\mathbf{H}\right)\right]$$

where the element αβ gives the flux of momentum parallel to the αth axis crossing a surface normal to the βth axis (in the negative direction) per unit time.

The time averaged force amd torque on a particle due to harmonic fields can be found by integrating the MST over the closed surface area surrounding the particle. The integration gives the value of the total force and total torque applied to the particle.

$$\mathrm{Force} = \oint_S \overline{\overline{\mathbf{T}}}\cdot d\mathbf{A} \tag{2.24}$$

$$\text{Torque} = \oint_S (\vec{r} \times \overline{\overline{\mathbf{T}}}) \cdot d\mathbf{A} \tag{2.25}$$

For numerical computation of the force and torque exerted onto the particle, the time-averaged form of all the MST is used in equations (2.24) and (2.25).

2.1.3. Material Response to Light

The electromagnetic response of a nonmagnetic medium can be characterized entirely by the relative permittivity ε, also called the dielectric function. For time harmonic fields of the form of $\exp(-i\omega t)$, Fourier Transform can be done to the constitutive relations in the time domain,

$$\mathbf{D}(\vec{r},t) = \varepsilon_0 \int dt' d\vec{r}' \varepsilon(\vec{r}-\vec{r}',t-t')\mathbf{E}(\vec{r}',t') \tag{2.26}$$

$$\mathbf{J}(\vec{r},t) = \int dt' d\vec{r}' \sigma(\vec{r}-\vec{r}',t-t')\mathbf{E}(\vec{r}',t') \tag{2.27}$$

which yields:

$$\mathbf{D}(\mathbf{K},\omega) = \varepsilon_0 \varepsilon(\mathbf{K},\omega)\mathbf{E}(\mathbf{K},\omega) \tag{2.28}$$

$$\mathbf{J}(\mathbf{K},\omega) = \sigma(\mathbf{K},\omega)\mathbf{E}(\mathbf{K},\omega) \tag{2.29}$$

where **K** is the wave vector and ω is the angular frequency. Thus ε is given as the following in the Fourier domain.

$$\varepsilon(\mathbf{K},\omega) = 1 + \frac{i\sigma(\mathbf{K},\omega)}{\varepsilon_0 \omega} \tag{2.30}$$

The wave vector dependence of the dielectric function is called the nonlocal effect. In order to neglect this K dependence and assume a spatially local response, λ must be significantly larger than all of the characteristic dimensions, such as the size of the unit cell or the mean free path of the electrons. Nonlocal effects can be significant at sharp tips of metallic cones or in the proximity of narrow gaps. In all the systems dealt in this thesis, the assumption of spatial locality is valid, thus $\varepsilon(\mathbf{K}=0,\omega) = \varepsilon(\omega)$.

It is worth noting that the distinction between the bound and free charges in (2.30) may vary according to different conventions. At low frequencies, ε usually represents the response of the bound charges, while σ describes the free charge contribution. At optical frequencies, this distinction can be blurred. A detailed description is given in [77].

A simple equation of motion for an electron displacement in response to an electric field excitation of $\mathbf{E} = \mathbf{E}_0 \exp(-i\omega t)$ can be written as:

$$m^*\left(\frac{\partial^2 \vec{r}}{\partial t^2} + \Gamma\frac{\partial \vec{r}}{\partial t} + \omega_0{}^2 \vec{r}\right) = -e\mathbf{E} \tag{2.31}$$

where $\vec{r}$, e, and m^* are the displacement, charge, and effective mass of a free electron, respectively. $\omega_0{}^2 = k_{bound}/m^*$ is the resonant frequency of the bound electrons, where k_{bound} is the effective spring constant that limits the motion of the bound electrons as opposed to the free electrons, for which $\omega_0 \approx 0$. For metals, ω_0 can be neglected in the low frequency regime but needs to be considered in the visible frequency regime in order to represent interband transitions [78]. $\Gamma = 1/\tau$ is the characteristic collision frequency of the electrons, which represents the damping due to electron scattering. The relaxation time τ is typically on the order of 10^{-14} s for free electron gas at room temperature, corresponding to Γ=100THz. The solution of the electron displacement is:

$$\vec{r} = \frac{e/m^*}{(\omega^2 - \omega_0^2) + i\Gamma\omega}\mathbf{E} \tag{2.32}$$

Optical resonance of a single medium happens when this electric displacement $\vec{r}$ is greater at some frequencies compared to others, when the denominator of (2.32) becomes smaller. This displacement can be plugged into the polarization,

$$\mathbf{P} = -ne\vec{r} \tag{2.33}$$

where n is the electron number density. Optical resonance thus represents the enhancement of **P**. Therefore the relative permittivity ε can be calculated as a function of ω.

$$\varepsilon = 1 + \frac{\mathbf{P}}{\varepsilon_0 \mathbf{E}} = 1 + \frac{ne\vec{r}}{\varepsilon_0 \mathbf{E}} \tag{2.34}$$

The general form of the solution is a Lorentz-oscillator type response, which includes the bound electrons:

$$\varepsilon(\omega) = 1 - \frac{\omega_p^2}{\omega^2 - \omega_0^2 + i\Gamma\omega} \tag{2.35}$$

where $\omega_p = \sqrt{ne^2/\varepsilon_0 m^*}$ is the volume plasma frequency. One more extension to the model should be made for noble metals (e.g. Au, Ag, Cu), in the high frequency region. The high frequency response is dominated by the free s electrons, and the filled d band close to the Fermi

surface causes a highly polarized environment. This residual polarization due to the positive background of the ion cores can be described by adding the term $\mathbf{P}_\infty = \varepsilon_0(\varepsilon_\infty - 1)$ to (2.2). This gives:

$$\varepsilon(\omega) = \varepsilon_\infty - \frac{\omega_p^2}{\omega^2 - \omega_0^2 + i\Gamma\omega} \tag{2.36}$$

where $1 \leq \varepsilon_\infty \leq 10$, typically. The Drude model for purely free electrons can be simplified as the following.

$$\varepsilon_{Drude}(\omega) = 1 - \frac{\omega_p^2}{\omega^2 + i\Gamma\omega} \tag{2.37}$$

The dielectric function is a mathematical representation of the magnitude and phase of the electron oscillation with respect to the driving electromagnetic field. Further, the complex dielectric function and the complex refractive index are:

$$\varepsilon(\omega) = \varepsilon_1(\omega) + i\varepsilon_2(\omega) \tag{2.38}$$

$$\tilde{n}(\omega) = n(\omega) + i\kappa(\omega) = \sqrt{\varepsilon(\omega)} \tag{2.39}$$

For both (2.38) and (2.39), the physical interpretation of the imaginary parts $\varepsilon_2(\omega)$ and $\kappa(\omega)$ is decay of the electron oscillation due to damping. The real part of the refractive index $n(\omega)$ represents the optical density of the medium, where the speed of light inside the medium is inversely proportional to $n(\omega)$. The real part of the dielectric function becomes important for metals, and consequently for optical resonance. The sign of $\varepsilon_2(\omega)$ is positive for most dielectric materials where $\omega_0 > \omega$, and also positive for metals in high frequency regime above the plasma frequency. On the other hand, metals below the plasma frequency exhibit a negative $\varepsilon_1(\omega)$, which is the case for noble metals in the visible spectrum. A negative dielectric function means that the electron oscillation inside the metal is out of phase with the driving electromagnetic field.

2.1.4. Optical Resonance at an Interface and the Surface Plasmon Polariton

In 2.1.3, we calculated $\varepsilon(\omega)$ and defined the resonance of a single medium in bulk. In a single medium, the enhancement of **P** with respect to the magnitude of **E** characterized optical resonance. In this section, we discuss a different mode of resonance which can happen at the surface between two different media.

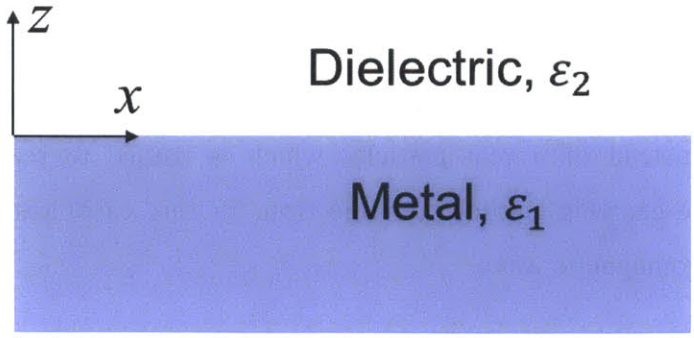

Figure 2. An illustration of a metal-dielectric interface which can support surface plasmon polaritons.

At an interface between metallic ($\varepsilon < 0$) and dielectric ($\varepsilon > 0$) media shown in Figure 2, the Maxwell's equations can be solved to yield a surface-wave eigenmode solution for transverse magnetic (TM) polarization [78]. This solution has the form of a surface wave bound to the interface, mathematically represented as a wave propagating along the metal-dielectric surface and decaying to zero away from the interface on both sides. The detailed derivation for a single interface solution can be found in [71-73], and for multilayer systems with further discussions, in [78]. At a single interface, the wave vector along the surface k_x is expressed as a function of the two dielectric functions ε_1 and ε_2 of the two media:

$$k_x = k_0 \sqrt{\frac{\varepsilon_1 \varepsilon_2}{\varepsilon_1 + \varepsilon_2}}, \quad k_0 = \frac{\omega}{c} \tag{2.40}$$

which is plotted in Figure 3. The wave vector perpendicular to the surface k_x inside the two media becomes:

$$k_{j,z} = \sqrt{\varepsilon_j k_0^{\,2} - k_x^2} = k_0 \frac{\varepsilon_j}{\sqrt{\varepsilon_1 + \varepsilon_2}}, \quad j = 1,2 \tag{2.41}$$

where j indicates the medium. To meet the constraint of a surface wave solution, $\exp(ik_z z)$ should be real and decaying in both media. This gives the conditions of (2.42) below.

$$\varepsilon_1 \varepsilon_1 < 0 \text{ and } \varepsilon_1 + \varepsilon_2 < 0 \tag{2.42}$$

Because the dielectric constant of a metal is negative for frequencies below the volume plasma frequency ($\omega < \omega_p$), the surface wave mode can exist in this frequency range. This solution is of great interest because the electromagnetic field is confined to a small volume near the surface instead of being distributed in the whole volume, resulting in an enhancement in the field intensity.

This mode is called the surface plasmon mode, where surface plasmon polaritons are the quanta of the electromagnetic surface waves that propagate at the interface between a metal and a dielectric by the collective motion of electrons. The word "polariton" specifies that a plasmon is a 'quasi-particle' instead of a real particle, which is named to represent the collective oscillation of a dipole-carrying particle (an electron, in this case) resulting from a strong coupling with an electromagnetic wave.

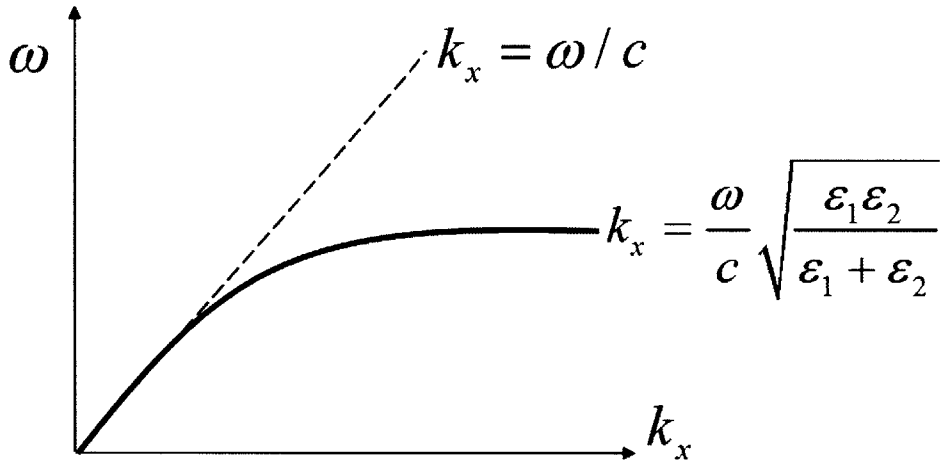

Figure 3. Surface plasmon polariton dispersion. At low k_x, ω of the surface plasmon curve (solid) approaches that of the light line (dashed). At high k_x, ω approaches the constant value of ω_{sp}.

The surface plasmon frequency at the high k limit of Figure 3 is $\omega_{sp} = \omega_p / \sqrt{1+\varepsilon_2}$. The plasmon mode can be excited by a photon if both the energy and momentum of the incoming photon match those of the surface plasmon. But this is not possible from a simple plane wave of normal incidence. In Figure 3, the plasmon has a higher value of momentum in the x direction (k_x), compared to the photon. As a result, a 'momentum-matching' condition should be provided. This is typically done by: (1) manually tilting or strongly focusing the light to create an oblique incidence, (2) introducing a light-tiling element on the surface, such as a surface roughness, a prism, or a diffraction grating, and (3) using a sub-wavelength metallic particle, which has a radius of curvature of the surface that is smaller or comparable to the wavelength of light. The first two cases can be represented by the modification of the dispersion relationship, as shown in Figure 4. The excitation of the plasmon mode, i.e. the surface wave mode, allows a confinement of energy into dimensions smaller than the diffraction limit ($\lambda/2$) and provides an enhancement of the electromagnetic field.

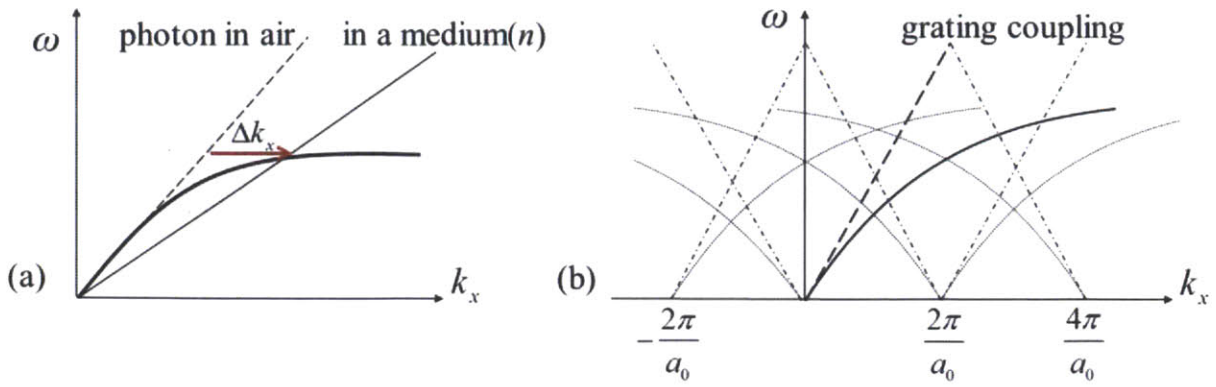

Figure 4. Momentum-matching methods to couple photons and surface plasmon polaritons. (a) By a dielectric medium, i.e. prism coupling. (b) By a grating structure on the surface. The coupling is represented by the intersection of the light line and the surface plasmon curve.

In Figure 4, the addition of linear momentum achieved by the two structures are: (a) $\Delta k_x = (n-1)\omega / c$ by placing a dielectric medium with n, and (b) $\Delta k_g = j \cdot 2\pi / a_0$, where j is an integer, by placing a grating structure with lattice periodicity a_0 .

The third case, using a metallic nanoparticle, is another type of resonance where both the electrons and the electromagnetic fields are strongly localized. This is particularly interesting due to the extremely small confinement volume of the electromagnetic field and the large enhancement in absorption and scattering efficiencies. This phenomenon is named as the (localized) surface plasmon resonance (LSPR, SPR). Figure 5 shows a simple schematic of the electron cloud of a metallic nanoparticle oscillating in response to the harmonic electric field.

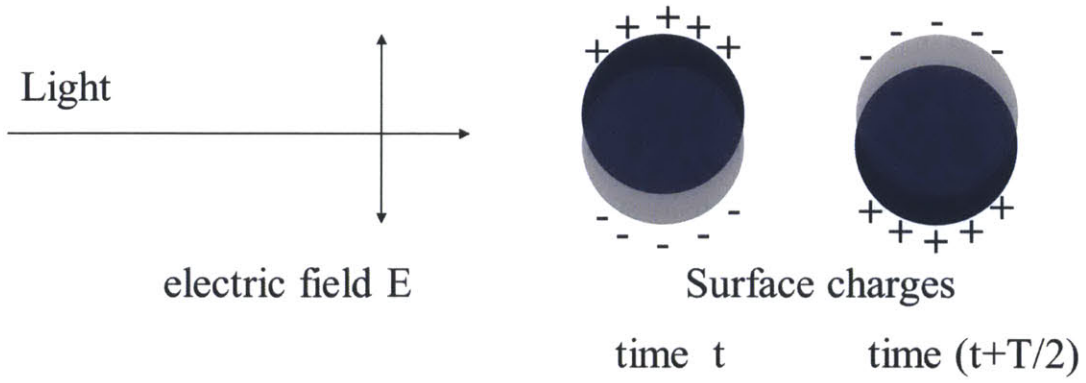

Figure 5. An illustration of Localized Surface Plasmon Resonance (LSPR). The dipolar SPP's are excited by the electric field of an incident light wave of frequency ν=1/T. The electron cloud oscillates to form an electronic (-) region on one side and an ionic (+) region on the opposite side.

In Figure 5, let's denote the dielectric constant of the metallic particle to be ε_p and that of the surrounding dielectric medium to be ε_m. In the limiting case of a very small metallic sphere of radius $\ll \lambda$, we can neglect the phase difference across the particle in the direction of propagation of the driving electric field. The polarizability of the particle can be approximated in this case [79]:

$$\mathbf{P} = \alpha \mathbf{E} = \left(3\varepsilon_m \frac{\varepsilon_p - \varepsilon_m}{\varepsilon_p + 2\varepsilon_m} V \right) \mathbf{E} \qquad (2.43)$$

where α is the polarizability of the particle, and $V = 4\pi a^3/3$ is the volume of the spherical particle. Metallic particles allow the real part of the denominator to approach zero, when $\mathrm{Re}(\varepsilon_p)+2\varepsilon_m \approx 0$. For gold in water, this condition is satisfied at wavelength of excitation near 505nm [80]. At these wavelengths, polarizability increases greatly, indicating that the particle is on resonance. At the resonance wavelength, energy from the external driving field can efficiently couple into the particle and excite strong electron oscillation. When the resonance occurs in visible wavelength range, the particle can be considered as an optical antenna. The oscillating electrons can create very high surface charge densities and consequently very high local field intensities.

Nanoparticles with geometries other than spheres permit stronger polarizabilities and local fields. Examples of these particles include nanorods [81], nanoshells [82], nanostars [83], nanotriangles and hexagons [76-77], and nanorice [84]. The sharp tips exhibited by these nonspherical particles are very efficient in achieving high surface charge densities: the field intensity enhances in the "hot spots" more than several hundred times [84].

A strong field confinement can also be achieved in small gaps or between metal nanoparticle and metal surfaces or between metal nanoparticle pairs[79-80]. The small gap acts like a capacitor which stores high density surface charges across the gap. An example is a bowtie optical antenna, which is an optical frequency analogue of a radio frequency dipole antenna. From the efficient excitation by external illumination, enhancement of the electric field can occur within a spatial extent below the diffraction limit [87].

2.1.5. Polarization and Angular Momentum

A monochromatic laser beam can be written as a plane wave propagating in the z direction in terms of two orthogonal components:

$$\mathbf{E}(\vec{r},t) = \mathbf{E}_x\hat{x} + \mathbf{E}_y\hat{y} \qquad (2.44)$$

where $\vec{r} = (x, y, z)$, and $\mathbf{E}_x = \mathbf{E}_{x0}e^{ikz-i\omega t}$, $\mathbf{E}_y = \mathbf{E}_{y0}e^{ikz-i\omega t}$ are the two orthogonal electric field components in x and y, respectively. If $\mathbf{E_x}$ and $\mathbf{E_y}$ have the same phase, (2.44) represents a linearly polarized wave, with its polarization vector making an angle $\theta = \tan(\mathbf{E}_{x0} / \mathbf{E}_{y0})$.

On the other hand, if $\mathbf{E}_x$ and $\mathbf{E}_y$ have different phases, (2.44) is elliptically polarized. A special case of an elliptical polarization is circular polarization, when the phase difference between $\mathbf{E}_x$ and $\mathbf{E}_y$ are exactly 90°, corresponding to the phase factor $i = \sqrt{-1}$. At a fixed point in space, the fields are such that the electric vector has a constant magnitude but sweeps around in a circle at frequency ω.

The sign $(\hat{x} + i\hat{y})$ is called a left circularly polarized beam (LCP) in optics, and a positive helicity in some disciplines of physics. The rotation is counterclockwise when the observer faces the oncoming wave. The opposite sign $(\hat{x} - i\hat{y})$ is called right circularly polarized (RCP) beam, and it has negative helicity.

An orthogonal set of basis can describe an arbitrary polarization, and the LCP and RCP vectors form an orthogonal basis set, which means that any plane wave of arbitrary polarization can be decomposed into a weighted linear combination of LCP and RCP fields. The complex orthogonal unit vectors can be written as:

$$\hat{r}_{\pm} = \frac{1}{\sqrt{2}}(\hat{x} \pm i\hat{y}) \qquad (2.45)$$

Together with the linear polarization basis, the four elementary polarization directions $(\hat{x}, \hat{y}, \hat{r}_+, \hat{r}_-)$ represent the four parameters of a Stokes vector, which is explained in [88].

A laser beam carries angular momentum in two distinct forms: spin angular momentum, associated with the polarization of the beam, and orbital angular momentum, associated with the spatial structure of the beam [89]. Either or both can be zero. The spin angular momentum S varies from $-\hbar$ to $\hbar$ per photon, with S = $-\hbar$ for RCP and S = $\hbar$ for LCP. For linear polarization, S = 0 and elliptical polarization can possess intermediate values. The spin angular momentum is

intrinsic in each photon and is not affected by the spatial distribution of a light beam. Thus the measurement is invariant with the translation of the measurement axis.

Orbital angular momentum is not associated with the polarization of a beam but rather with the Poynting vector possessing inclined wavefronts, Laguerre-Gaussian beams being prime examples [90]. Orbital angular momentum is quantized as $l\hbar$ per photon, where l is an integer, allowing the value to potentially exceed the spin angular momentum. The transfer of both spin and orbital angular momentum can occur through various methods, including absorption, birefringence, and scattering, depending on the particle's properties and the form of angular momentum involved in the problem [23, 79-80]. The distinction between spin and orbital angular momentum becomes important when considering the scattering or absorption processes by which the angular momentum is transferred.

2.2. Angular Grating Analogy

In this section, a theory of mode selection is presented with an analogy of linear and angular grating. The theory aims to explain the strong geometry dependence of the angular momentum transfer between the angular momentum carried by light and the discrete rotational symmetry of the metallic nanostructure.

2.2.1. The Grating Equation

A diffraction grating is a periodic optical component, which splits and diffracts light into several beams travelling in different directions. The directions of these beams depend on the grating period a and the wavelength of light λ, related by a simple grating equation:

$$\sin\theta' - \sin\theta = \frac{n\lambda}{a} \tag{2.46}$$

where the incident angle θ and resulting angle θ' are indicated in Figure 6.

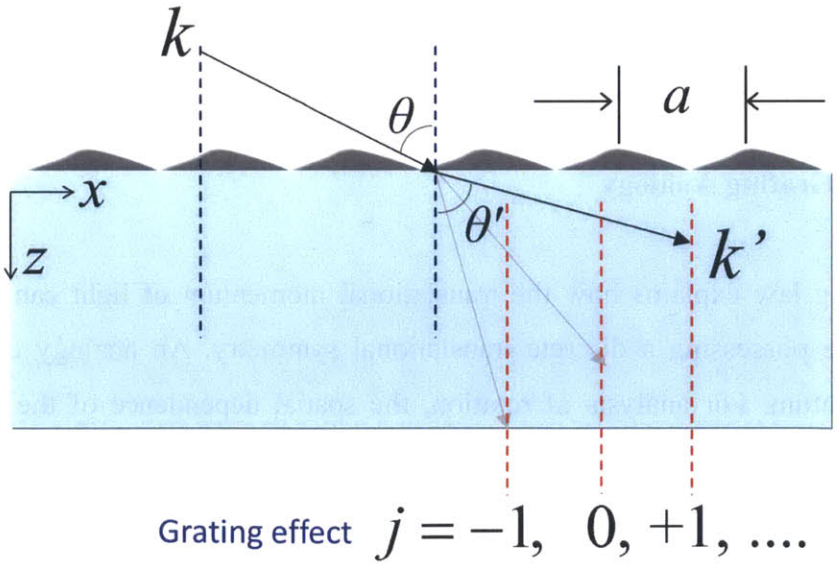

Figure 6. A schematic of a linear grating. The incoming wavevector k can be converted to discrete output values k', due to the momentum matched by the linear grating. The grating period is a, and the integer j denotes the diffraction order.

The field propagating in the *x*-*z* plane can be expressed as:

$$\mathbf{E}(\vec{r}) = \mathbf{E}_0 e^{i(k\cdot\vec{r})} = \mathbf{E}_0 e^{i(k_x x + k_z z)} \tag{2.47}$$

and after the interaction with the linear grating in *x* direction, the change in the wave vector can be written as:

$$\begin{aligned} k_x' &= k_x + j\frac{2\pi}{a} \\ k_z' &= k' - k_x' = \sqrt{k^2 - k_x'^2} \end{aligned} \tag{2.48}$$

where j is an integer. The total momentum k is conserved while the direction of propagation is changed. If we focus on the momentum in the *x* direction k_x, the grating can add or subtract a discrete value of momentum, $2\pi/a$, decided by the grating period *a*.

A translation-invariant structure such as a smooth line has no means of adding momentum in one direction. On the other hand, a grating has a 'broken' translational symmetry in the sense that translation by an arbitrary value does not result in the same structure, thus breaking the continuous symmetry. Instead, a grating has a 'discrete' translational symmetry, because a translation by certain values, in this case an integer multiple of the grating period, comes back to the original structure. This discrete symmetry of a grating allowing the interference of the diffracted beams to possess a new direction of momentum *k'* that is different from the original *k*.

2.2.2. Angular Grating Analogy

The linear grating law explains how the translational momentum of light can be altered by a periodic structure possessing a discrete translational symmetry. An analogy can be made for rotational momentum. For analysis of rotation, the spatial dependence of the electromagnetic field can be expressed in terms of angle φ as:

$$\mathbf{E}(r,\varphi) = \mathbf{E}_0(r) e^{im\varphi} \tag{2.49}$$

where m is the total angular momentum number, which represents how much phase variation occurs in one cycle of $\varphi=2\pi$. For circular polarization, $m=\pm 1$, because phase changes exactly 2π during one cycle. This corresponds to a rotating dipole mode, as depicted in Figure 7. For higher orders of angular momentum states, *m* can be larger than 1 and each integer *m* corresponds to a

rotating multipole mode. Sign difference in m represents the opposite direction of rotation, just like LCP (m=1) and RCP (m= –1).

Let us consider a non-circular object with N-fold discrete rotational symmetry. As in the case of a perfect translational symmetry of a smooth line, a perfect rotational symmetry means that there is no change in the structure under a rotation of an arbitrary amount. A perfect rotational symmetry corresponds to a circle in 2D or a sphere in 3D.

Figure 7 shows an example of a structure possessing discrete rotational symmetry with order N=3. An N-fold rotational symmetry implies that the optical properties of the system are identical when the geometry is rotated by $2\pi/N$ radians. This discrete rotational symmetry, as in the case for the linear grating, supports a constructive interference of the diffracted light to possess a new value of angular momentum, governed by the angular momentum equation:

$$m' = m + \mathrm{jN} \tag{2.50}$$

where j is an integer and m' denotes the output angular momentum.

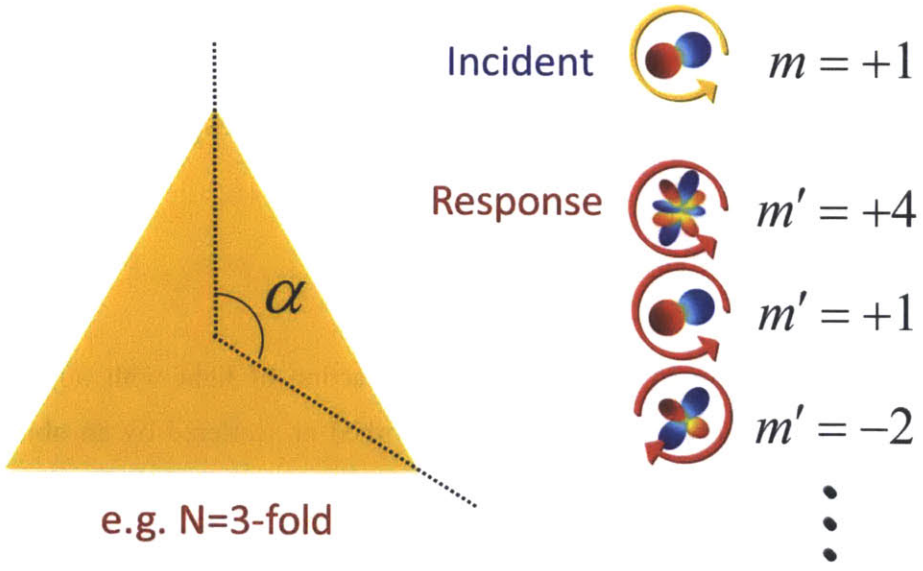

Figure 7. A schematic of an angular grating with N-fold rotational symmetry. The incoming angular momentum number m can be converted to discrete output values m', due to the angular momentum matched by the angular grating. The left shows an example of a N=3 fold angular grating. The right shows the possible output angular momentum states, dictated by the discrete rotational symmetry of the grating. The three lowest order responses are listed. The arrows represent the direction of field rotation of each mode, and the multipole functions inside the round arrows indicate how much phase change occurs in 2π azimuthal angle. The red and blue colors are the positive and negative phase of the electric field, respectively. m'=1 is the dipole mode, m'=-2 is a negative quadrupole mode, and m'=4 is the octupole mode.

A triangle is a simple example of a 3-fold angular grating, because the structure repeats itself after a rotation by $\alpha=2\pi/3$ radians.

Note that the excitation of the quadrupole resonant mode $m' = \pm 2$ from a circularly polarized beam at normal incidence is only possible with a 3-fold symmetric structure, as shown in Figure 7. This is because $m' = 1 \pm jN = \pm 2$ is only possible when N=3 and j=-1. As a result, the quadrupole resonant mode excited from a 3-fold symmetric structure is negative, which means that the direction of phase change with respect to azimuthal angle φ is always opposite to the incident excitation. This negative quadrupole mode is of particular interest in optical torque generation. The result of this analysis is discussed in detail in Chapter 4.

The order of the angular momentum states each represents how much phase difference occurs with respect to φ. The electric field profile of $m' = \pm 1$ state resembles a rotating dipole, while $m' = \pm 2$ resembles a rotating quadrupole, and so on. The modes with higher values of m indicate that the mode is not in a pure spin angular momentum state, but possesses a mixture of spin and orbital angular momentum states, which are not distinguished in the model.

2.3. Characterization and Calculation of the Optical Response

2.3.1. Definition of Optical Cross Sections

Optical cross sections are defined to quantify the interaction of light with objects. The cross sections represent the total power of light that is absorbed or scattered by an object imbedded inside a medium, divided by the intensity of the incident light.

The concept of a cross section is very commonly used to describe how large an object appears to incident external radiation. The spectral scattering of an individual structure is characterized by the scattering efficiency, which is a normalized representation of the effective scattering cross section viewed by the light source. Here we consider only elastic scattering, where the frequency of the incident and scattered light are identical. Inelastic scattering such as Brillouin and Raman scattering are not taken into account. The scattering cross section C_{sca} and the unitless scattering efficiency Q_{sca} are defined as:

$$C_{sca}(\lambda)=\frac{P_{sca}(\lambda)}{I_{illum}(\lambda)},\ Q_{sca}(\lambda)=\frac{C_{sca}(\lambda)}{G} \tag{2.51}$$

where G is the geometric cross section in the direction perpendicular to the incident illumination. C_{sca} stands for the fraction of the incident power that is scattered, with the unit of area. The spectral absorption efficiency can be expressed in the same manner:

$$C_{abs}(\lambda)=\frac{P_{abs}(\lambda)}{I_{illum}(\lambda)},\ Q_{abs}(\lambda)=\frac{C_{abs}(\lambda)}{G} \tag{2.52}$$

where C_{abs} is the absorption cross section and Q_{abs} is the unitless absorption efficiency. The extinction is defined as the sum of scattering and absorption, both for the extinction cross section C_{ext} and for the extinction efficiency Q_{ext} .

$$\begin{aligned} C_{ext}(\lambda)&=C_{sca}(\lambda)+C_{abs}(\lambda)\\ Q_{ext}(\lambda)&=Q_{sca}(\lambda)+Q_{abs}(\lambda) \end{aligned} \tag{2.53}$$

The extinction efficiency represents the total power lost from the incident field, per incoming intensity, due to the presence of the particle.

2.3.2. The Mie Theory

The Maxwell's equations for the optical response of metal nanoparticles were first solved analytically for a homogeneous isotropic sphere by Mie in 1908 [39]. The Mie theory bridges the intermediate size regions between the two limiting cases of the Rayleigh scattering model and ray optics model [93], which describe Rayleigh particles with $a << \lambda$ and large particles with $a >> \lambda$, respectively.

2.3.3. Computational methods for the calculation of optical response

Although many extensions of Mie theory have been made in order to cover the different aspects such as magnetic [40] and coated spheres [41], this analytical method is fundamentally limited that the exact solutions are restricted to highly symmetrical particles such as spheres, cylinders, and spheroids.

For other nonspherical particles, a number of numerical approximate methods based on more advanced scattering theories have been developed. These include the T-matrix method [94], the generalized multipole technique (GMT) [95], the discrete dipole approximation (DDA) [96], and the finite difference time domain method [82-83]. The T-matrix method and GMT are surface-based methods that discretize only the surface of the particle to be solved numerically. The DDA and FDTD methods are volume-based methods that discretize the whole volume of the particle.

For metallic nanoparticles of complex geometries, it is suitable to use a volume-based computational method for the calculation of scattering and absorption. The widely used DDA method is briefly explained, and the FDTD method is explained in detail in the next chapter.

In the DDA method, the particle is approximated as an array of polarizable cubic elements, with the array being large enough for the calculation to converge. The scattering and absorption cross sections of the particle can be obtained once the location and polarizability of each element have been specified. An advantage of the DDA method is that the optical cross sections can be calculated from a simple dipole approximation. However, in order to obtain the field distribution outside the particle for calculation of force and torque, the Maxwell's equations need to be solved for the region outside the particle and a complete simulation is required such as the FDTD method.

2.3.4. Quantifying the Mechanical Effects of Absorption and Scattering

When a photon is absorbed, the momentum $\hbar k$ and angular momentum $\hbar m$ carried by that photon are transferred entirely to the object. As a result, the mechanical effects can be quantitatively represented using the absorption cross section, $C_{abs}(\lambda) = P_{abs} / I_{inc}$, which is the absorbed power divided by the input intensity. Here, P_{abs} is the power absorbed by the particle and I_{inc} is the intensity of the input illumination. The force and torque created by absorption can be calculated by multiplying the number of absorbed photons per unit time ($P_{abs} / \hbar\omega$) with the momentum ($\hbar\vec{k}$) and angular momentum ($\hbar m$) of a single incident photon, respectively. This gives [38]:

$$\vec{\mathbf{F}}_{abs} = \frac{C_{abs} I_{inc}}{c} \hat{k} \tag{2.54}$$

$$\vec{\mathbf{M}}_{abs} = \frac{C_{abs} I_{inc}}{\omega} m \tag{2.55}$$

where $\vec{F}_{abs}$ [N] and $\vec{M}_{abs}$ [Nm] are force and torque from the absorbed field, c is the speed of light, $\hat{k}$ is the direction of the momentum vector, and m is the angular momentum number. Absorption arises from loss, which is associated with the imaginary part of the dielectric function Im(ε(λ)). When normalized with incident intensity, the normalized force becomes C_{abs}/c and the normalized torque becomes C_{abs}/ω.

When a photon is scattered, it carries a nonzero momentum after interacting with the particle. Thus the momentum of the scattered photon, as well as the incident photon, affects the resultant force and torque. The information about the outgoing, scattered field is essential. While the absorption-induced mechanical effects could be simply quantified by figuring out the total power absorbed into the particle, scattering-induced effects cannot be characterized this way. This is especially true for Mie particles with $C_{abs} < C_{sca}$, which indicates that extinction is dominated by scattering. The mechanical effects caused by the

$$\vec{\mathbf{F}}_{sca} = \frac{C_{sca} I_{inc}}{c} \hat{k} + \vec{\mathbf{F}}_{SF} \tag{2.56}$$

$$\vec{\mathbf{M}}_{sca} = \frac{C_{sca} I_{inc}}{\omega} m + \vec{\mathbf{M}}_{SF} \tag{2.57}$$

where $\vec{\mathbf{F}}_{SF}$ and $\vec{\mathbf{M}}_{SF}$ are force and torque calculated from the scattered field. Monitoring the scattered fields can be done by using the TFSF source, as explained in 3.1.4.

3. Finite Difference Time Domain (FDTD) Numerical Analysis

The finite-difference time-domain (FDTD) method is a direct solution of the Maxwell curl equation, originated from the work by Yee in 1966 [99]. FDTD method is widely used in computational electromagnetics to analyze interactions between electromagnetic waves and matter, especially complex dielectric or metallic structures. The general procedure involves approximating Maxwell's equation in real space using finite differences, on spatial grids called Yee cells. The time-domain responses are obtained by time-marching the fields explicitly and applying appropriate boundary conditions. In this thesis, the commercially available Lumerical FDTD software is used.

One of the major advantages of FDTD method is that a frequency response of a wide range can be obtained with a single simulation, by using a broadband pulsed source. The resulting time-dependent electromagnetic fields are Fourier-transformed to give the response in the frequency domain. The memory requirement of the computation was 26.5GB and all of the computations were carried out in the laboratory workstation.

3.1. Simulation Setup

3.1.1. Yee Cell

The Maxwell's curl equations are discretized on the Yee's lattice. The field variables are defined on a rectangular grid, and the electric and magnetic fields are separated in time by one-half time step and interlaced in space by one-half grid cell. Based on this scheme, center differences in both space and time are applied to approximate the Maxwell equations on each grid points. We use the grid size of 2 nm for the plasmonic nanostructure and the surrounding dielectric material. For spherical particles with radius larger than 100 nm, the grid size of 3 nm is used.

3.1.2. Absorbing Boundary Condition

To compute the field at any given point, we must know the value of the field at every adjacent point on the grid. With a finite computation cell, information from nodes outside the cell is not available. Fields at the nodes on the boundaries are therefore calculated using boundary conditions.

In this thesis, the PML boundary condition is used in the three-dimensional simulation. The Perfectly Matched Layer (PML) boundary condition is based on placing artificial absorbers around the cell boundary. The absorber is designed to be completely impedance-matched with free space, and a complete cancellation of reflection is achieved regardless of the incident angle. With this boundary condition we can perform FDTD computer experiments that allow us to calculate quantities of direct experimental relevance, such as extinction and transmission spectrum.

3.1.3. Material Response Fit

The time domain material response is required in order to solve the Maxwell's equations in the time domain. Because the experimental data are tabulated in the frequency domain, we need to use fit the data and then perform inverse Fourier-transform into the time domain. For the fitting function, we can use simplified models which require only a couple of parameters to be determined, or perform a more accurate fitting of the experimental data inside a specific frequency window. We use the latter method to improve the fitting accuracy in the desired wavelength window. The permittivity of gold is described by a fitting to the experimental data of Palik [100]. 300 data points are taken from the experimental data, in the simulation wavelength window (which is typically 350nm to 1200nm) and the fitting was performed with 5 independent parameters. For some simulations, different wavelength windows such as 350nm to 900nm, 700nm to 1200nm, and 1100nm to 1800nm were used. The material fitting procedure for all of the separate simulation ranges are the same. The results are shown in Figure 8. In order to analyze the effect of absorption, two artificial materials are created with modified values of $\mathrm{Im}(\varepsilon)$. For these materials, $\mathrm{Re}(\varepsilon)$ is identical to gold, while the imaginary part is changed to half

and one tenth. Due to the low loss of the artificial materials, absorption-induced effects are suppressed and the results are analyzed in detail in Figure 8.

The medium surrounding the metallic particle is regarded as a homogeneous dielectric with constant refractive index. Vacuum medium with n=1 is used for all of the force and torque calculations. The simulation result of Figure 11 is the only exception, using an artificially high refractive index of n=2.35 in order to display many high-order resonance modes of the same particle.

3.1.4. Light Source

The TFSF plane wave source is used in order to calculate the scattering of the particle. The computation region using the TFSF source can be separated into two distinct regions. The total field region includes both the incident and the scattered field, while the scattered field region only records the scattered field, without the incident plane wave.

In order to realize circular polarization, we use the standard linear combination method which is suggested by the Lumerical FDTD simulation software. First, two simulations are carried out separately, using TFSF source of orthogonal linear polarizations, noted 0 and 90. Then the resulting field data for the two simulations are combined with a phase shift, using the following equation. The incidence is left circularly polarized.

$$\begin{aligned} \mathbf{E}_{total} &= \left(\mathbf{E}_0 + i\mathbf{E}_{90}\right)/\sqrt{2} \\ \mathbf{H}_{total} &= \left(\mathbf{H}_0 + i\mathbf{H}_{90}\right)/\sqrt{2} \end{aligned} \tag{3.1}$$

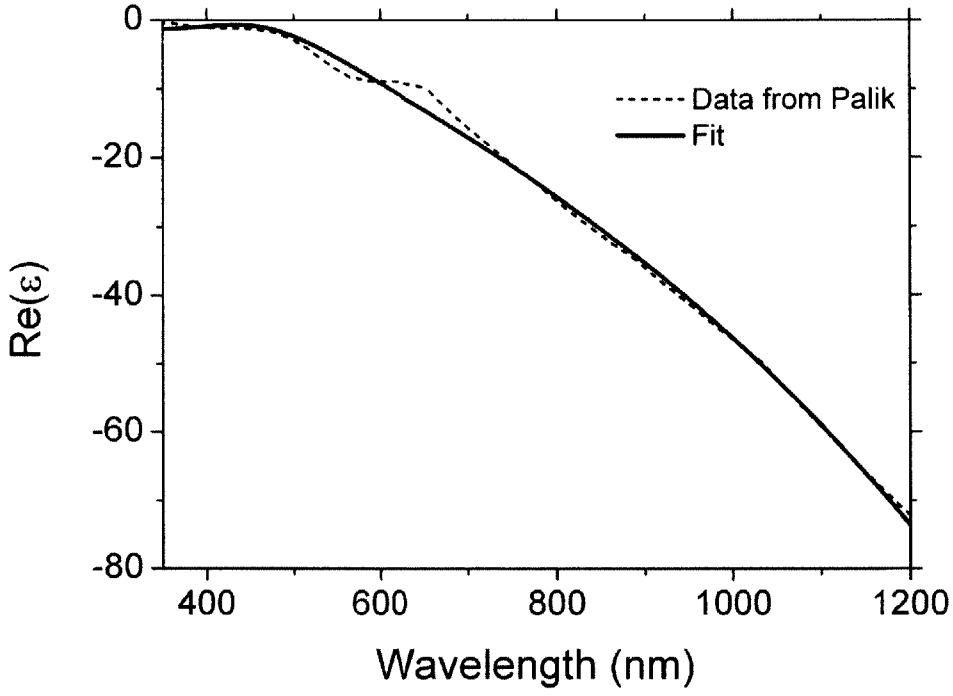

(a)

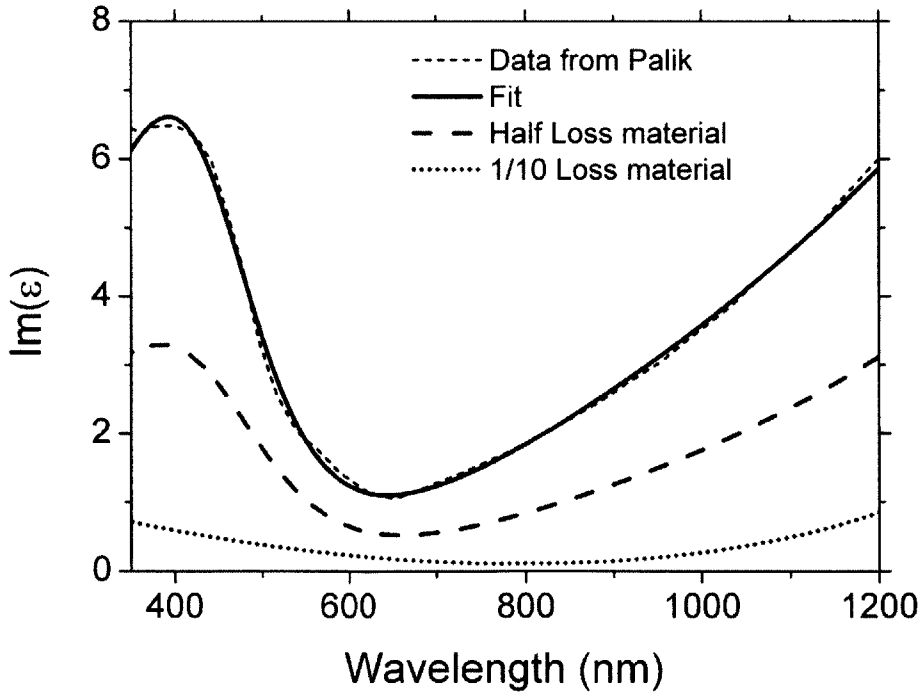

(b)

Figure 8. Dielectric function of gold, used in the FDTD simulations. (a) Real part of the dielctric function. (b) Imaginary part of the dielectric function. The dotted line is a smoothed experimental data from Palik, and the solid like is the FDTD function Fit. The solid dash line and solid dot line represents two artificial materials with reduced Im(ε), by a factor of 1/2 and 1/10, respectively.

3.2. Geometrical specifications

The geometries considered are spheres, circular disks, flat polygons, and star-shaped particles. The edges and corners are rounded with a radius of 15nm, to avoid nonlocal effects and also to take into account the experimental limitations. The thickness of the flat structures is 40nm.

The 3D simulation region is divided into the total field and the scattered field region, where the 6 scattered field power monitors are located outside the box formed by the 6 total field power monitors. The scattered field monitors record only the scattered electromagnetic field. The computation region is shown in Figure 9. The Cartesian (*xyz*) coordinate system is used in the simulation.

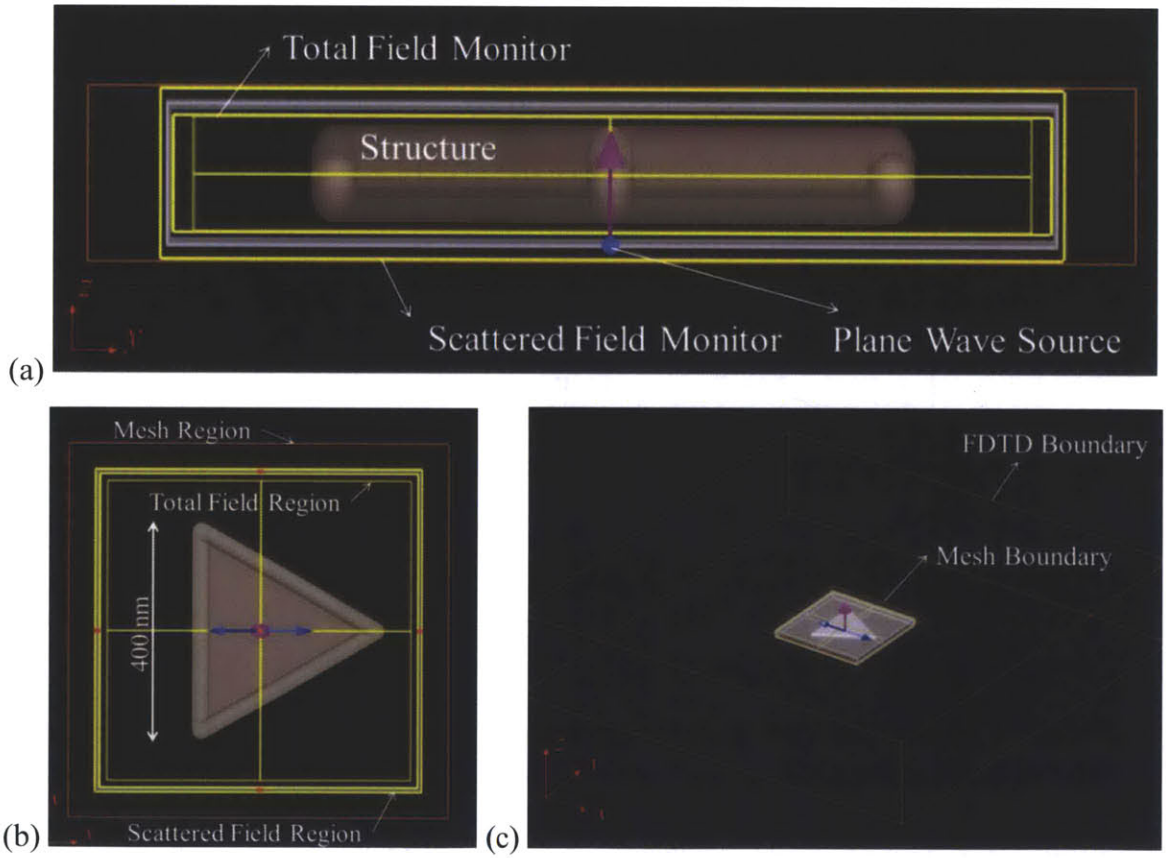

Figure 9. Simulation scheme for Lumerical FDTD Software. The example particle illustrated is a flat gold triangle with edge size 400nm. (a) *y-z* cross section of the simulation region. The linearly polarized plane wave source is located between the total field and scattered field monitor boxes (yellow), propagating towards the positive z direction. (b) *x-y* cross section. The orange box indicates the size of the meshing region. The size of the particle and the monitors (yellow) are shown. (c) The 3D view of the entire simulation space. The small orange box is the meshing region and the large orange box is the total FDTD simulation boundary, where PML boundary condition is applied.

4. Results and Discussion

The FDTD calculation results are discussed in three parts. Section 4.1 presents the optical resonance spectrum of geometric particles with different N-fold rotational symmetry, in order to substantiate the angular grating analogy. Section 4.2 discusses the conversion of the input angular momentum mode (m=1) into a different output mode, which is a result of the interaction with the sub-wavelength nanoparticle. This particle can be analyzed as a mode converter, with a wavelength-dependent efficiency. Finally, section 4.3 discusses the creation of mechanical force and torque that is generated by absorption and scattering at each resonant mode of the nanoparticle. Post-processing of the simulation data is performed by modified Lumerical scripts and MATLAB.

4.1. Verification of the Angular Grating Analogy

In this section, we present the simulation result which verifies the angular grating analogy of chapter 2. We consider planar geometries with different orders of rotational symmetry, and focus on the in-plane resonance excited on the plane perpendicular to the Poynting vector of the excitation. Starting from a circular disk, we extend the discussion to representative polygonal geometries shown in Figure 10. The angular momentum analogy described in section 2.2 is verified in through numerical simulation. Table 1 shows the possible output angular momentum modes excitable from an in-plane, LCP (m=1) plane wave excitation. Figure 10 shows the variation of the number of folds N, and the representative geometries for each of the N-fold rotational symmetries.

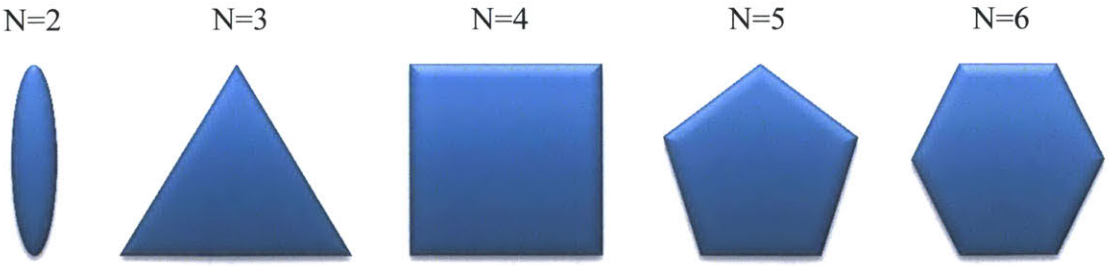

Figure 10. Representative polygon geometries for different N-fold discrete rotational symmetries. N=2 corresponds to mirror symmetry about one linear axis. For higher orders, the representative polygons are triangles for N=3, square for N=4, pentagon for N=5, and hexagon for N=6.

The discrete rotational symmetry exhibited by the nanostructure is expected to govern the possible output modes of angular momentum. FDTD simulation was carried out for the simple representative geometries shown in Figure 10. Table 1 shows a summary of the possible output angular momenta m' for incident light of m=+1, such as a circularly polarized plane wave or a rotating electric dipole.

Table 1. The selection of output angular momentum states by the angular grating rule.

# of folds	possible $m' = m \pm Nj$ output states from m=1 excitation
N=2	**-5 -3 1 3 5**
N=3	**-5 -2 1 4**
N=4	**-3 1 5**
N=5	**-4 1 6**
N=6	**-5 1**

The initial excitation of m=1 includes a far field source of a circular polarized light or a near field source of a rotating dipole, and any combinations in between possessing the same azimuthal order. The possible output modes are limited by the angular grating rule, as shown in Table 1. Note that the excitation of quadrupole resonant mode m=±2 from a circularly polarized beam at normal incidence is only possible with a 3-fold symmetric structure. This is because m'=1±jN=±2 is only possible when N=3 and j=-1. As a result, the quadrupole resonance excited on a 3-fold symmetric structure always has a negative sign, meaning that the direction of phase

rotation with respect to azimuthal angle φ is opposite from the incident circular polarization. This negative quadrupole mode is of particular interest in the following chapters.

For clarity, the optical response is plotted in Figure 11 for a triangular gold nanoparticle with edge length 300 nm, inside a high-index dielectric medium with n=2.35. The size of the triangle is chosen to visualize the first four high-order peaks in the visible-near IR wavelength range. The increase in the refractive index of the dielectric medium both red-shifts the resonance, as explained in 2.1.4. The effect of particle size is discussed in 4.2.6.

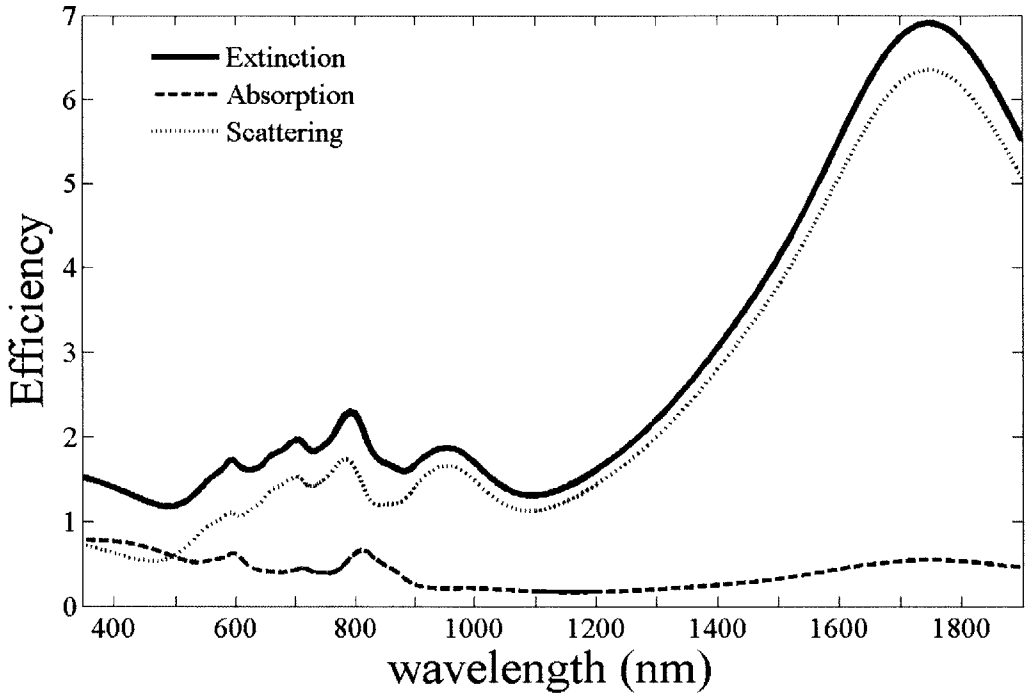

Figure 11. Optical resonance of a 3-fold symmetric plasmonic particle. The extinction (solid), scattering (dotted), and absorption (dashed) are plotted with respect to wavelength. The triangle size is 300nm with 30nm-diameter rounded corners and 40nm thickness, and the surrounding dielectric medium has n=2.35. The absorption and scattering peaks for the same mode occur at slightly different wavelengths, and the absorption peaks correspond to 1715.76nm (m=1), 1044.74nm (m=-2), 814.14nm (m=4), and 706.321nm (m=-5), respectively. The modes in the shorter wavelength region consist of out-of-plane hybrid modes involving variations in the depth direction z.

Figure 11 shows a few discrete modes of multipolar plasmonic resonance of an N-fold symmetric nanoparticle. When an incident electromagnetic field excites different resonant modes of the nanoparticle, an efficient transfer of energy and momentum is expected to happen. For the same particle, the snapshot of the electric field distributions at each mode is plotted in Figure 12. The color shows the phase of $\mathbf{E}_z$, which is the electric field in the z direction. Red and blue colors

represent the positive and negative phase, respectively. The phase change with respect to angle can be counted along the periphery of the particle. The dipole mode (a) shows 2π phase change around the periphery, which corresponds to a rotating dipole.

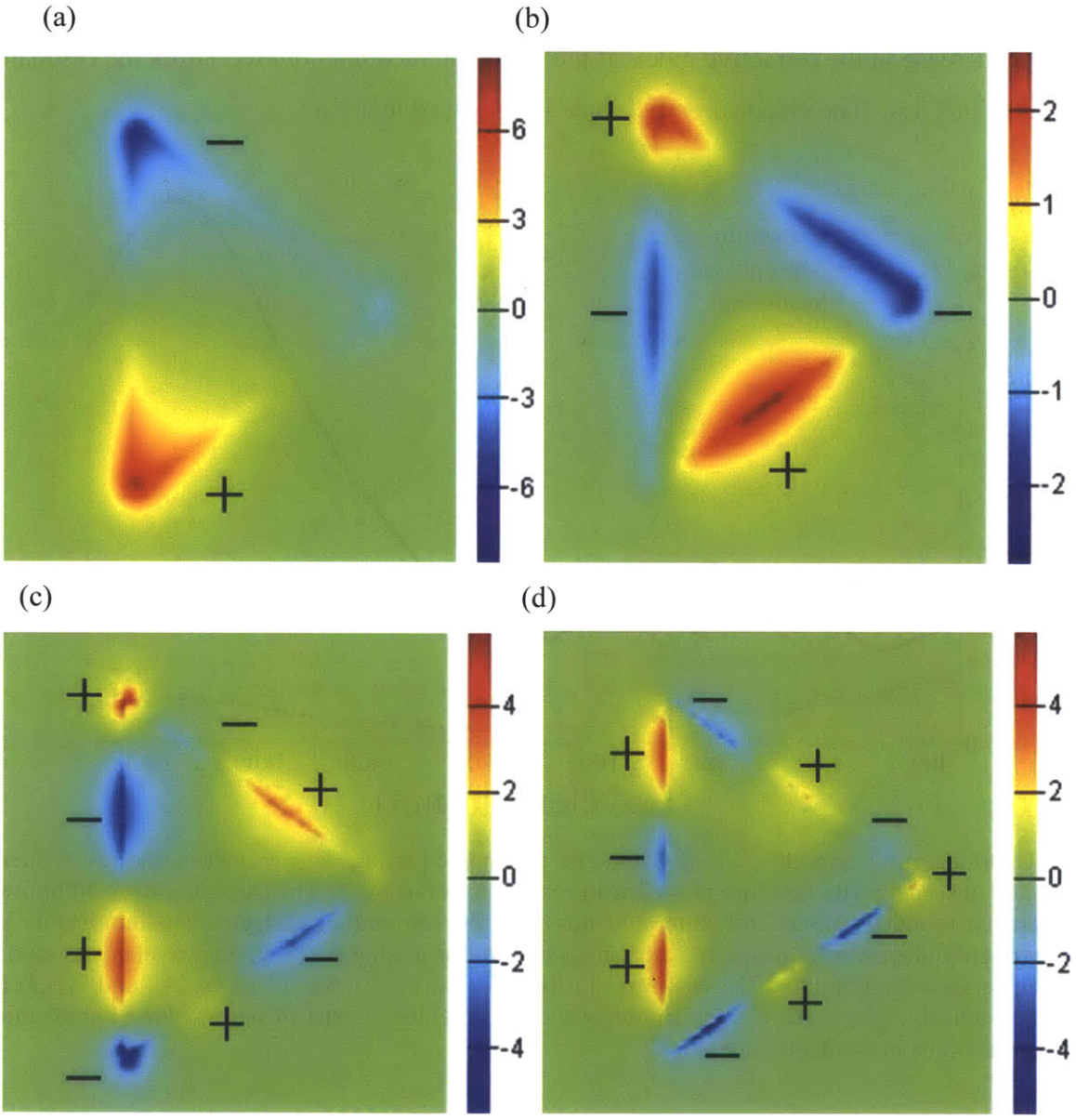

Figure 12. Snapshot of $\mathbf{E}_z$ on the surface of a 3-fold symmetric plasmonic particle. (a) m=1 dipole resonance at 1715.76nm. (b) m=-2 negative quadrupole resonance at 1044.74nm. (c) m=4 octupole resonance at 814.14nm. (d) m=-5 resonance at 706.32nm. The color represents the real part of $\mathbf{E}_z$ in arbitrary units. The distribution is measured with a 2D monitor located 2 nm above the surface. The + and – marks the sign of the electric field.

For a comparison, we also show the first and second non-dipolar modes for a square nanoplate with N=4. The optical response is plotted in Figure 13, and the snapshot of the field in Figure 14. For a square plate, m=-3 mode is observed right after the m=1 mode, skipping the m=-2 mode. The negative quadrupole mode is not excited, because a 4-fold symmetry fails to match angular momentum between dipole and negative quadrupole. The result is in clear accordance with the angular grating rule. The importance of discrete rotational symmetry is highlighted again in 4.2.5, where a triangular particle with N=3 is gradually changed into a hexagonal particle with N=6.

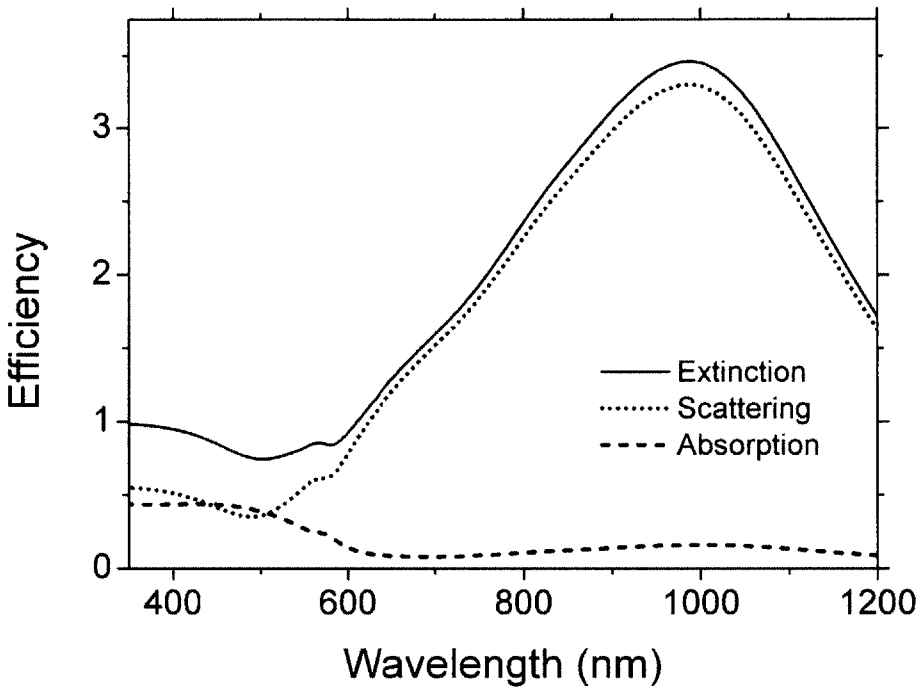

Figure 13. Optical resonance of a 4-fold symmetric plasmonic particle. The extinction (solid), scattering (dotted), and absorption (dashed) are plotted with respect to wavelength. The square size is 400nm with 30nm-diameter rounded corners and 40nm thickness, and the surrounding medium has n=1. The absorption and scattering peaks for the same mode occur at slightly different wavelengths, and the absorption peaks correspond to above 990nm (m=1) and 578nm (m=-3), respectively. The modes in the shorter wavelength region consist of out-of-plane hybrid modes involving variations in the depth direction z.

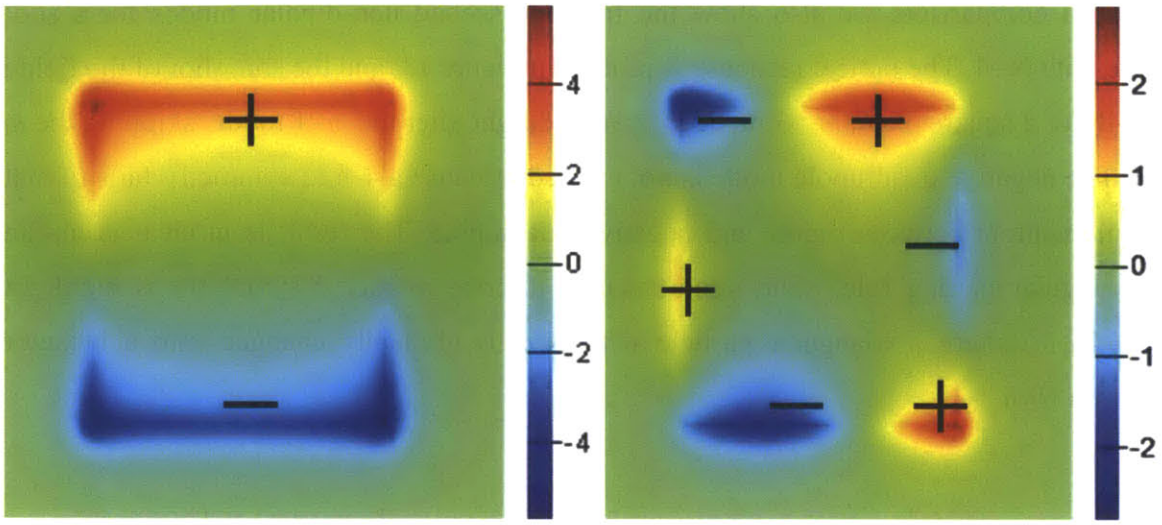

Figure 14. Snapshot of $\mathbf{E}_z$ on the surface of a 4-fold symmetric plasmonic particle. Left shows m'=1 dipole resonance at 990nm, and right shows m'=-3 resonance at 578nm. The color represents the real part of $\mathbf{E}_z$ in arbitrary units. The distribution is measured with a 2D monitor located 2 nm above the particle surface. The particle is identical with the one in Figure 13. The + and – marks the sign of the electric field.

4.2.Angular Momentum Conversion of a Single Plasmonic Resonator

Recent demonstrations suggest that orbital angular momentum of light can offer new information channels for boosting the speed of information transfer in free space [101]. Orbital angular momentum beams have also been used in optical tweezers in order to manipulate particles [102]. Traditional means of modifying the angular momentum state of light include phase plates, q-plates, and pitchfork holograms. These elements can create a phase distribution to a beam of light. The recently demonstrated concept of metasurfaces also provides simple rules in designing photon angular momentum converters [103-105]. All previous designs required the size of the converter to be larger than the size of the light beam, and thus were too bulky for single-photon applications.

Can we reduce the size of the light beam or waveguide to a size comparable to the operation wavelength? This would compress the volume of information carriers and also reduce the distortion from the environment. While classical and quantum information transmission in metallic submicron-waveguide has been studied, the study of angular momentum converters in this small scale is not yet available.

In this chapter, we study the possibility and efficiency of photon angular momentum conversion through a single subwavelength plasmonic resonator. The feasibility of realizing such a subwavelength converter is limited by the strength of the light-matter interaction through localized surface plasmons. We explain how the strong plasmonic resonance can support a high conversion rate which is orders of magnitude higher than the same structure made of dielectrics. In particular, we focus on the conversion rules in subwavelength structures with three-fold rotational symmetry. We find that the symmetry of the angular momentum converter plays a crucial role in the conversion process. This approach may offer great potential in reducing the size of optical angular momentum information converters to micron scale.

4.2.1. Possible Output Modes of a Plasmonic Converter

The angular momentum conversion of a subwavelength particle is based on the angular grating effect, enhanced by the excitation of surface plasmon resonance. Recall that discrete rotational

symmetry governs the output angular momentum modes via the angular grating rule. Each value of m' represents a possible channel for carrying information.

However, not every channel is efficient in capturing the energy from the external field. The most efficient coupling to a particular mode happens when the external driving frequency matches the resonant frequency of the mode. This is demonstrated in Figure 15.

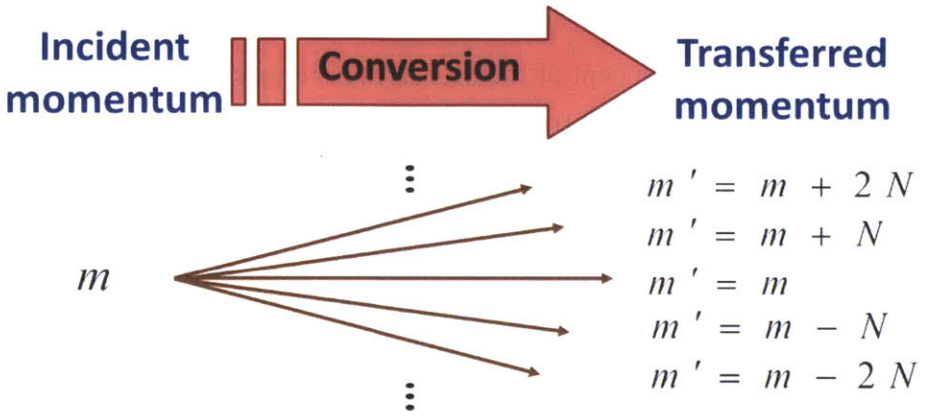

Figure 15. A schematic of the conversion of angular momentum state from m to m', by using a converter which possesses N-fold discrete rotational symmetry. The angular grating effect allows the conversion of incident angular momentum state m to multiple output states m'. A conversion to a particular m' channel is enhanced when the multipolar plasmon resonance matches the azimuthal order m'.

The left side of Figure 15 shows the incident angular momentum state, and the right side shows the possible output angular momentum modes provided by a converter. This is dictated by the N-fold discrete rotational symmetry of the converter geometry. The response can be tuned with the incidence wavelength, with the maximum conversion occurring when the resonant frequency of a particular mode exactly coincides with the excitation frequency.

4.2.2. Dipole to Quadrupole Converter with 3-fold Symmetry

Dipole to quadrupole mode conversion is possible only through 3-fold rotationally symmetric structure, as explained in 2.2.2 and verified in 4.1. This conversion is demonstrated with a simple model system of a triangular gold nanoparticle (or a nanotriangle) in air.

The surrounding medium is set as vacuum (or air) with n=1, for convenience of analysis. The existence of a dielectric medium requires a discussion of the different conventions used to express the momentum of the electromagnetic field, which is discussed in Chapter 5.2.1.

The dimension of the particle is chosen so that dipole and quadrupole resonances occur in the visible to near infrared wavelength range. For this we choose the edge length to be 400nm, thickness 40nm, and the rounding diameter 30nm. The optical response for this configuration is shown in Figure 16.

Because each resonance mode is dispersive, as the broadness of the peaks in Figure 16 indicates, the output angular momentum state at a particular wavelength is a combination of different m' modes. The efficiency of conversion into each angular momentum state will be discussed in the following sections.

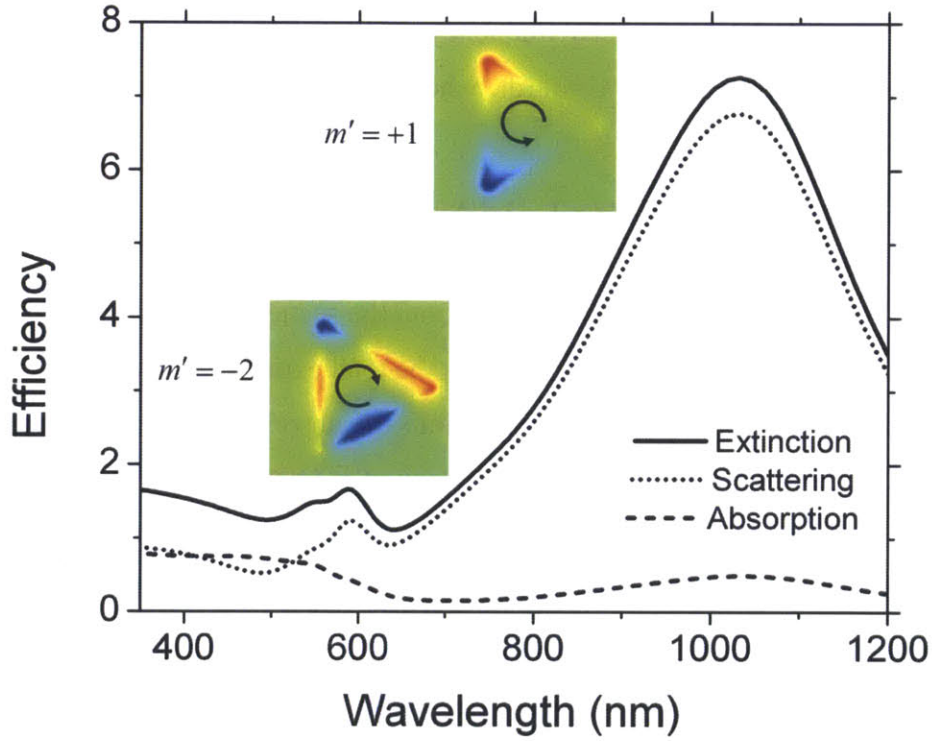

Figure 16. Optical response of a 400nm triangular gold nanoplate inside vacuum (n=1). The extinction (solid), scattering (dotted), and absorption (dashed) efficiencies are plotted with respect to wavelength, and the two resonant modes, dipole (right inset) and negative quadrupole (left inset), are indicated with a snapshot of $\mathbf{E}_z$. The triangle edge length is 400nm with 40nm thickness. The rotating arrows inside the insets indicate the rotation of the phase. CCW direction matches the incidence and CW direction has the opposite sign.

4.2.3. Results from a Plane Wave Source

Let us first consider a plane wave input. The angular momentum state of this plane wave is m=+1, which is a LCP plane wave in z direction. The structure concerned is a triangular gold nanoplate on the x-y plane, as characterized in Figure 16. The incident electric field can be written as:

$$\mathbf{E}_{inc}(\vec{r},t) = \mathrm{Re}(\mathbf{E}_0(\hat{x}+i\hat{y})e^{ik_z z - i\omega t}) \tag{4.1}$$

where the propagation direction z is normal to the surface of the converter. The angular momentum transfer efficiency η can be defined as:

$$\eta = \frac{\omega G}{P_{ext}} \tag{4.2}$$

where G [N·m] is the rate of angular momentum transfer to the response electromagnetic field outside the particle, ω [rad/s] is the angular frequency, and P_{ext} [W=J/s] is the extinction power. G has the same unit with torque, since G=dL/dt, where L is the angular momentum with units [J·s]. G is calculated from (4.3) below:

$$G = \oint_S (\vec{r} \times \overline{\overline{\mathbf{T}}}_{sca}) \cdot d\mathbf{A} \tag{4.3}$$

where $\overline{\overline{\mathbf{T}}}_{sca}$ is the Maxwell Stress Tensor calculated from the scattered electromagnetic field, and S is the closed surface around the nanoparticle. P_{ext} is the total extinction power obtained directly from the simulation, which can be further divided into the absorption and scattering part. The value $\eta/\omega = G/P_{ext}$ represents how much angular momentum is transferred to the output field, per extinguished photon energy. A positive (negative) η indicates that the output field carries a total angular momentum with its sign the same as (opposite to) the input angular momentum. The spectrum of η from the calculation is plotted in Figure 17.

A negative sign of η indicates that the output field carries a total angular momentum of opposite sign from the input angular momentum. We find that η has a dip of negative value at the quadrupole plasmon frequency of the Au triangle. The field profile shows the electric field component normal to the converter surface. Indeed, we see a clear quadrupole mode rotating in opposite direction to the incident excitation. This indicates angular momentum conversion to m'=-2 state at the quadrupole resonance. For a comparison, the field profile away from the

quadrupole resonance and closer to the dipole resonance shows a dipole rotating in the same direction of the external driving field.

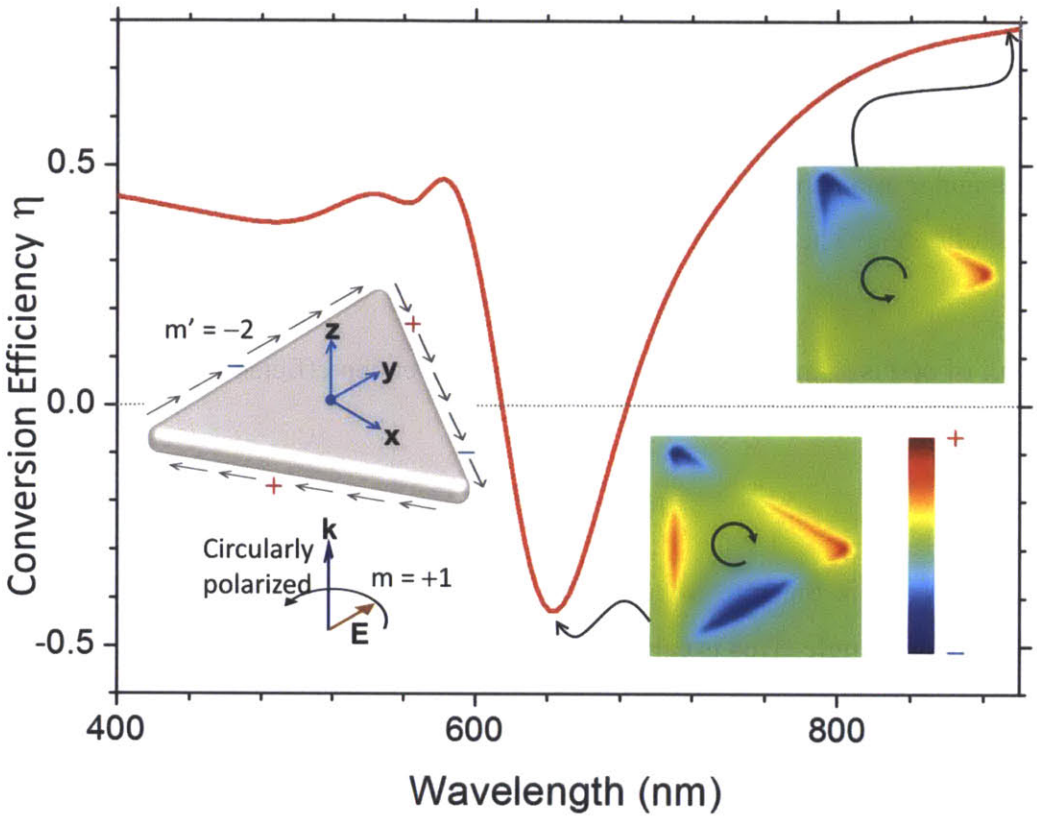

Figure 17. Angular momentum conversion efficiency from a plane wave (far field) source. Left inset shows a left-hand plane wave (m=1) that can be converted to a negative quadrupole (m'=-2) using the resonant properties. Bottom (top) colored plot shows normal electric field 4nm above the surface of the triangular nanoplate at 640 nm (900 nm), representing approximately the corresponding charge distribution.

It should be noted that the total angular momentum is conserved. The loss of the field angular momentum is balanced by the gain of angular momentum within the material. We also note that linear or elliptically polarized incidence also follows the conversion rule because it can be written as a linear superposition of right-hand and left-hand circularly polarized light. In this case, the output will be a superposition between m=+2 and m=-2 quadrupole states. This also explains why quadrupole resonances can be observed in previous works on plasmonic nanotriangles by plane wave excitation. [54], [55].

4.2.4. Results from a Near Field Source

Next, we consider the angular momentum conversion from a near-field source. The same Au nanotriangle is drilled with a small triangular hole at its center, as shown in Figure 18, so that we can place a near-field source in it. The symmetry is undisturbed, and the small hole does not affect the dipole and quadrupole resonances of the nanotriangle.

The angular momentum conversion efficiency can be defined for a near field dipole source as the following. The rotating electric dipole moment in 3D can be expressed as:

$$p(t) = \mathrm{Re}\left(p_0(\hat{x} + i\hat{y})e^{-i\omega t}\right) \tag{4.4}$$

where the unit of p(t) is [Cm], Coulomb meters. The conversion efficiency from this finite source is defined as:

$$\eta = \frac{\omega G_{rad}}{P_{dipole}} \tag{4.5}$$

where $G_{radiation}$ [N·m] is the rate of total angular momentum escaped from a closed surface embedding the nanotriangle. This is calculated from:

$$G_{rad} = \oint_S (\vec{r} \times \overline{\overline{\mathbf{T}}}_{\text{total}}) \cdot d\mathbf{A} \tag{4.6}$$

and P_{dipole} is output power of a dipole source in the presence of the nanotriangle. Similar to the case of plane wave excitation, we find that η has a dip of negative value at the quadrupole plasmon resonant frequency. The radial component of the electric field $\mathbf{E}_r$ close to the outer edges of the nanotriangle can represent approximately the charge distribution of the quadrupole along the outer edges. The converted quadrupole is clearly shown by comparing the plots of $\mathbf{E}_r$ with and without the nanotriangle converter, in the left and right insets of Figure 18 respectively. The field is measured along the circumference of a circle of radius 400nm, centered at the dipole source location, respectively. The field is measured along the circumference of a circle of radius 400nm, centered at the location of the dipole source.

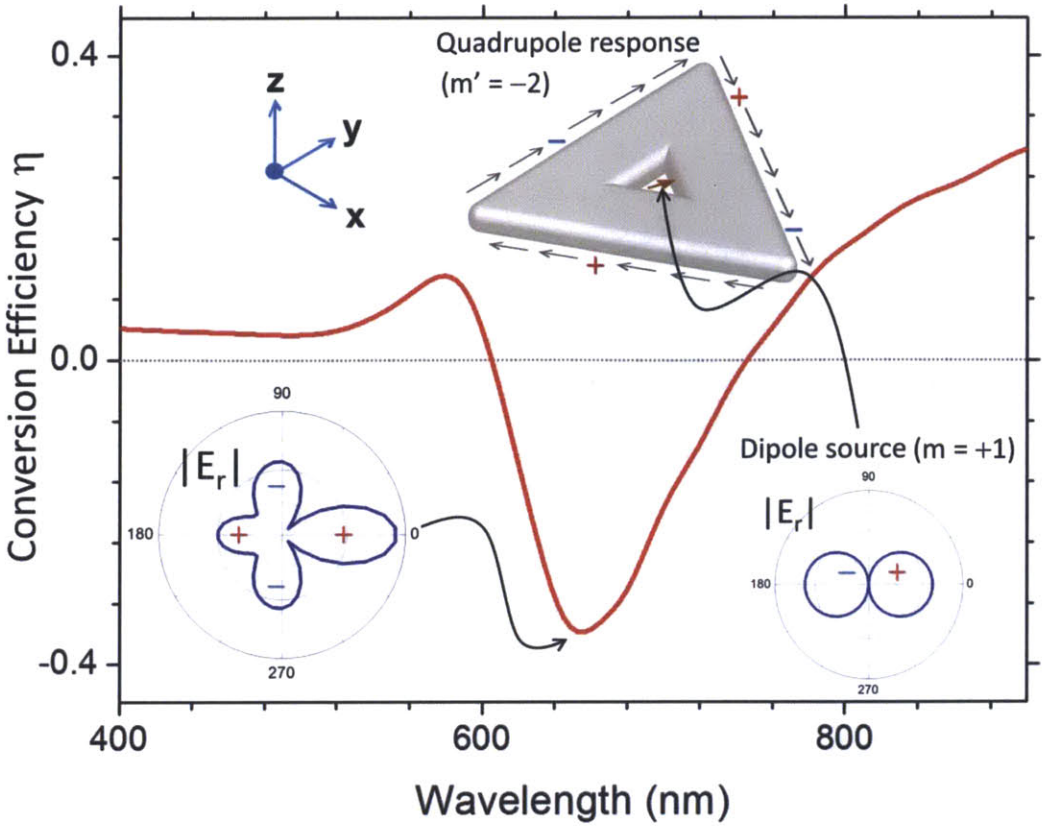

Figure 18. Angular momentum conversion efficiency from a near-field dipole source. Top inset shows a dipole emitter can be converted to a quadrupole emission source using the resonant properties. The radial plot on the left (right) shows the radial component of the electric field 400 nm away from the center of dipole source when the nanostructure is present (absent).

4.2.5. Highlighs on the Importance of Broken Symmetry

Next we explore the effect of the broken rotational symmetry more carefully. The 3-fold discrete rotational symmetry is the key to the high conversion efficiency into the quadrupole mode, quantified by the magnitude of η. Can all particles with 3-fold symmetry such as 6-fold, 9-fold, or circular discs work as a quadrupole mode converter? This is explicitly demonstrated by Figure 19, where change in conversion efficiency is plotted as a triangular particle is gradually modified into a hexagon with 6-fold symmetry. From the result we see that the answer to the above question is 'no'. Once the particle has full 6-fold rotational symmetry, the negative quadrupole contribution disappears because angular momentum cannot be changed by a number of 3 anymore. This can be interpreted that mode conversion is dictated by which symmetry remains

intact and which is broken. In a hexagonal particle, the 6-fold symmetry remains intact and therefore governs the conversion behavior.

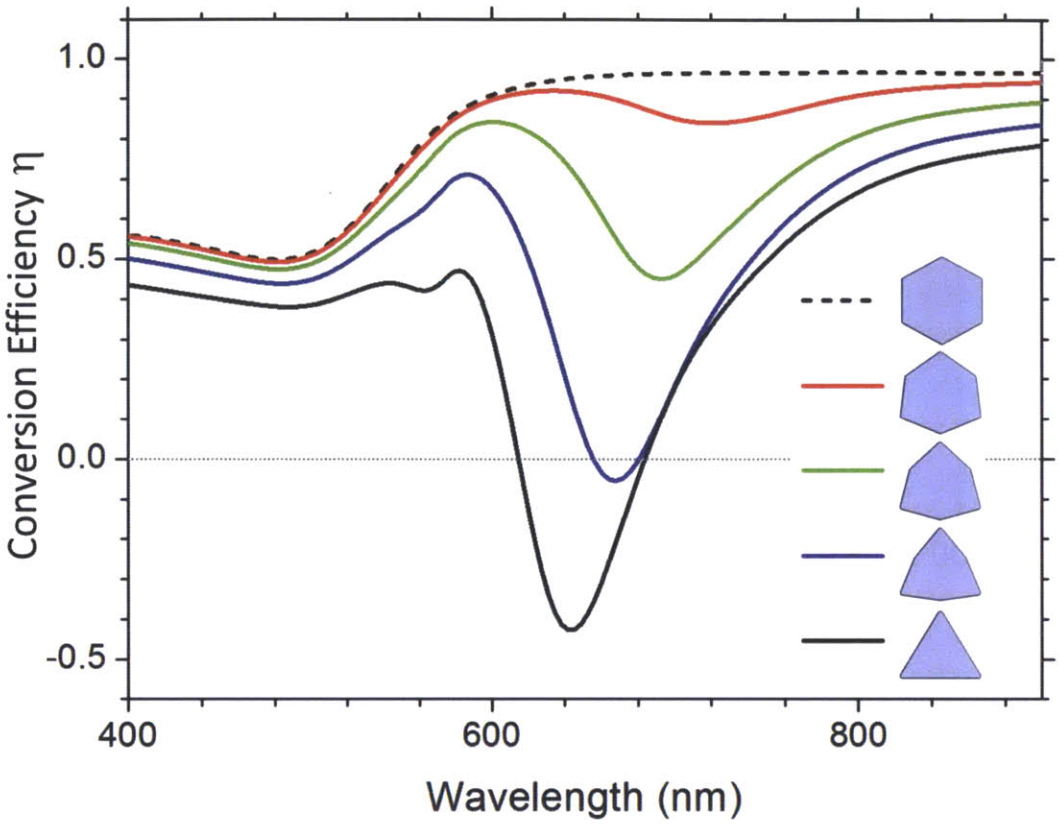

Figure 19. Comparison of the conversion efficiency between 3-fold and 6-fold symmetric converters. A smooth change from 6-fold symmetric hexagon to 3-fold symmetric triangle is observed. The momentum conversion onto the negative quadruple mode is only possible by a 3-fold symmetric structure, and not by the 6-fold symmetric structure.

4.2.6. The Effect of Particle Size

The size of the plasmonic angular momentum converter also determines whether the conversion process is benefitted from quadrupole resonance. Higher order plasmon resonances with short plasmon wavelength are usually lossy because of the small group velocity. Therefore, larger size converter is preferred for a given passive material. Figure 20 shows that the critical size for a Au nanotriangle of thickness 40 nm is ~300 nm, with the corresponding operation wavelength ~600 nm.

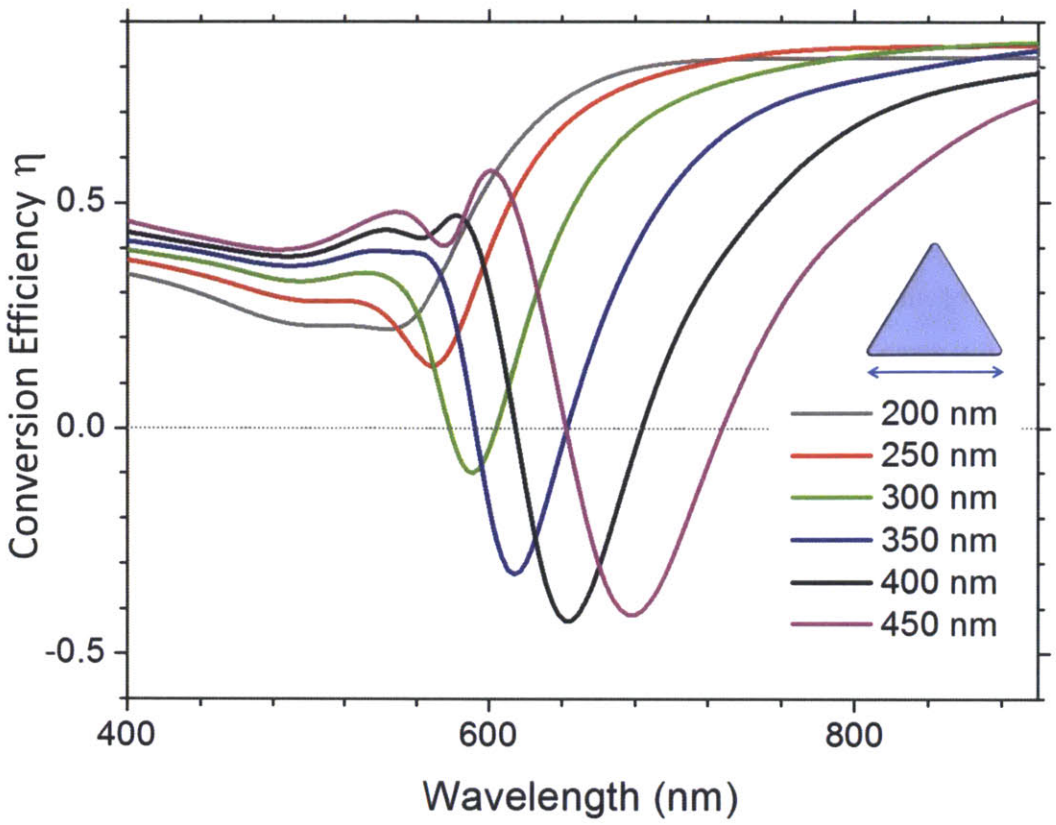

Figure 20. The size dependence of the conversion efficiency. An optimum size exists for a maximum conversion efficiency. The results for a varied edge length of 200nm (gray), 250nm (red), 300nm (green), 350nm (blue), 400nm (black), and 450nm (magenta) are plotted.

The conversion efficiencies of negative angular momentum conversion we obtained so far are only around -0.4, which is quite different from the theoretical value -2 for clockwise quadrupole. It should be noted that a pure angular momentum state of the order m should have $\eta=m$'. Energy absorption and the contribution of broadband dipole resonance are the two main reasons for such a reduction of efficiency. Material with low absorption coefficient and gain medium may be helpful in enhancing the efficiency in later designs.

4.3. Mechanical Effects at Multipolar Plasmon Resonance

Optically induced mechanical forces arise from scattering and absorption process. Both the absorbed field and the scattered field transfer the momentum and angular momentum to the target object. This section discusses the mechanical effects caused by optical scattering and

absorption of a plane wave, incident on a plasmonic resonator at different multipolar resonances. The first two sections explain how the mechanical effects from absorption and scattering are quantified. Next, the calculation results for Force and Torque are presented with a focus on the varied size, shape, and material of the object, which determines the quality of the plasmon resonance of the particle.

For all of the data presented, the direction of force is parallel to the direction of propagation ($\hat{k}$), which is $+z$ in the simulation. The direction of torque is $+z$ as well, which is the same as the axis of rotation for the circularly polarized incident field. The force and torque in all the other directions are equal to zero, due to the symmetry of the particle in the depth direction, and also due to the circularly polarized field containing exactly the same amount of x-polarized and y-polarized components.

4.3.1. Calculation of the Mechanical Effects

Depending on the relative size of the cross sections, people categorize absorption-dependent and scattering-dependent particles. It is commonly understood that the extinction becomes absorption-dependent as the particle size decreases to be much smaller than the wavelength. Both processes are enhanced at resonance, and the maximum efficiencies are achieved when the particle is in strong plasmonic resonance with the incoming field.

While comparing the magnitude of C_{abs} and C_{sca} can clarify the relative magnitude of the scattered and absorbed fields, it fails to represent the relative importance of the two processes in generating force or torque. In other words, cross section values cannot yield the complete information about the light-induced mechanical effects. This is because the output momentum and angular momentum carried by the scattered electromagnetic field can have a significant effect on mechanical effects. For a same scattering cross section, the effect of scattering can be different depending on the distribution of the electromagnetic field as well as the polarization and direction of scattering. All of these factors would affect the resulting mechanical force and mechanical force and torque. The calculation methods to separately account for scattering and absorption are presented in 2.3.4.

4.3.2. Particles with Perfect Rotational Symmetry

The magnitude of the light-matter interaction reaches its peak when the particle is excited at its plasmon resonance. This resonance can first be tuned by changing the size of the particle, without altering the shape. Between scattering and absorption, which process dominates momentum transfer and angular momentum transfer? First, spherical nanoparticles with perfect rotational symmetry are studied.

Figure 20 shows the extinction efficiency for spherical gold nanoparticles with various radius, from 50nm to 200nm. While small nanoparticles have absorption-dominant extinction, larger nanoparticles exhibit increasingly scattering dominant behavior. The magnitude of the absorption efficiency being nearly consistent represents that the number of photons absorbed depends mostly on the cross sectional area of the nanoparticle, in this size range.

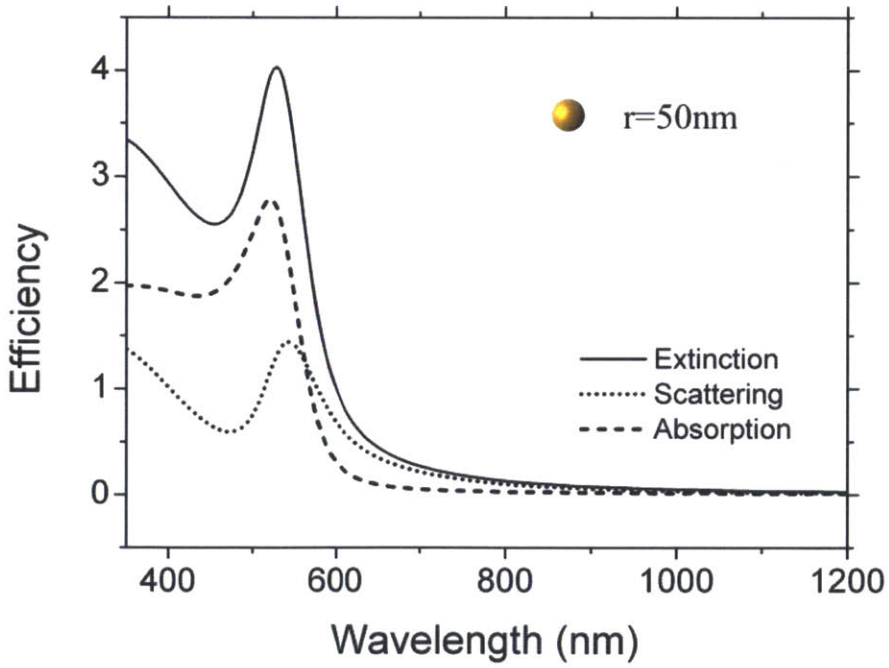

(a)

Figure 21. The optical response of a spherical gold nanoparticle. (a) r=50nm. (b) r=100nm. (c) r=150nm. (d) r=200nm. Extinction (solid), scattering (dotted), and absorption (dashed) are plotted together.

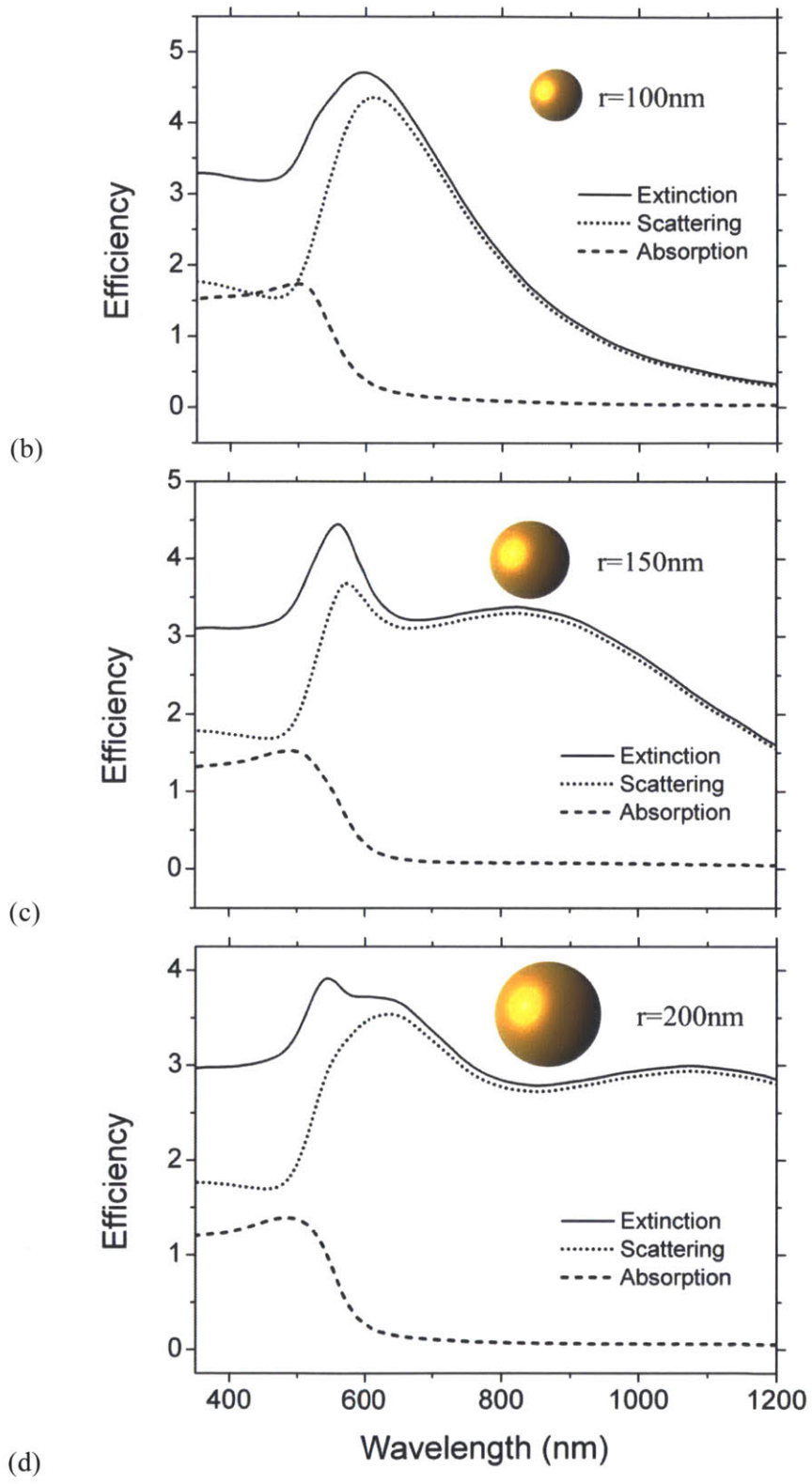

Figure 21. The optical response of a spherical gold nanoparticle. (a) r=50nm. (b) r=100nm. (c) r=150nm. (d) r=200nm. Extinction (solid), scattering (dotted), and absorption (dashed) are plotted together.

For the same particles, the force and torque are plotted in Figure 22 and Figure 23, respectively. While the force comes largely from scattering, the torque comes entirely from absorption. Scattering-induced torque vanishes due to the two terms for the incident and scattered fields in (2.57), cancelling each other out completely. This indicates that the angular momentum is not altered for the portion of the field that is scattered. Therefore, the scattered photons do not produce any mechanical torque. For a rotationally symmetric particle, absorption is the only mechanism to achieve angular momentum transfer.

Our focus is to analyze the mechanism of angular momentum transfer to plasmonic particles with different modes of resonance. The magnitude of torque produced by absorption can be calculated using (4.9), which is proportional to the absorption cross section. From Figure 21, we find that the absorption efficiency for particles larger than r=100nm do not vary as the particle size increases, meaning that the torque scales with the cross sectional area of the spherical particle, instead of the radius or the volume.

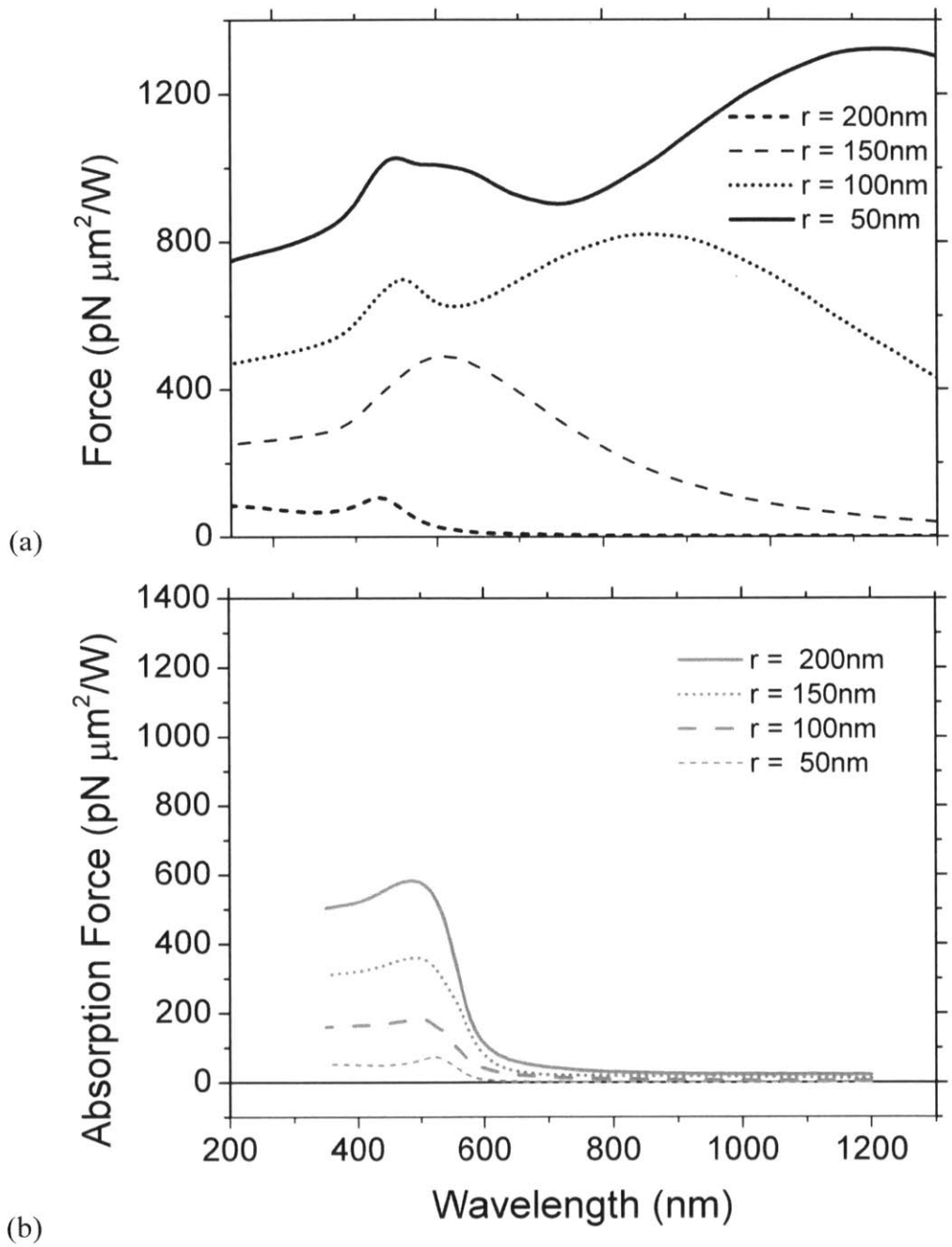

Figure 22. Light induced force on a spherical gold nanoparticle. The top (a) shows total force, and the bottom (b) shows the force from absorption. The difference between the two is the scattering-induced force. The lines indicate the size variation of 200nm (solid), 150nm (dotted), 100nm (dashed), and 50nm (short dashed).

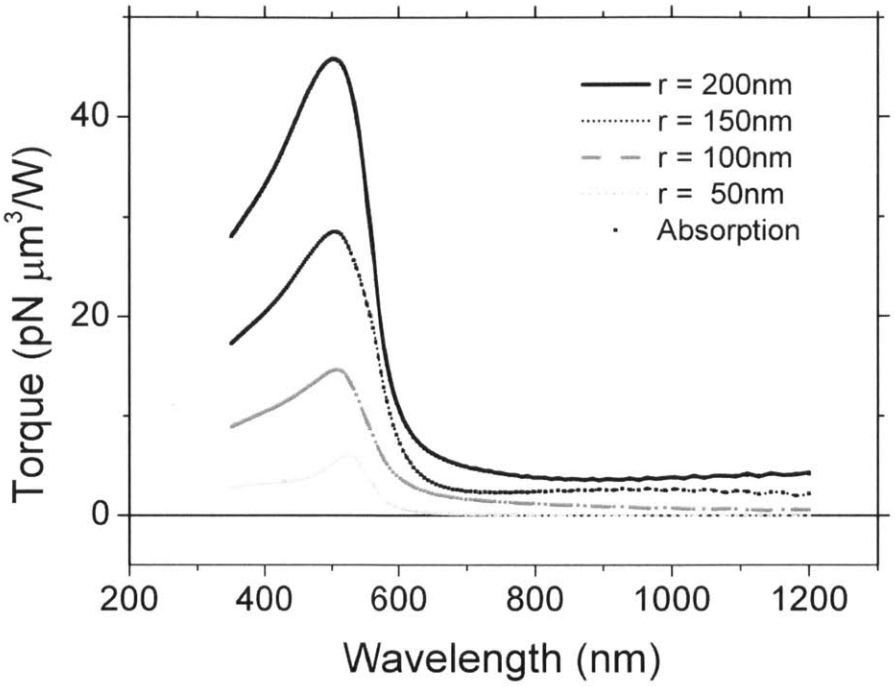

Figure 23. Light induced torque on a spherical gold nanoparticle. 100% of the torque comes from absorption. The lines indicate the size variation of 200nm (solid black), 150nm (dotted black), 100nm (dashed dark gray), and 50nm (dotted gray). The torque from absorption is plotted with square markers for all four curves, and shows an exact match with the total torque.

A thin circular disk with the same cross section is simulated next. A gold disk with r=200nm and thickness of 40nm is simulated and the extinction efficiency, force, and torque are plotted in Figure 24.

A comparison between the graphs (a) and (b) of Figure 24 shows that the force generally follows the trend of the extinction, but careful examination shows that they do not scale perfectly into each other. Higher extinction cross section results in a larger optical force, yet the total force resulting from scattering does not come from all of the scattered photons possessing identical values of output momentum. Instead, the scattered photons possess very different values of output momentum. Some of the photons go through a very large change in momentum, such as the backscattered photons, while other photons do not undergo such a big change. The total force is a summation of all such effects.

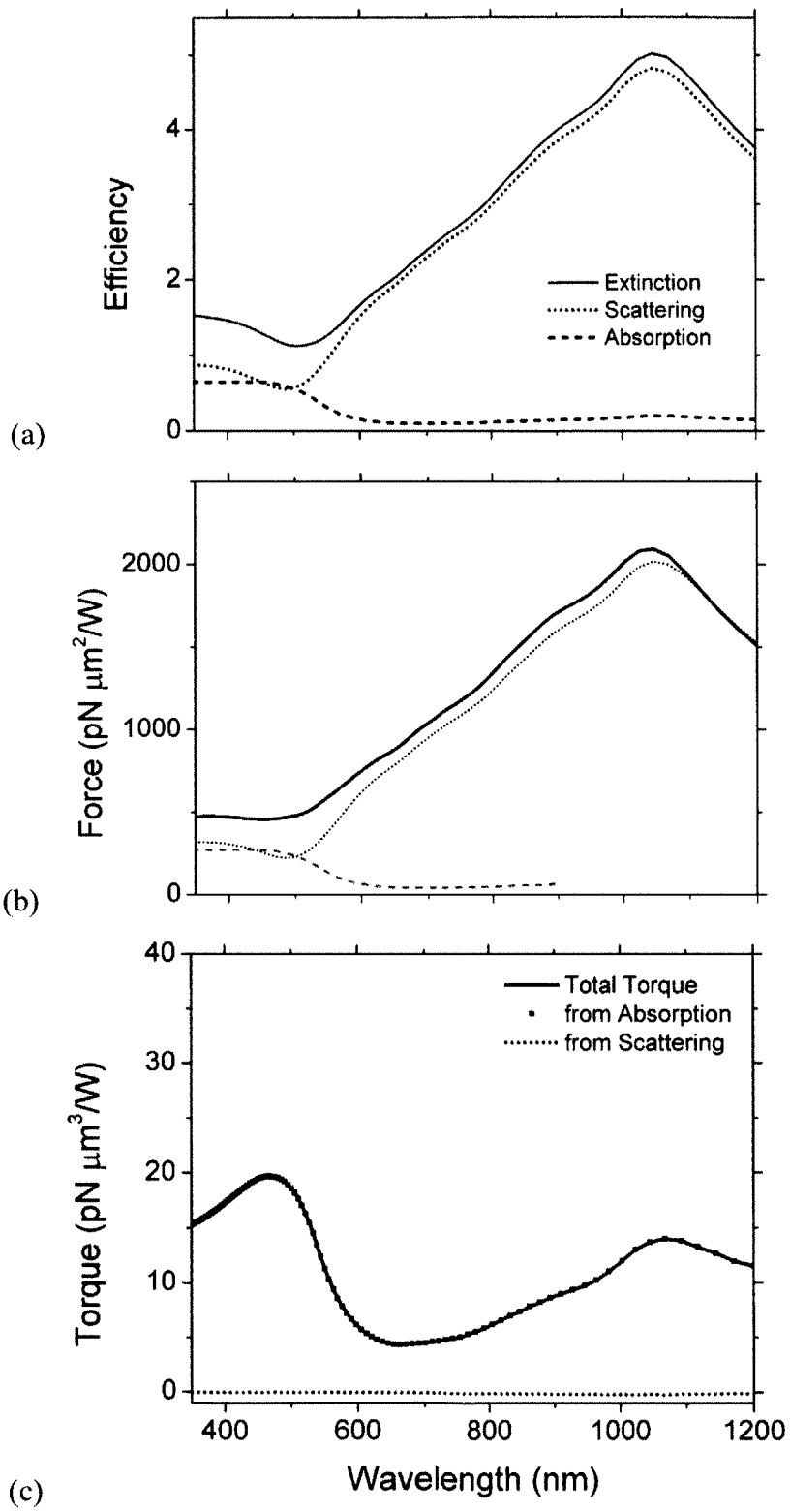

Figure 24. Optical response of a circular gold nanoplate with r=200nm. (a) extinction (solid), scattering (dotted), and absorption (gray dashed) efficiencies. (b) Force applied to the particle. (c) Torque applied to the particle, where 100% of the total torque (solid) and the torque from absorption (square marker) overlap exactly. The torque from the scattered field is zero.

Because two distinctive peaks are observed in Figure 24, the electric field distributions corresponding to the two different modes are plotted in Figure 25.

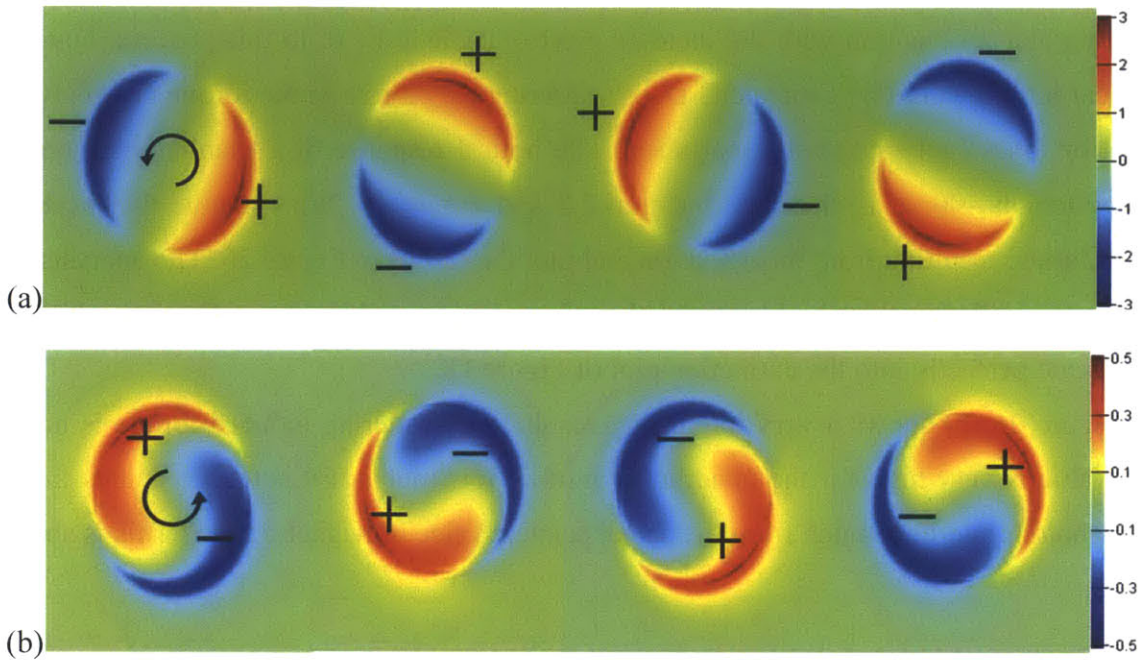

Figure 25. Snapshot of $\mathbf{E}_z$ on the surface of a circular gold nanoplate. (a) m=1 dipole mode at 900nm excitation, (b) another mode with a different radial distribution, while azimuthal order is still m=1 (at 457nm excitation.) The color represents the real part of $\mathbf{E}_z$ in arbitrary units. The distribution is measured with a 2D monitor located 2 nm above the surface. The + and – marks the signs of the electric field, and the rotating arrow indicates the direction of phase rotation. CCW matches with the incident illumination.

The torque plotted in graph (c) of Figure 24 shows that 100% of the torque comes from absorption. This confirms that for particles exhibiting perfect rotational symmetry, the only possible means of angular momentum transfer is absorption. Scattering does not produce any torque on a perfectly symmetric particle.

The angular momentum number of both resonance modes in Figure 25 are m'=1. The rotationally symmetric object has no means of converting the incident angular momentum m=1 into a different mode. While the radial field distribution varies from mode to mode, the angular distribution is still exactly the same, and scattering produces no mechanical torque on the nanoparticle.

4.3.3. Particles with Discrete Rotational Symmetry

We know from the results of 4.2.3 that the scattered output field carries a significantly different value of angular momentum with the incident electromagnetic field. In this process, how much mechanical torque would be generated? Does scattering play a role in the torque transfer, unlike the case for rotationally symmetric particles? The optical response of a triangular nanoparticle with edge length 400nm is characterized in 4.2.3 and Figure 16. We examine the mechanical force and torque resulting from this situation and plot the results in Figure 26. The analysis of the force is very similar to that for Figure 24 (b). The graph resembles the extinction, although it does not scale perfectly into the extinction plot of Figure 11.

Figure 26 (b) shows a very interesting result. The scattering-induced torque is nonzero, and the value is very high for the quadrupole mode. How much of this torque comes from the incident photons and how much from the actual scattered electromagnetic field? This is shown in Figure 27.

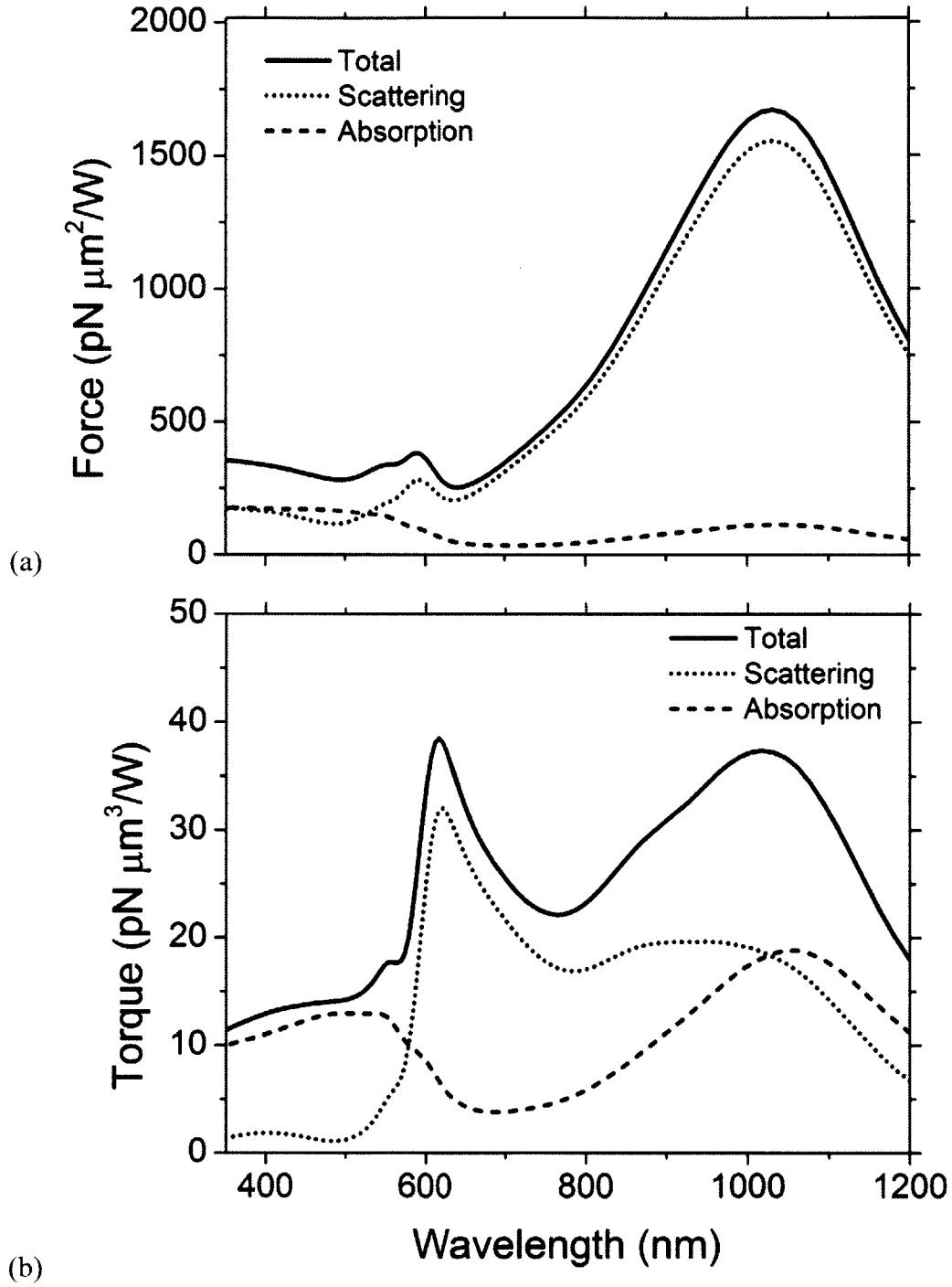

Figure 26. Force and torque due to scattering and absorption from a triangular gold nanoplate. (a) F orce applied to the particle, which resembles the extinction efficiency profiles and is largely scattering dependent. (b) Torque applied to the particle. Total value (solid), scattering-induced value (dotted), and absorption-induced value (dashed) are plotted together.

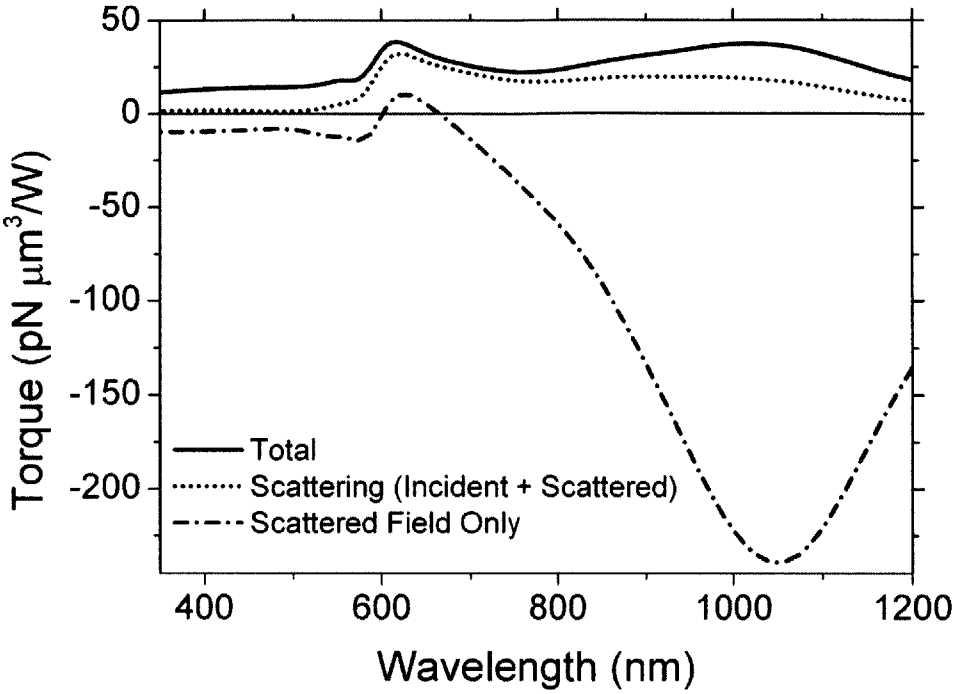

Figure 27. Torque from the scattered field due to angular momentum conversion. The total torque (solid), torque from scattering (dotted), and the torque from the output scattered field (dot-dashed) are plotted together.

In the scattering process, the net torque is close to zero when the scattered electromagnetic field carries the same angular momentum as the incident field. This exactly cancels out the net torque transferred to the particle. While this was the case for the rotationally symmetric particles, this is not true for the case shown in Figure 27, due to the effect of angular momentum conversion. Here, the scattered field does carry exactly the same value of angular momentum compared to the incident field. In fact, the scattered electromagnetic field imparts a positive torque onto the particle near the plasmon resonance peak.

The magnitude and direction of scattering depends on the distribution of the nearfield enhancement on the surface of the plasmonic nanoparticle. The snapshot of electric field distribution on the surface of the particle is plotted in Figure 28 for the dipole and quadrupole modes. The negative direction of rotation of the quadrupole mode is expected to affect the angular momentum carried by the scattered field, in an opposite manner compared to the positive dipole mode.

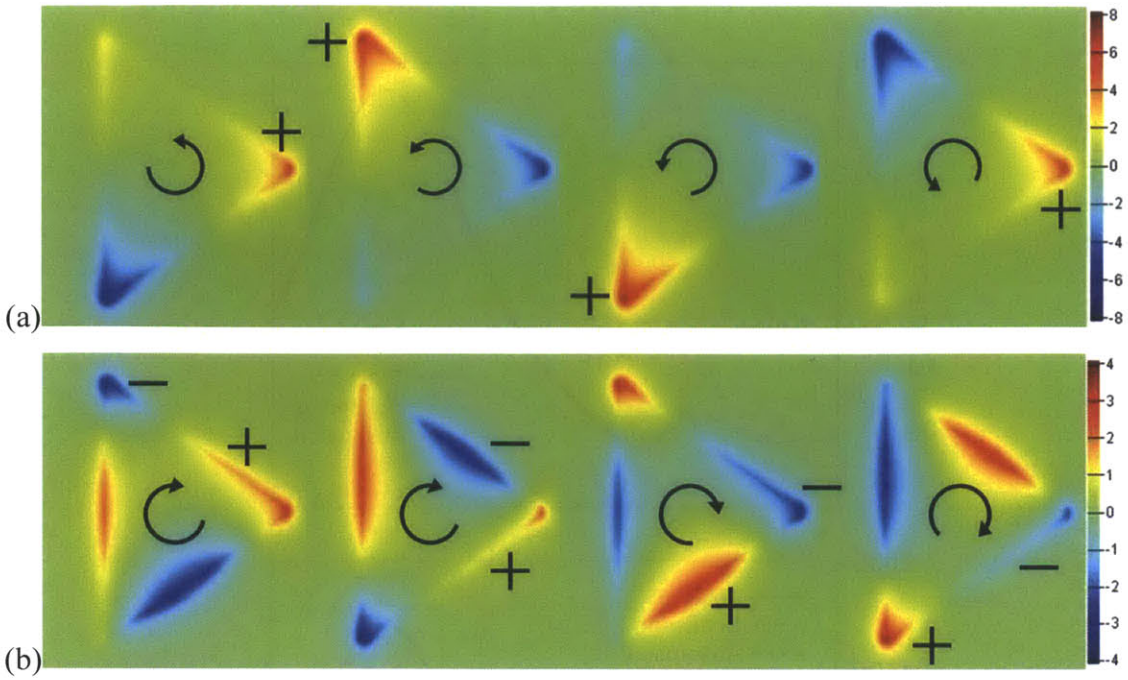

Figure 28. Snapshot of $\mathbf{E}_z$ on the surface of a triangular gold nanoplate. (a) m=1 dipole mode at 900nm excitation, (b) m=-2 quadrupole mode at 634.4nm. The color represents the real part of $\mathbf{E}_z$ in arbitrary units. The distribution is measured with a 2D monitor located 2 nm above the surface. The + and – marks the signs of the electric field, and the rotating arrow indicates the direction of phase rotation. CCW matches with the incident illumination.

4.3.4. Material Variation: Effect of the Reduction in Loss

The large transfer of angular momentum of the negative quadrupole mode comes from the enhanced scattering, which is dictated by the particle geometry rather than the material characteristics. In order to show this more clearly, two materials are simulated with an artificially reduced Im(ε), modified from the dielectrif function of gold. Their material characteristics are plotted in Figure 8. Since reducing Im(ε) decreases absorption, we expect that the quadrupole peak would not decrease when as Im(ε) is lowered, while the dipole peak does. For a triangular nanoparticle, the data for half-loss gold, of which Im(ε) is modified from gold with a factor of 1/2, are plotted in Figure 29. The data for one-tenth-loss gold, of which Im(ε) is modified from gold with a factor of 1/10, are plotted in Figure 30.

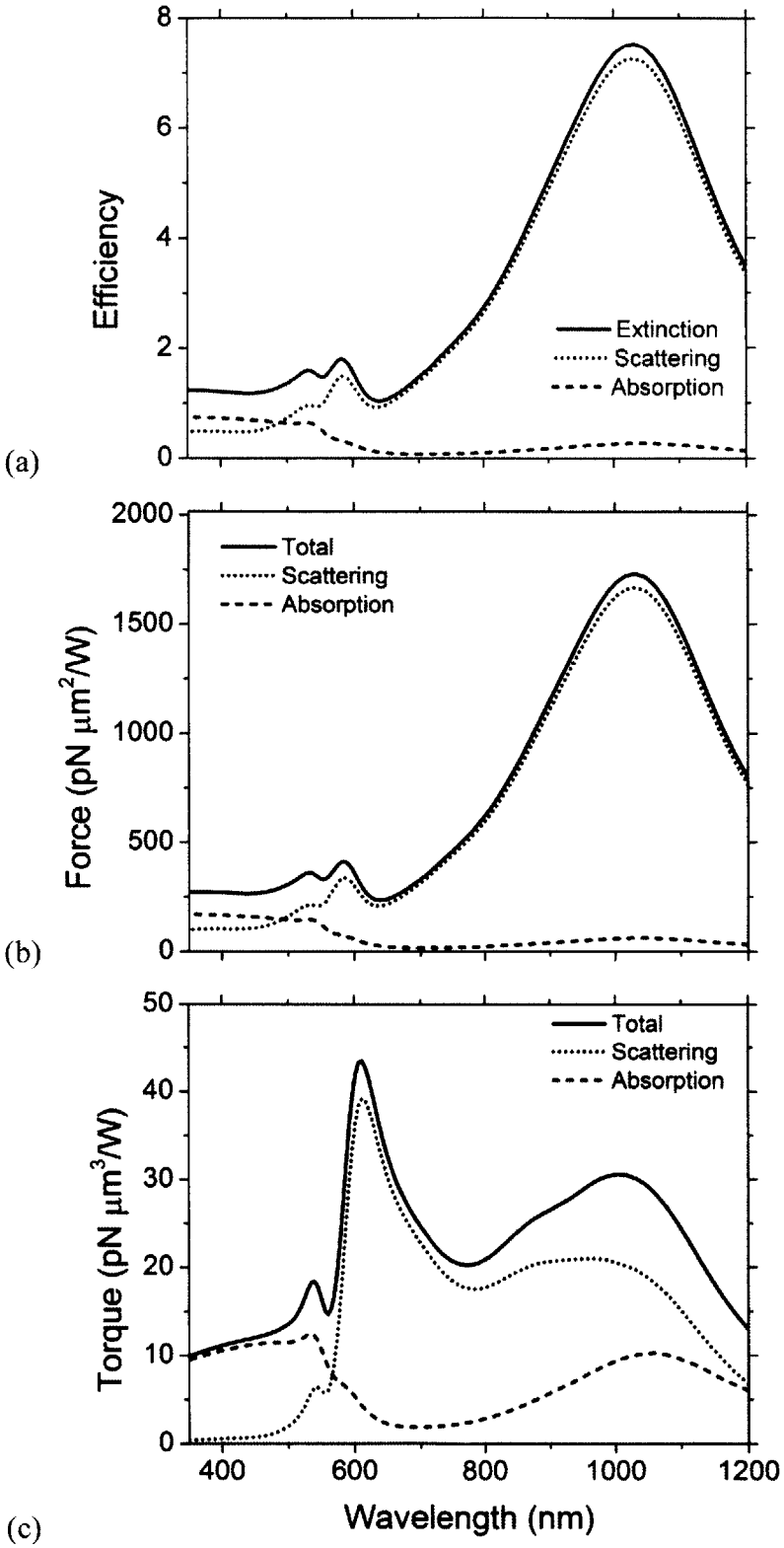

Figure 29. Optical response of a triangular nanoplate, made of gold with reduced loss of $0.5\times\mathrm{Im}(\varepsilon)$. (a) Extinction (solid), scattering (dotted), and absorption (dashed) efficiencies are plotted together. (b) Force applied to the particle. (c) Torque applied to the particle.

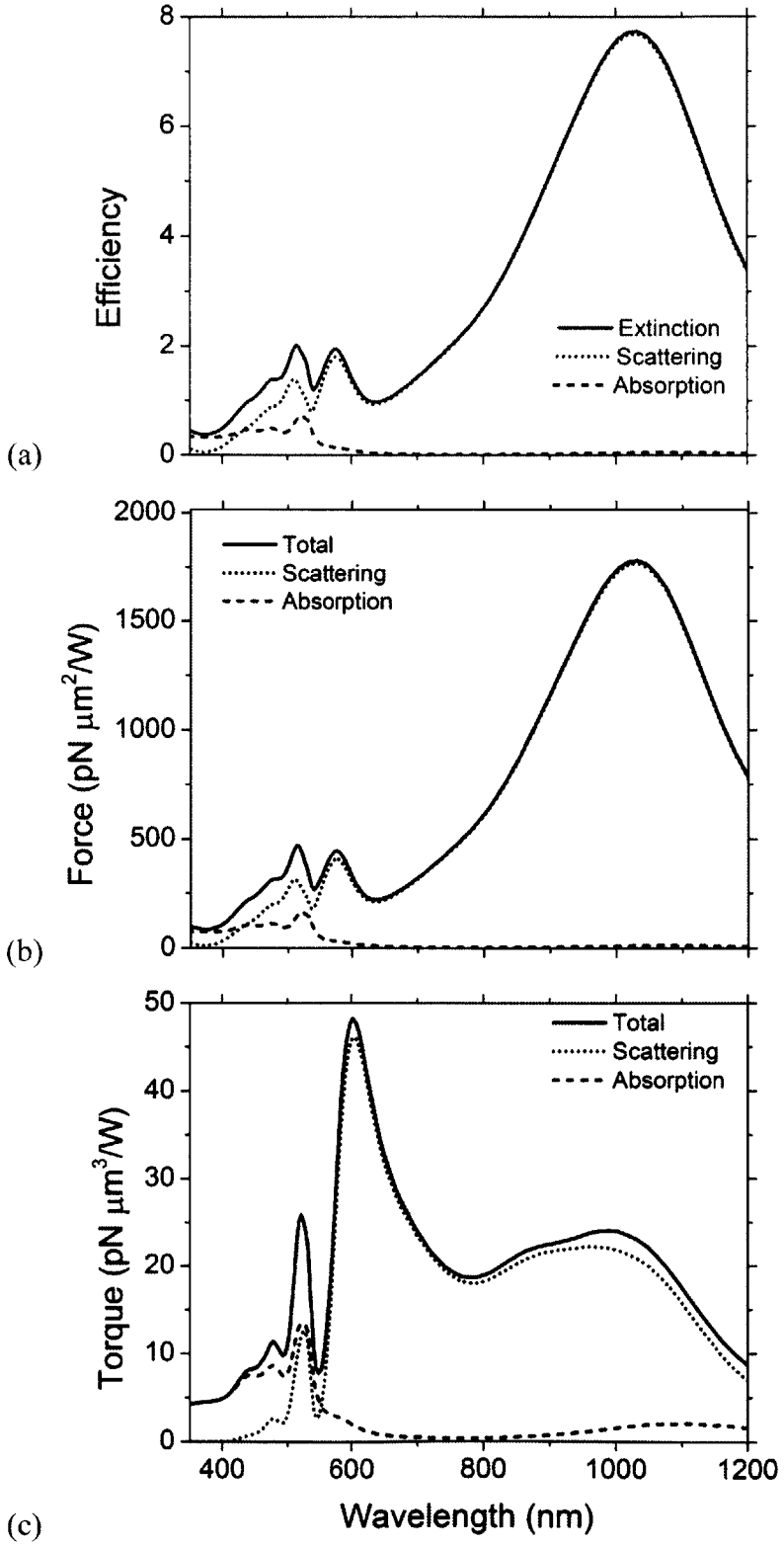

Figure 30. Optical response of a triangular nanoplate, made of gold with reduced loss of $0.1\times\mathrm{Im}(\varepsilon)$. (a) Extinction (solid), scattering (dotted), and absorption (dashed) efficiencies are plotted together. (b) Force applied to the particle. (c) Torque applied to the particle.

One can immediately notice that reducing Im(ε) suppresses the absorption-induced force and torque dramatically, while the scattering-induced effects are only slightly modified. As expected, the torque at the dipole mode decreases to almost half the original value, while the torque at the quadrupole mode, which is dominated by scattering, slightly increases and do not show a significant change. In conclusion, the light-induced torque applied at the dipole and quadrupole plasmon resonance arises from different phenomena.

Torque at the dipole mode of a triangular particle arises from the mixed effect of scattering and absorption, and the absorption-induced part is suppressed when Im(ε) is decreased. Torque at the quadrupole mode, on the other hand, arises mainly from scattering. This geometry-driven effect is changed only a little by the modification of Im(ε).

As a comparison, we plot the case of how absorption-dominant torque is modified when the material loss is reduced. Circular disks with perfect rotational symmetry are simulated with varied Im(ε), and plotted below in Figure 31. The same geometry as Figure 24 is used with the radius of 200nm.

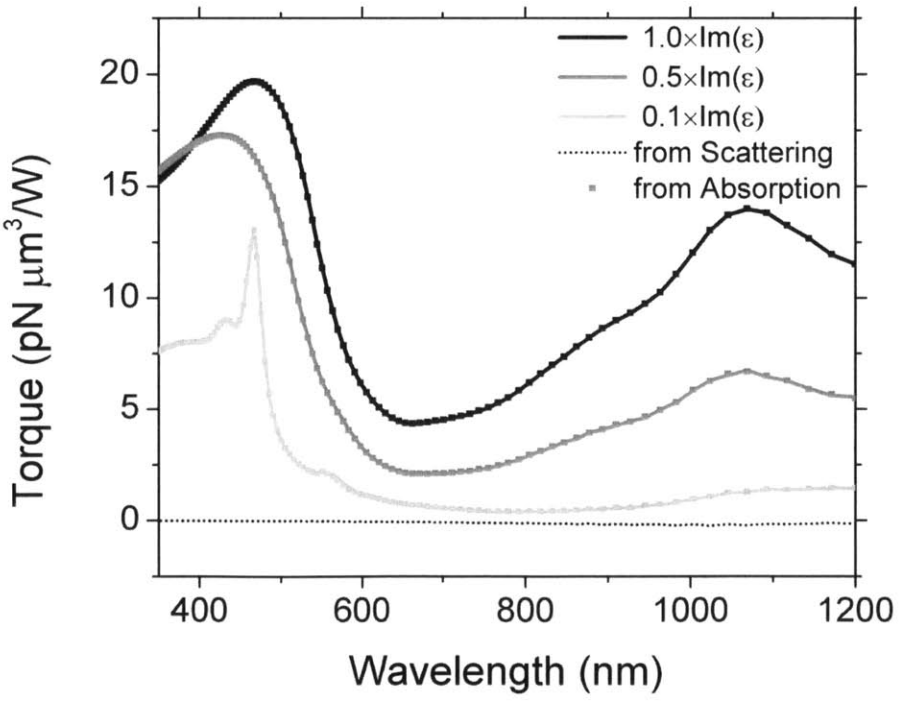

Figure 31. Light induced torque on a circular gold disk, for materials with reduced loss. Colors represent the different materials, black for gold with full loss, dark gray for gold modified to half loss, and light gray for gold modified to 1/10 loss. For all three cases, the torque contribution from scattering is zero. Contribution from absorption is plotted in square markers.

From Figure 31, the absorption-induced torque is highly governed by the imaginary part of the dielectric function. All of the torque applied on a disk is a result of absorption, and this torque decreases proportionally when Im(ε) is reduced.

It should be noted that the kinks seen in the 1/10-loss material result is not a physical peak but rather an unsteady effect arising from Im(ε) approaching zero. When the imaginary part is decreased even further, the data turns unstable below 550nm and the convergence is lost.

In conclusion, we confirm that torque is unusually enhanced at negative quadrupole resonance mode, where angular momentum conversion occurs. This large torque comes from scattering instead of absorption, which is an unusual finding for irrotational geometries. While absorption is generally regarded as the major mechanism of spin angular momentum transfer from light to matter, scattering can produce a larger contribution at certain non-dipolar resonance modes, due to the scattered field carrying a different value of angular momentum from the incident field.

5. Summary and Outlook

5.1. Summary

We numerically investigate the light-matter interaction of a single plasmonic resonator, focusing on the transfer and conversion of angular momentum at different multipole resonances.

First, the angular grating analogy is presented to explain how the field distribution around a plasmonic structure at resonance is dictated by two factors: (1) the angular momentum state of the incident light, and (2) the broken rotational symmetry of the structure. The theory is validated by FDTD numerical simulation for geometries with varied rotational symmetry.

Next, we propose using a subwavelength plasmonic nanoparticle as an optical angular momentum converter in free space. The broken rotational symmetry of the structure dictates the angular momentum channels supported by a single converter. The conversion efficiency is governed by the quality of the plasmon resonance. The efficiency of the conversion is analyzed in detail for a triangular converter possessing 3-fold symmetry, which allows conversion from a dipole mode to a negative quadrupole mode.

Finally, we calculate the mechanical effects created from the enhanced absorption and scattering at the plasmonic resonance modes. While absorption is generally regarded as the major mechanism of spin angular momentum transfer from light to plasmonic particles, this is not always true for objects excited at particular modes of resonance where conversion of the angular momentum mode occurs. In particular, we find that the angular momentum transfer is dominated by the scattering process at the negative quadrupole mode of a triangular particle. The scattered field carries a different angular momentum value from the incident field due to conversion effect at non-dipolar plasmon resonance. As a result, an unusually large, scattering-dominant mechanical torque is applied to the plasmonic particle.

The primary focus of the thesis presented is to elucidate the angular momentum transfer and conversion by a single plasmonic resonator through numerical calculations. After basic experimental characterization, the natural next step can be branched two-folds. First is to focus

on the enhancement of the mechanical effect created onto a single particle. Second is to integrate the resonators into a metamaterial or a metasurface environment, which can manipulate light, fluid, or adjacent micro/nanoparticles using the field distribution created.

5.2. Considerations and Future Outlook

This section summarizes the necessary steps for an improved study of the mechanical effects due to scattering. Several key points which require a deeper investigation are summarized.

5.2.1. Handling a Substrate or a Surrounding Medium

The current simulation results in this thesis are carried out with a homogeneous medium of air (n=1), except for the extinction result of Figure 11. This avoided the issue of field momentum inside matter. However, for future simulations involving experimental verifications, it is essential to introduce a substrate or a homogeneous medium surrounding the plasmonic particle.

The definition of electromagnetic momentum inside a medium has been an active topic of debate in the previous century, also referred to as the "Abraham-Minkowski controversy". Minkowski defined electromagnetic momentum as:

$$\mathbf{D}\times\mathbf{B} \tag{5.1}$$

and Abraham defined it in an alternative form as:

$$\varepsilon_0\mu_0\mathbf{E}\times\mathbf{H}. \tag{5.2}$$

The momentum density vector for a nonmagnetic medium is

$$\mathbf{G}=\mathbf{D}\times\mathbf{B}=\varepsilon_0\mu_0\mathbf{E}\times\mathbf{H}+\mathbf{P}\times\mu_0\mathbf{H} \tag{5.3}$$

where the wave momentum density is a summation of the electromagnetic momentum density $\varepsilon_0\mu_0\mathbf{E}\times\mathbf{H}$ and a momentum density resulting from the dielectric polarization in response to a field, $\mathbf{P}=\mathbf{D}-\varepsilon_0\mathbf{E}$. There are excellent review articles which summarize the distinction between the two formulas [106]. As a result, the Abraham and Minkowski conventions for the definition of light momentum inside a dielectric medium differ by a factor of ε^2.

Ways to reconcile this controversy has been proposed by Barnett in 2010, by carefully and consistently assigning different values for the momentum transferred to the dielectric matter when light is incident upon it [107]. In summary, the Abraham form strictly represents the kinetic momentum carried by the field, while the Minkowsky form represents the recoil momentum which can be measured experimentally. The Minkowski form is also the canonical momentum satisfying the commutation relationship between displacement and momentum operators. As long as one formula is used consistently with the adequate term for the momentum transferred to the medium, both formulas give correct results.

Because the recoil momentum is the one measurable through experiments, recent experiments have confirmed again and again the use of the Minkowski form convenient and correct [108]. Therefore, we suggest that the Minkowski momentum form be used inside the Maxwell Stress Tensor.

5.2.2. Mode Theory

This thesis calculates the optical response which depends on the input excitation. Eigenmode analysis, on the other hand, would provide a more accurate study of all of the resonances supported by a resonator, and enable a study of the coupling between different resonance modes. This is the necessary next step for the theoretical analysis of the non-dipolar high order resonance supported by plasmonic particles.

5.2.3. Analysis of Thermal Effects

Because the plasmon phenomenon in optical and telecommunication frequencies typically originates from the collective oscillations of free charges in a material due to an applied electromagnetic field, plasmonic devices generally require metallic components, which have an abundance of free electrons [109]. These free electrons provide the negative real permittivity that is an essential property of any plasmonic material. However, metals are plagued by large losses, especially in the visible and ultraviolet (UV) spectral ranges, arising in part from interband

electronic transitions. Even the metals with the highest conductivities suffer from large losses at optical frequencies.

In the Mie scattering regime, between the two size extremes, an enhancement in scattering always entails an unwanted enhancement of absorption, and vice versa. Resonant illumination can cause significant heat generation due to enhanced optical absorption by the nanostructures, which results in a subsequent release of heat into the surrounding environment. Because these consequences of plasmonic heating are generally regard as deleterious to the optical trap, researchers have used various techniques including integrated heat sinks [110] to mitigate heating. Also, structures that are well connected to the environment which allows heat dissipation, such as extended metal surfaces or gratings are favored over isolated nanoparticles. The extended metal surface can serve as a heat sink to prevent deleterious heat accumulation. On the other hand, reserachers are also striving to search for ways to take advantage of the convective forces arising from heating. Light-induced thermal heating alone can create very large mechanical forces, often referred to as photophoresis [111].

Quantifying the amount of heat generated from optical excitation can be done through simple FEM simulations. The analysis of the convective forces arising from thermal gradient would complete the analysis of light-induced mechanical effects and allow accurate predictions of experimental results.

5.2.4. Experimental Characterization of the Scattered Field

Two types of experiments can be designed from the simulation results presented in this thesis. The first is to fix a particle, or an array of particles, on a rigid substrate or inside a medium. The constraints in the mechanical movement allow a steady measurement of the scattered elecrtromagnetic field surrounding the particle. The second is to allow and detect the mechanical movement of the nanoparticle inside a fluid.

In both directions, the synthesis or fabrication of the plasmonic structure can be done through various methods. Both top-down electron beam fabrication methods, as well as bottom-up chemical synthesis in solution, are available to create subwavelength plasmonic nanostructures with varied geometries. While chemical synthesis provides a superior quality of the atomic flatness and sharp corners to create maximum field enhancement, it is generally

difficult to sort and arrange the nanoparticles into a desired pattern. Electron beam fabrication allows nanostructures fabricated with rounded corners, and the substrate can be varied as long as a conducting layer is present. For transparent optical substrates, ITO-coated (Indium Tin Oxide) glass is widely used, with a Titanium adhesion layer to attach gold on top of the glass surface. In case a homogeneous medium is desired, index-matching oil can be used to create an optically homogeneous dielectric environment.

Next, the characterization methods for the highly scattering nanostructures will be briefly reviewed. The experimental techniques for the measurement of plasmonic excitation of nanoparticles can be broadly grouped into far-field and near-field methods. The far-field method measures the radiation field propagated from the nanoparticle, while the near-field methods use highly localized excitation or detection, or both. Various near-field spectroscopy techniques have been used in the past to quantify the plasmonic electromagnetic field enhancement. NSOM (Nearfield Scanning Optical Microscopy) is a technique where the near field distribution is scanned in response to a local optical excitation . Other methods using particle beams include Cathodo-Luminescence (CL) spectroscopy, which detects the photons generated from a local electron excitation [54], and Electron Energy Loss Spectroscopy (EELS), which measures the loss of energy of the scattererd electrons [112].

We hope these steps will be pursued in the near future.

References

[1] M. A. El-Sayed, "Some Interesting Properties of Metals Confined in Time and Nanometer Space of Different Shapes," *Accounts Chem. Res.*, vol. 34, no. 4, pp. 257–264, Apr. 2001.

[2] Y. Xia and N. J. Halas, "Shape-controlled synthesis and surface plasmonic properties of metallic nanostructures," *MRS Bull.*, vol. 30, no. 05, pp. 338–348, 2005.

[3] S. Franke-Arnold, L. Allen, and M. Padgett, "Advances in optical angular momentum," *Laser Photonics Rev.*, vol. 2, no. 4, pp. 299–313, 2008.

[4] J. C. Maxwell, *A treatise on electricity and magnetism*, vol. 1. Clarendon press, 1881.

[5] J. H. Poynting, "On the transfer of energy in the electromagnetic field," *Philos. Trans. R. Soc. Lond.*, vol. 175, pp. 343–361, 1884.

[6] J. Poynting, "The wave motion of a revolving shaft, and a suggestion as to the angular momentum in a beam of circularly polarised light," *Proc. R. Soc. Lond. Ser.*, vol. 82, no. 557, pp. 560–567, 1909.

[7] R. A. Beth, "Mechanical detection and measurement of the angular momentum of light," *Phys. Rev.*, vol. 50, no. 2, p. 115, 1936.

[8] A. Ashkin, "Trapping of atoms by resonance radiation pressure," *Phys. Rev. Lett.*, vol. 40, no. 12, pp. 729–732, 1978.

[9] A. Ashkin, J. M. Dziedzic, J. E. Bjorkholm, and S. Chu, "Observation of a single-beam gradient force optical trap for dielectric particles," *Opt. Lett.*, vol. 11, no. 5, pp. 288–290, 1986.

[10] D. G. Grier, "A revolution in optical manipulation," *Nature*, vol. 424, no. 6950, pp. 810–816, 2003.

[11] C. Bustamante, Z. Bryant, and S. B. Smith, "Ten years of tension: single-molecule DNA mechanics," *Nature*, vol. 421, no. 6921, pp. 423–427, 2003.

[12] T. Pilizota, T. Bilyard, F. Bai, M. Futai, H. Hosokawa, and R. M. Berry, "A programmable optical angle clamp for rotary molecular motors," *Biophys. J.*, vol. 93, no. 1, pp. 264–275, 2007.

[13] J. R. Moffitt, Y. R. Chemla, S. B. Smith, and C. Bustamante, "Recent advances in optical tweezers," *Annu Rev Biochem*, vol. 77, pp. 205–228, 2008.

[14] Z. Bryant, M. D. Stone, J. Gore, S. B. Smith, N. R. Cozzarelli, and C. Bustamante, "Structural transitions and elasticity from torque measurements on DNA," *Nature*, vol. 424, no. 6946, pp. 338–341, 2003.

[15] C. Claudet and J. Bednar, "Magneto-optical tweezers built around an inverted microscope," *Appl. Opt.*, vol. 44, no. 17, pp. 3454–3457, 2005.

[16] G. Romano, L. Sacconi, M. Capitanio, and F. Pavone, "Force and torque measurements using magnetic micro beads for single molecule biophysics," *Opt. Commun.*, vol. 215, no. 4, pp. 323–331, 2003.

[17] L. Sacconi, G. Romano, R. Ballerini, M. Capitanio, M. De Pas, M. Giuntini, D. Dunlap, L. Finzi, and F. Pavone, "Three-dimensional magneto-optic trap for micro-object manipulation," *Opt. Lett.*, vol. 26, no. 17, pp. 1359–1361, 2001.

[18] A. Crut, D. A. Koster, R. Seidel, C. H. Wiggins, and N. H. Dekker, "Fast dynamics of supercoiled DNA revealed by single-molecule experiments," *Proc. Natl. Acad. Sci.*, vol. 104, no. 29, pp. 11957–11962, 2007.

[19] V. Bingelyte, J. Leach, J. Courtial, and M. Padgett, "Optically controlled three-dimensional rotation of microscopic objects," *Appl. Phys. Lett.*, vol. 82, no. 5, pp. 829–831, 2003.

[20] M. Friese, J. Enger, H. Rubinsztein-Dunlop, and N. R. Heckenberg, "Optical angular-momentum transfer to trapped absorbing particles," *Phys. Rev.*, vol. 54, no. 2, p. 1593, 1996.

[21] M. Friese, T. Nieminen, N. Heckenberg, and H. Rubinsztein-Dunlop, "Optical torque controlled by elliptical polarization," *Opt. Lett.*, vol. 23, no. 1, pp. 1–3, 1998.

[22] H. He, M. E. J. Friese, N. R. Heckenberg, and H. Rubinsztein-Dunlop, "Direct observation of transfer of angular momentum to absorptive particles from a laser beam with a phase singularity," *Phys. Rev. Lett.*, vol. 75, no. 5, pp. 826–829, 1995.
[23] S. Parkin, G. Knöner, W. Singer, T. A. Nieminen, N. R. Heckenberg, and H. Rubinsztein-Dunlop, "Optical torque on microscopic objects," *Methods Cell Biol.*, vol. 82, pp. 525–561, 2007.
[24] A. I. Bishop, T. A. Nieminen, N. R. Heckenberg, and H. Rubinsztein-Dunlop, "Optical application and measurement of torque on microparticles of isotropic nonabsorbing material," *Phys. Rev.*, vol. 68, no. 3, p. 033802, 2003.
[25] P. Galajda and P. Ormos, "Complex micromachines produced and driven by light," *Appl. Phys. Lett.*, vol. 78, no. 2, p. 249, 2001.
[26] L. Oroszi, P. Galajda, H. Kirei, S. Bottka, and P. Ormos, "Direct measurement of torque in an optical trap and its application to double-strand DNA," *Phys. Rev. Lett.*, vol. 97, no. 5, p. 058301, 2006.
[27] M. Friese, T. Nieminen, N. Heckenberg, and H. Rubinsztein-Dunlop, "Optical alignment and spinning of laser-trapped microscopic particles," *Nature*, vol. 394, no. 6691, pp. 348–350, 1998.
[28] A. La Porta and M. D. Wang, "Optical torque wrench: angular trapping, rotation, and torque detection of quartz microparticles," *Phys. Rev. Lett.*, vol. 92, no. 19, p. 190801, 2004.
[29] W. Singer, T. A. Nieminen, U. J. Gibson, N. R. Heckenberg, and H. Rubinsztein-Dunlop, "Orientation of optically trapped nonspherical birefringent particles," *Phys. Rev. E*, vol. 73, no. 2, p. 021911, 2006.
[30] T. A. Nieminen, N. R. Heckenberg, and H. Rubinsztein-Dunlop, "Optical measurement of microscopic torques," *J. Mod. Opt.*, vol. 48, no. 3, pp. 405–413, 2001.
[31] C. Deufel, S. Forth, C. R. Simmons, S. Dejgosha, and M. D. Wang, "Nanofabricated quartz cylinders for angular trapping: DNA supercoiling torque detection," *Nat. Methods*, vol. 4, no. 3, pp. 223–225, 2007.
[32] C. Gosse and V. Croquette, "Magnetic tweezers: micromanipulation and force measurement at the molecular level," *Biophys. J.*, vol. 82, no. 6, pp. 3314–3329, 2002.
[33] J. Voldman, R. A. Braff, M. Toner, M. L. Gray, and M. A. Schmidt, "Holding forces of single-particle dielectrophoretic traps.," *Biophys. J.*, vol. 80, no. 1, p. 531, 2001.
[34] R. Quidant, D. Petrov, and G. Badenes, "Radiation forces on a Rayleigh dielectric sphere in a patterned optical near field," *Opt. Lett.*, vol. 30, no. 9, pp. 1009–1011, 2005.
[35] A. E. Cohen and W. Moerner, "Suppressing Brownian motion of individual biomolecules in solution," *Proc. Natl. Acad. Sci. U. S. A.*, vol. 103, no. 12, pp. 4362–4365, 2006.
[36] D. M. Eigler and E. K. Schweizer, "Positioning single atoms with a scanning tunnelling microscope," *Nature*, vol. 344, no. 6266, pp. 524–526, 1990.
[37] G. Binnig, C. F. Quate, and C. Gerber, "Atomic force microscope," *Phys. Rev. Lett.*, vol. 56, no. 9, pp. 930–933, 1986.
[38] P. L. Marston and J. H. Crichton, "Radiation torque on a sphere caused by a circularly-polarized electromagnetic wave," *Phys. Rev.*, vol. 30, no. 5, p. 2508, 1984.
[39] G. Mie, "Beiträge zur Optik trüber Medien, speziell kolloidaler Metallösungen," *Ann. Phys.*, vol. 330, no. 3, pp. 377–445, 1908.
[40] M. Kerker, D.-S. Wang, and C. Giles, "Electromagnetic scattering by magnetic spheres," *JOSA*, vol. 73, no. 6, pp. 765–767, 1983.
[41] Z. Wu and Y. Wang, "Electromagnetic scattering for multilayered sphere: recursive algorithms," *Radio Sci.*, vol. 26, no. 6, pp. 1393–1401, 1991.
[42] S. Asano and G. Yamamoto, "Light scattering by a spheroidal particle," *Appl. Opt.*, vol. 14, no. 1, pp. 29–49, 1975.
[43] N. Voshchinnikov and V. Farafonov, "Optical properties of spheroidal particles," *Astrophys. Space Sci.*, vol. 204, no. 1, pp. 19–86, 1993.
[44] P. K. Jain, K. S. Lee, I. H. El-Sayed, and M. A. El-Sayed, "Calculated Absorption and Scattering Properties of Gold Nanoparticles of Different Size, Shape, and Composition: Applications in

Biological Imaging and Biomedicine," *J. Phys. Chem. B*, vol. 110, no. 14, pp. 7238–7248, Apr. 2006.
[45] A. J. Haes and R. P. Van Duyne, "A nanoscale optical biosensor: sensitivity and selectivity of an approach based on the localized surface plasmon resonance spectroscopy of triangular silver nanoparticles," *J. Am. Chem. Soc.*, vol. 124, no. 35, pp. 10596–10604, 2002.
[46] A. Ulman, "An Introduction to Ultrathin Organic Films Academic," *New York*, pp. 237–245, 1991.
[47] K. Kneipp, H. Kneipp, I. Itzkan, R. R. Dasari, M. S. Feld, and others, "Ultrasensitive chemical analysis by Raman spectroscopy," *Chem. Rev.*, vol. 99, pp. 2957–2976, 1999.
[48] A. Parfenov, I. Gryczynski, J. Malicka, C. D. Geddes, and J. R. Lakowicz, "Enhanced fluorescence from fluorophores on fractal silver surfaces," *J. Phys. Chem. B*, vol. 107, no. 34, pp. 8829–8833, 2003.
[49] C. J. Murphy, T. K. Sau, A. M. Gole, C. J. Orendorff, J. Gao, L. Gou, S. E. Hunyadi, and T. Li, "Anisotropic Metal Nanoparticles: Synthesis, Assembly, and Optical Applications," *J. Phys. Chem. B*, vol. 109, no. 29, pp. 13857–13870, Jul. 2005.
[50] R. Jin, Y. W. Cao, C. A. Mirkin, K. L. Kelly, G. C. Schatz, and J. G. Zheng, "Photoinduced conversion of silver nanospheres to nanoprisms," *Science*, vol. 294, no. 5548, pp. 1901–1903, 2001.
[51] J. E. Millstone, S. J. Hurst, G. S. Métraux, J. I. Cutler, and C. A. Mirkin, "Colloidal gold and silver triangular nanoprisms," *Small*, vol. 5, no. 6, pp. 646–664, 2009.
[52] M. Rang, A. C. Jones, F. Zhou, Z.-Y. Li, B. J. Wiley, Y. Xia, and M. B. Raschke, "Optical Near-Field Mapping of Plasmonic Nanoprisms," *Nano Lett.*, vol. 8, no. 10, pp. 3357–3363, Oct. 2008.
[53] Q. Zhang, N. Li, J. Goebl, Z. Lu, and Y. Yin, "A Systematic Study of the Synthesis of Silver Nanoplates: Is Citrate a 'Magic' Reagent?," *J. Am. Chem. Soc.*, vol. 133, no. 46, pp. 18931–18939, Nov. 2011.
[54] P. Chaturvedi, K. H. Hsu, A. Kumar, K. H. Fung, J. C. Mabon, and N. X. Fang, "Imaging of plasmonic modes of silver nanoparticles using high-resolution cathodoluminescence spectroscopy," *ACS Nano*, vol. 3, no. 10, pp. 2965–2974, 2009.
[55] J. E. Millstone, S. Park, K. L. Shuford, L. Qin, G. C. Schatz, and C. A. Mirkin, "Observation of a Quadrupole Plasmon Mode for a Colloidal Solution of Gold Nanoprisms," *J. Am. Chem. Soc.*, vol. 127, no. 15, pp. 5312–5313, Apr. 2005.
[56] K. Svoboda and S. M. Block, "Optical trapping of metallic Rayleigh particles," *Opt. Lett.*, vol. 19, no. 13, pp. 930–932, 1994.
[57] S. Sato, Y. Harada, and Y. Waseda, "Optical trapping of microscopic metal particles," *Opt. Lett.*, vol. 19, no. 22, pp. 1807–1809, 1994.
[58] K. Sasaki, M. Koshioka, H. Misawa, N. Kitamura, and H. Masuhara, "Optical trapping of a metal particle and a water droplet by a scanning laser beam," *Appl. Phys. Lett.*, vol. 60, no. 7, pp. 807–809, 1992.
[59] P. M. Hansen, V. K. Bhatia, N. Harrit, and L. Oddershede, "Expanding the optical trapping range of gold nanoparticles," *Nano Lett.*, vol. 5, no. 10, pp. 1937–1942, 2005.
[60] L. Bosanac, T. Aabo, P. M. Bendix, and L. B. Oddershede, "Efficient optical trapping and visualization of silver nanoparticles," *Nano Lett.*, vol. 8, no. 5, pp. 1486–1491, 2008.
[61] Y. Seol, A. E. Carpenter, and T. T. Perkins, "Gold nanoparticles: enhanced optical trapping and sensitivity coupled with significant heating," *Opt. Lett.*, vol. 31, no. 16, pp. 2429–2431, 2006.
[62] L. N. Ng, M. N. Zervas, J. S. Wilkinson, and B. J. Luff, "Manipulation of colloidal gold nanoparticles in the evanescent field of a channel waveguide," *Appl. Phys. Lett.*, vol. 76, no. 15, p. 1993, 2000.
[63] K. Sasaki, J. Hotta, K. Wada, and H. Masuhara, "Analysis of radiation pressure exerted on a metallic particle within an evanescent field," *Opt. Lett.*, vol. 25, no. 18, pp. 1385–1387, 2000.
[64] S. Gaugiran, S. Gétin, J. Fedeli, G. Colas, A. Fuchs, F. Chatelain, and J. Dérouard, "Optical manipulation of microparticles and cells on silicon nitride waveguides," *Opt. Express*, vol. 13, no. 18, pp. 6956–6963, 2005.

[65] A. H. J. Yang, T. Lerdsuchatawanich, and D. Erickson, "Forces and Transport Velocities for a Particle in a Slot Waveguide," *Nano Lett.*, vol. 9, no. 3, pp. 1182–1188, Mar. 2009.
[66] A. N. Grigorenko, N. W. Roberts, M. R. Dickinson, and Y. Zhang, "Nanometric optical tweezers based on nanostructured substrates," *Nat. Photonics*, vol. 2, no. 6, pp. 365–370, May 2008.
[67] L. Novotny, R. X. Bian, and X. S. Xie, "Theory of nanometric optical tweezers," *Phys. Rev. Lett.*, vol. 79, no. 4, pp. 645–648, 1997.
[68] M. Righini, P. Ghenuche, S. Cherukulappurath, V. Myroshnychenko, F. J. García de Abajo, and R. Quidant, "Nano-optical trapping of Rayleigh particles and Escherichia coli bacteria with resonant optical antennas," *Nano Lett.*, vol. 9, no. 10, pp. 3387–3391, 2009.
[69] M. Righini, G. Volpe, C. Girard, D. Petrov, and R. Quidant, "Surface plasmon optical tweezers: tunable optical manipulation in the femtonewton range," *Phys. Rev. Lett.*, vol. 100, no. 18, p. 186804, 2008.
[70] V. Garcés-Chávez, R. Quidant, P. J. Reece, G. Badenes, L. Torner, and K. Dholakia, "Extended organization of colloidal microparticles by surface plasmon polariton excitation," *Phys. Rev. B*, vol. 73, no. 8, Feb. 2006.
[71] G. Volpe, R. Quidant, G. Badenes, and D. Petrov, "Surface Plasmon Radiation Forces," *Phys. Rev. Lett.*, vol. 96, no. 23, Jun. 2006.
[72] K. Wang, E. Schonbrun, and K. B. Crozier, "Propulsion of gold nanoparticles with surface plasmon polaritons: evidence of enhanced optical force from near-field coupling between gold particle and gold film," *Nano Lett.*, vol. 9, no. 7, pp. 2623–2629, 2009.
[73] A. T. O'Neil and M. J. Padgett, "Three-dimensional optical confinement of micron-sized metal particles and the decoupling of the spin and orbital angular momentum within an optical spanner," *Opt. Commun.*, vol. 185, no. 1, pp. 139–143, 2000.
[74] M. Liu, T. Zentgraf, Y. Liu, G. Bartal, and X. Zhang, "Light-driven nanoscale plasmonic motors," *Nat. Nanotechnol.*, vol. 5, no. 8, pp. 570–573, 2010.
[75] A. Lehmuskero, R. Ogier, T. Gschneidtner, P. Johansson, and M. Käll, "Ultrafast Spinning of Gold Nanoparticles in Water Using Circularly Polarized Light," *Nano Lett.*, p. 130624122754005, Jun. 2013.
[76] J.D. Jackson, *Classical Electrodynamics*, Third Edition. Wiley.
[77] N. W. Ashcroft and N. D. Mermin, "Solid state physics," *Saunders Coll. Phila.*, vol. 1, 1976.
[78] S. A. Maier, *Plasmonics: fundamentals and applications*. Springer Science+ Business Media, 2007.
[79] C. F. Bohren and D. R. Huffman, *Absorption and scattering of light by small particles*. Wiley-Vch, 2008.
[80] P. B. Johnson and R. Christy, "Optical constants of the noble metals," *Phys. Rev. B*, vol. 6, no. 12, p. 4370, 1972.
[81] Y.-Y. Yu, S.-S. Chang, C.-L. Lee, and C. C. Wang, "Gold nanorods: electrochemical synthesis and optical properties," *J. Phys. Chem. B*, vol. 101, no. 34, pp. 6661–6664, 1997.
[82] L. R. Hirsch, A. M. Gobin, A. R. Lowery, F. Tam, R. A. Drezek, N. J. Halas, and J. L. West, "Metal nanoshells," *Ann. Biomed. Eng.*, vol. 34, no. 1, pp. 15–22, 2006.
[83] C. L. Nehl, H. Liao, and J. H. Hafner, "Optical Properties of Star-Shaped Gold Nanoparticles," *Nano Lett.*, vol. 6, no. 4, pp. 683–688, Apr. 2006.
[84] H. Wang, D. W. Brandl, F. Le, P. Nordlander, and N. J. Halas, "Nanorice: a hybrid plasmonic nanostructure," *Nano Lett.*, vol. 6, no. 4, pp. 827–832, 2006.
[85] M. Schnell, A. García-Etxarri, A. J. Huber, K. Crozier, J. Aizpurua, and R. Hillenbrand, "Controlling the near-field oscillations of loaded plasmonic nanoantennas," *Nat. Photonics*, vol. 3, no. 5, pp. 287–291, Apr. 2009.
[86] P. Muhlschlegel, "Resonant Optical Antennas," *Science*, vol. 308, no. 5728, pp. 1607–1609, Jun. 2005.
[87] L. Novotny and N. van Hulst, "Antennas for light," *Nat. Photonics*, vol. 5, no. 2, pp. 83–90, 2011.
[88] M. Born and E. Wolf, *Principles of optics: electromagnetic theory of propagation, interference and diffraction of light*. CUP Archive, 1999.

[89] L. Allen, S. M. Barnett, and M. J. Padgett, *Optical angular momentum*. Taylor & Francis, 2003.
[90] L. Allen, M. Beijersbergen, R. Spreeuw, J. Woerdman, and others, "Orbital angular momentum of light and the transformation of Laguerre-Gaussian laser modes," *Phys. Rev.*, vol. 45, no. 11, pp. 8185–8189, 1992.
[91] N. Simpson, K. Dholakia, L. Allen, and M. Padgett, "Mechanical equivalence of spin and orbital angular momentum of light: an optical spanner," *Opt. Lett.*, vol. 22, no. 1, pp. 52–54, 1997.
[92] K. Volke-Sepúlveda, S. Chávez-Cerda, V. Garcés-Chávez, and K. Dholakia, "Three-dimensional optical forces and transfer of orbital angular momentum from multiringed light beams to spherical microparticles," *JOSA B*, vol. 21, no. 10, pp. 1749–1757, 2004.
[93] A. Ungut, G. Grehan, and G. Gouesbet, "Comparisons between geometrical optics and Lorenz-Mie theory," *Appl. Opt.*, vol. 20, no. 17, pp. 2911–2918, 1981.
[94] M. I. Mishchenko, L. D. Travis, and D. W. Mackowski, "< i> T</i>-matrix computations of light scattering by nonspherical particles: A review," *J. Quant. Spectrosc. Radiat. Transf.*, vol. 55, no. 5, pp. 535–575, 1996.
[95] A. Ludwig, "The generalized multipole technique," *Comput. Phys. Commun.*, vol. 68, no. 1, pp. 306–314, 1991.
[96] E. M. Purcell and C. R. Pennypacker, "Scattering and absorption of light by nonspherical dielectric grains," *Astrophys. J.*, vol. 186, pp. 705–714, 1973.
[97] J. P. Kottmann, O. J. F. Martin, D. R. Smith, and S. Schultz, "Field polarization and polarization charge distributions in plasmon resonant nanoparticles," *New J. Phys.*, vol. 2, no. 1, p. 27, 2000.
[98] A. Taflove and S. C. Hagness, "Computationai Electrodynamics," 2000.
[99] K. Yee, "Numerical solution of initial boundary value problems involving Maxwell's equations in isotropic media," *Antennas Propag. IEEE Trans.*, vol. 14, no. 3, pp. 302–307, 1966.
[100] E. D. Palik, *Handbook of Optical Constants of Solids: Index*, vol. 3. Academic press, 1998.
[101] J. Wang, J.-Y. Yang, I. M. Fazal, N. Ahmed, Y. Yan, H. Huang, Y. Ren, Y. Yue, S. Dolinar, M. Tur, and A. E. Willner, "Terabit free-space data transmission employing orbital angular momentum multiplexing," *Nat. Photonics*, vol. 6, no. 7, pp. 488–496, Jun. 2012.
[102] K. Dholakia and T. \vCi\vzmár, "Shaping the future of manipulation," *Nat. Photonics*, vol. 5, no. 6, pp. 335–342, 2011.
[103] N. Yu, F. Aieta, P. Genevet, M. A. Kats, Z. Gaburro, and F. Capasso, "A Broadband, Background-Free Quarter-Wave Plate Based on Plasmonic Metasurfaces," *Nano Lett.*, vol. 12, no. 12, pp. 6328–6333, Dec. 2012.
[104] P. Genevet, N. Yu, F. Aieta, J. Lin, M. A. Kats, R. Blanchard, M. O. Scully, Z. Gaburro, and F. Capasso, "Ultra-thin plasmonic optical vortex plate based on phase discontinuities," *Appl. Phys. Lett.*, vol. 100, no. 1, p. 013101, 2012.
[105] N. Yu, P. Genevet, M. A. Kats, F. Aieta, J. P. Tetienne, F. Capasso, and Z. Gaburro, "Light propagation with phase discontinuities: generalized laws of reflection and refraction," *Science*, vol. 334, no. 6054, pp. 333–337, 2011.
[106] P. W. Milonni and R. W. Boyd, "Momentum of light in a dielectric medium," *Adv. Opt. Photonics*, vol. 2, no. 4, pp. 519–553, 2010.
[107] S. M. Barnett, "Resolution of the Abraham-Minkowski Dilemma," *Phys. Rev. Lett.*, vol. 104, no. 7, Feb. 2010.
[108] V. Kajorndejnukul, W. Ding, S. Sukhov, C.-W. Qiu, and A. Dogariu, "Linear momentum increase and negative optical forces at dielectric interface," *Nat. Photonics*, Aug. 2013.
[109] K. Dholakia and T. Čižmár, "Light and Heat in a Balancing Act," *Physics*, vol. 5, Jul. 2012.
[110] K. Wang, E. Schonbrun, P. Steinvurzel, and K. B. Crozier, "Trapping and rotating nanoparticles using a plasmonic nano-tweezer with an integrated heat sink," *Nat. Commun.*, vol. 2, p. 469, 2011.
[111] M. Esseling, P. Rose, C. Alpmann, and C. Denz, "Photophoretic trampoline —Interaction of single airborne absorbing droplets with light," *Appl. Phys. Lett.*, vol. 101, no. 13, pp. 131115–131115, 2012.
[112] R. F. Egerton, *Electron energy-loss spectroscopy in the electron microscope*. Springer, 2011.